Systems Driven out of Equilibrium with Energy Input at Interfaces or Boundaries.

Linjun Li

Dissertation submitted to the Faculty of the
Virginia Polytechnic Institute and State University
in partial fulfillment of the requirements for the degree of

Doctor of Philosophy
in
Physics

Michel J. Pleimling, Chair
Jean J. Heremans
Uwe C. Täuber
Chenggang Tao

October 25^{th}, 2015
Blacksburg, Virginia

Keywords: Monte Carlo Simulation, Two-temperature Lattice Gas, Magnetic Friction,
Non-equilibrium Phase Transition, Surface Critical Phenomena.

Systems Driven out of Equilibrium with Energy Input at Interfaces or Boundaries.

Linjun Li

We study the non-equilibrium behavior of systems that are driven out of equilibrium from the interface. In the first part of this thesis, we study a model of a two-dimensional lattice gas that is in contact with two heat baths that are at different temperatures. Performing Monte Carlo simulations, we find that there are three possible types of non-equilibrium steady states, depending on the values of certain system parameters. They include a disordered phase, a fully phase separated state, and an interesting state with striped patterns in the half of the lattice where the temperature is lower. The last one is a novel non-equilibrium steady state that we study systematically by varying the system parameters. To obtain the non-equilibrium finite-size phase diagram, we perform a spectrum analysis to classify not only the three major states, but also the sub-states of the striped phase. In the second part of the thesis, we study magnetic friction that results when two Potts systems move with respect to each other. In this research, we first study a model that consists of two interacting Potts blocks, where one block moves on top of the other. As a result, the system is driven out of equilibrium constantly. In our research we find for weak interfacial couplings that the contacting surfaces behave rather similar to a free surface. If the interfacial coupling is strong, however, anisotropic spin patterns appear on the contacting surfaces. This study is extended to a three-dimensional Potts wedge with a tip sliding along the surface of a Potts block. It is found that the shape of the Potts lattice influences the surface behavior of the system.

This work is supported by the US National Science Foundation through Grants DMR-0904999 and DMR-1205309.

Dedication

In memory of my father Zhiming Li (passed away in April 2009), my grandmother Yutian Gao (passed away in April 2011) and my grandfather Huisheng Zhong (passed away in November 2012).

Acknowledgments

I would like to take this opportunity to thank my advisor, Dr. Michel Pleimling, for his mentorship, patience and understanding during the years. Without the guidance and support of Dr. Pleimling, I would not have the opportunity to explore in such an interesting field (non-equilibrium statistical mechanics). I would also like to express my gratitude to my committee member and first year temporary advisor Dr. Uwe Täuber, for his patience in teaching and high standards to students, and his insightful comments and suggestions for my dissertation. In addition, I would like to thank my committee member Dr. Jean Heremans and Dr. Chenggang Tao, for their support throughout my academic endeavor at Virginia Tech. Also, I would like to thank all other professors in department of physics who have taught me, for their patience and hard work; and all the fellow graduate students with whom I sit through the classes together, go to conferences together, or worked together, for their brotherhood. Further, I want to thank graduate program coordinators Ms. Chris Thomas and Ms. Betty Wilkins, for their great effort to help and support graduate students. Their timely responses to students show their true care for the physics graduate students, and I always feel in debt about what they have brought us.

I would like to thank my dear father Zhiming Li, who keeps giving me invaluable guidance and care until the last second I see him. From my father I learned how to become a better person, for which I will be in debt for the rest of my life. I would like to thank my

dear grandmother Yutian Gao and my dear grandfather Huisheng Zhong, who brought warmness to my life. Your smiles and vivid conversations are still existing in my dreams and they will never fade.

Last, but not the least, I want to show my thankfulness to my mother Li Zhong, my grandmother Huizhen Li, my grandfather Shuhua Li, my aunt Jie Li, and my uncle Zhiqiang Li, for their constant care and encouragement throughout these years, and for surviving me through the saddest years in my life. Also, I want to say thank you to my boyfriend Xiangwen Wang, the one who brings happiness back to my life.

Contents

List of Figures

List of Tables

Chapter 1

Introduction

The research presented in this thesis focuses on a special type of non-equilibrium systems. Instead of having constant external forces (energy input) uniformly applied to the whole system, our systems under investigation are only locally disturbed. From the two models presented in this dissertation we find that for some systems local disturbances change the non-equilibrium steady state properties throughout the system, whereas for other systems changes only appear near the places where energy input takes place. Together with the description of the resulting non-equilibrium steady states in the studied models, we also present our analysis of the non-equilibrium phase transitions that take place in these systems.

In this Chapter we will first introduce Ising and Potts systems, followed by a short discussion of the statistical approaches used for understanding equilibrium systems and non-equilibrium systems. At last, we will introduce the different types of models studied in this dissertation.

1.1 Ising and Potts Systems

1.1.1 The Ising model

The Ising model was invented by the German physicist Wihelm Lenz as a problem to be solved by his student Ernst Ising [1]. The Ising model is used for the study of ferromagnetism in the framework of classical statistical mechanics. In this model, we have a d-dimensional lattice where every lattice site is characterized by a variable (spin) that can take one of the two possible states, denoted as $\sigma_i = 1$ and $\sigma_i = -1$ (here i is the index that marks the location of a specific site). In the Ising model only the neighboring sites are coupled, and each pair yields a coupling energy. Also, if a site at location i is experiencing an external field h_i, a magnetic potential energy is formed in the form of -$\mu h_i \sigma_i$, where μ is the magnetic moment. Thus, the general form for the total energy of an Ising system is given by the following expression:

$$H(\sigma) = -\sum_{<i,j>} J_{i,j}\sigma_i\sigma_j - \mu\sum_j h_j\sigma_j \tag{1.1}$$

In this equation $\langle i, j\rangle$ denotes neighboring sites. The number of possible spin states at each site is $q = 2$.

1.1.2 The Potts model

The Potts model was introduced in 1951 by Renfrey Potts as a generalization of the Ising model [2]. In a Potts system the variable at each lattice site can take one of q possible values, where $q > 2$. The coupling energy and the magnetic potential energy is calculated in the same way as for the Ising model. The only difference is that σ_i, a spin located at site i, can take any of the values $0, 1, ..., q-1$. As a result, the form of the total energy

of a Potts system can also be described by an equation similar to Eq.(1.2).

$$H(\sigma) = -\sum_{<i,j>} J_{i,j}\delta(\sigma_i, \sigma_j) - \mu \sum_j h_j \sigma_j \tag{1.2}$$

In this equation, $\delta(\sigma_i, \sigma_j) = 1$ $\sigma_i = \sigma_j$, and zero otherwise.

1.2 Markov Processes

In stochastic processes the measured quantities are random variables. A Markov process, as introduced by Andrey Markov [3], is a stochastic process in which each new state of the system happens with a probability that only depends on the previous state of the system.

Mathematically, we can define this kind of "memoryless" time evolution by writing the following equation:

$$\begin{aligned} P_{1|n}(y_n, t_n | y_{n-1}, t_{n-1}; y_{n-2}, t_{n-2}; ...; y_0, t_0) = P_{1|1}(y_n, t_n | y_{n-1}, t_{n-1}), \\ (t_n > t_{n-1} > ... > t_1 > t_0). \end{aligned} \tag{1.3}$$

Here both $P_{1|n}$ and $P_{1|1}$ are conditional probabilities for the event y_n to take place at time t_n. The difference is that $P_{1|n}$ is the probability for the event to happen given that y_0 took place at t_0, y_1 took place at t_1, ..., and y_{n-1} took place at t_{n-1}, whereas $P_{1|1}$ is the probability of the event to happen only given that y_{n-1} happened at t_{n-1}.

What needs our attention is that the y_i's $(i = 0, 1, ..., n)$ in Eq.(1.3) are discrete random variables. We can also require that the times $t_0, t_1, t_2, ...$ in Eq.(1.3) are discrete. Including these two conditions, we call a stochastic process given by Eq.(1.3) a Markov chain. Since the possible spin states at each site are discrete in Ising and Potts systems, the ensembles of both type of systems are made up of only discrete micro-states. Also, since we will study our systems with Monte Carlo simulations where time is discrete and Eq.(1.3) is

satisfied (see Chapter 2), we can call our simulations of these Ising and Potts systems Markov Chain Monte Carlo (MCMC) simulations.

1.3 Chapman-Kolmogorov Equation and Master Equation

1.3.1 The Chapman-Kolmogorov Equation

In Eq.(1.3), the conditional probability $P_{1|1}(y_n, t_n|y_{n-1}, t_{n-1})$ is considered as a one-step transition probability, since there is no other intermediate process between times $t_n - 1$ and t_n. The Chapman-Kolmogorov (CK) equation [4, 5] is a prescription for calculating a n-step transition probability from multiple one-step transition probabilities for the continuous-micro-state Markov process. To calculate the two-step transition probability, we start with the joint probability of three events $P_3(y_3, t_3; y_2, t_2; y_1, t_1)$. Relating the joint probability to the one-step transition probabilities, we have:

$$\begin{aligned} P_3(y_3, t_3; y_2, t_2; y_1, t_1) &= P_2(y_2, t_2; y_1, t_1) P_{1|2}(y_3, t_3|y_1, t_1; y_2, t_2) \\ &= P_1(y_1, t_1) P_{1|1}(y_2, t_2|y_1, t_1) P_{1|2}(y_3, t_3|y_1, t_1; y_2, t_2), \\ &\qquad (t_3 > t_2 > t_1). \end{aligned} \tag{1.4}$$

According to the Markov property of the system, we have:

$$\begin{aligned} P_{1|2}(y_3, t_3|y_1, t_1; y_2, t_2) &= P_{1|1}(y_3, t_3|y_2, t_2), \\ &\qquad (t_3 > t_2 > t_1). \end{aligned} \tag{1.5}$$

For a Markov process with continuous micro-states, we can use Eq.(1.3) with the y_i being continuous. Thus yields the following relation:

$$\begin{aligned} P_3(y_3, t_3; y_2, t_2; y_1, t_1) &= P_1(y_1, t_1) P_{1|1}(y_2, t_2|y_1, t_1) P_{1|1}(y_3, t_3|y_2, t_2), \\ &\qquad (t_3 > t_2 > t_1). \end{aligned} \tag{1.6}$$

Considering that the measurement of the continuous-micro-state system can also be continuous, we can integrate both sides of Eq.(1.6) with respect to y_2:

$$\begin{aligned}\int P_3(y_3,t_3;y_2,t_2;y_1,t_1)dy_2 &= P_1(y_1,t_1)\int P_{1|1}(y_2,t_2|y_1,t_1)P_{1|1}(y_3,t_3|y_2,t_2)dy_2,\\ P_2(y_3,t_3;y_1,t_1) &= P_1(y_1,t_1)\int P_{1|1}(y_2,t_2|y_1,t_1)P_{1|1}(y_3,t_3|y_2,t_2)dy_2,\\ &\qquad (t_3>t_2>t_1).\end{aligned} \tag{1.7}$$

Dividing both sides of Eq.(1.7) by $P_1(y_1,t_1)$ gives:

$$\begin{aligned}P_{1|1}(y_3,t_3|y_1,t_1) &= \int P_{1|1}(y_3,t_3|y_2,t_2)P_{1|1}(y_2,t_2|y_1,t_1)dy_2,\\ &\qquad (t_3>t_2>t_1).\end{aligned} \tag{1.8}$$

Here, Eq.(1.9) is the Chapman-Kolmogorov equation for a two-step transition probability. Likewise, the Chapman-Kolmogorov equation for an n-step transition probability reads:

$$\begin{aligned}P_{1|1}(y_n,t_n|y_1,t_1) &= \int\int ...\int P_{1|1}(y_n,t_n|y_{n-1},t_{n-1})\times\\ P_{1|1}(y_{n-1},t_{n-1}|y_{n-2},t_{n-2})\times ...\times P_{1|1}(y_2,t_2|y_1,t_1)dy_{n-1}dy_{n-2}...dy_2,&\\ (t_n>t_{n-1}>...>t_1).&\end{aligned} \tag{1.9}$$

1.3.2 The Master Equation

For a continuous-time Markov process, we can find the probability of a system staying in a certain micro-state at a given time by solving the Master equation of the system. In this subsection I will explain how the Master equation is derived from the Chapman-Kolmogorov equation [6].

Starting from the definition of differentiation of $P_1(y,t)$:

$$\frac{\partial P_1(y,t)}{\partial t} = \lim_{\tau\to 0}\frac{P_1(y,t+\tau)-P_1(y,t)}{\tau} \tag{1.10}$$

and writing $P_1(y,t)$ and $P_1(y,t+\tau)$ in the form

$$P_1(y,t) = \int dy' P_{1|1}(y,t|y',t)P_1(y',t), \tag{1.11}$$

$$P_1(y, t+\tau) = \int dy' P_{1|1}(y, t+\tau|y', t) P_1(y', t) \tag{1.12}$$

yields

$$\frac{\partial P_1(y,t)}{\partial t} = \int dy' P_1(y', t) \lim_{\tau \to 0} \frac{P_{1|1}(y, t+\tau|y', t) - P_{1|1}(y, t|y', t)}{\tau}. \tag{1.13}$$

From Eq.(1.11) we find that the expression $P(y, t|y', t)$ works as a delta function. Thus, we can write

$$P_{1|1}(y, t|y', t) = \delta(y - y'). \tag{1.14}$$

To calculate the $P_{1|1}(y, t+\tau|y', t)$ part of the integration in Eq.(1.13), we use an ansatz for the first order in τ [6]:

$$P(y, t+\tau|y', t) = A(\tau)\delta(y - y') + \tau w_t(y' \to y) \tag{1.15}$$

Here $w_t(y' \to y)$ is the transition rate for the system to transit from y to y' during the time interval $[t, t+\tau]$. $A(\tau)$ is a coefficient to be determined.

According to the normalization property of the conditional probability, we have

$$\int dy P(y, t+\tau|y', t) = 1 \tag{1.16}$$

Integrating both sides of Eq.(1.15) and comparing the result with Eq.(1.16), we obtain the following expression for $A(\tau)$:

$$A(\tau) = 1 - \tau \int dy'' w_t(y' \to y'') \tag{1.17}$$

Now, the expression for the ansatz in Eq.(1.15) has the form of

$$P(y, t+\tau|y', t) = [1 - \tau \int dy'' w_t(y' \to y'')]\delta(y - y') + \tau w_t(y' \to y) \tag{1.18}$$

Putting Eq.(1.14) and Eq.(1.18) back into Eq.(1.13), we obtain the master equation as follows:

$$\frac{\partial P_1(y,t)}{\partial t} = \int dy' [P_1(y', t) w_t(y' \to y) - P_1(y, t) w_t(y' \to y)] \tag{1.19}$$

The first part of the integration of Eq.(1.19) shows the effect on $\partial P_1(y,t)/\partial t$ of the system transiting from other states to the current state, whereas the second part shows the effect of the system transiting from the current state y to other states y'.

For the continuous-time discrete-micro-state system, we can simply convert the integral sign into a summation sign, and change y, y' into n, n' [6]:

$$\frac{\partial P_n(t)}{\partial t} = \sum_{n'} P_{n'}(t) w_{n'n} - P_n(t) \sum_{n'} w_{nn'}. \tag{1.20}$$

Here $P_n(t)$ is the probability for the system to be in state n at time t, and $w_{nn'}$ is the transition rate for the system to transit from state n to state n'. More discussion of Eq.(1.20) can be found in Chapter 2.

1.4 Systems in and out of Equilibrium

In the past century, physicists have developed a rich understanding of equilibrium systems. In this dissertation we focus on systems that exchange energy with the environment (heat bath).

In 1871, Ludwig Boltzmann published a paper describing the concept of canonical ensemble [7] for such an equilibrium system. This concept was intensively studied by Josiah Willard Gibbs [8] in 1902. Starting from counting the number of micro-states in a canonical ensemble with fixed temperature and fixed number of particles, one can derive the probability $P(E)$ for a system to have energy E. The canonical partition function can be obtained by normalization of $P(E)$ and facilitates the derivation of different state functions [9].

Besides the study of gas-liquid-solid systems [10], physicists also studied a wide range of other physical systems, such as lattice gas systems, magnetic systems [11], spin glass [12],

etc. To study the equilibrium phase transitions and critical phenomena, renormalization group analysis and numerical methods have been used with great success [13].

However, most systems in nature are non-equilibrium systems, where detailed balance is broken in one way or another. The theoretical framework for explaining the dynamical behaviors of these systems is still elusive. In recent years, statistical physicists have investigated non-equilibrium processes in a variety of simple models. These models include: the Ising system driven by an oscillating magnetic field [16, 17], the driven lattice gas [18, 19], models for non-equilibrium growth processes [20, 21], etc. In this dissertation, we will discuss our research of two different models where energy input from the environment is not spatially uniform. The first model, studied in Chapter 3, involves a two-dimensional two-temperature Ising lattice gas system where energy is inputted to the system from the interface. The second one, investigated in Chapter 4, is designed to study the effects of magnetic friction on the surfaces of magnets. Both of the models are studied through Markov chain Monte Carlo simulations, which will be introduced in Chapter 2.

Chapter 2

Numerical Methods

In this Chapter, we first discuss the conditions for a system to reach a stationary or equilibrium state. The detailed balance condition is derived. We then explain how the Glauber Algorithm and the Metropolis Algorithm successfully produce a process that satisfies the detailed balance condition. After that, concepts of Glauber Dynamics and Kawasaki Dynamics are introduced which effectively utilize this type of algorithm to study equilibrium processes. We also show how we implement similar ideas in Monte Carlo simulations of non-equilibrium systems.

2.1 Detailed Balance

As has been shown in the previous chapter, for a system whose state changes continuously we can derive the system's master equation from the Chapman-Kolmogorov equation [4,5]. For a system with a countable number of states, we can write the master equation in the

following form

$$\frac{dP_k(t)}{dt} = \sum_{\substack{l=1 \\ l\neq k}}^{N} [w_{kl}P_l(t) - w_{lk}P_k(t)] \tag{2.1}$$

Here $P_k(t)$ is the probability for the system to be in state k at time t and w_{lk} is the transition rate from state k to state l.

The condition for a system to be a in stationary state follows by setting the left side of Eq.(2.1) equal to zero:

$$\frac{dP_k(t)}{dt} = 0 \tag{2.2}$$

$$\Rightarrow \sum_{l\neq k} [w_{kl}P_l(t) - w_{lk}P_k(t)] = 0 \tag{2.3}$$

This means, when a system is in a stationary state, it is allowed that there is a probability current $(w_{kl}P_l(t) - w_{lk}P_k(t))$ that flow from one state to another, as long as Eq.(2.3) is satisfied.

However, for systems that are kept in an equilibrium state, a much stronger condition needs to be satisfied. That is called the *detailed balance condition*:

$$w_{kl}P_l(t) = w_{lk}P_k(t) \tag{2.4}$$

Thus, for a system in equilibrium, the net probability current for the process to transit from one state to another should be zero.

With the detailed balance condition in Eq.(2.4) satisfied, it follows that all bracketed terms on the right hand side of Eq.(2.1) are reduced to zero. As a result, $\frac{dP_k(t)}{dt} = 0$, meaning the probability for the system to be in a given state does not change with time. In other words, a system that is in an equilibrium state is also in a stationary state.

As far as we are studying equilibrium systems at a fixed temperature and with a fixed number of particles, the probability to find the system in a given state is given by the canonical distribution (Boltzmann distribution). The probability for a system to be in a state (labeled by k) is then

$$P(k) = \frac{e^{-\beta H(k)}}{\sum_{l=1}^{M} e^{-\beta H(l)}} \tag{2.5}$$

Here, M is the total number of states that can be found in the system. In $\beta = \frac{1}{k_B T}$, T is the temperature of the heat bath. $H(k)$ is the system's energy in state k. The denominator of the right hand side of Eq.(2.5) is the canonical partition function $Z = \sum_{l=1}^{M} e^{-\beta H(l)}$. With that, we can write down the detailed balance condition for a system that is in equilibrium with a heat bath (with a temperature of T) in the following way:

$$w_{kl} e^{-\beta H(l)} = w_{lk} e^{-\beta H(k)} \tag{2.6}$$

Hence, to simulate a system that is in equilibrium with a heat bath, we need to find an algorithm that can generate a sequence of states with rates that satisfy Eq.(2.6).

2.2 Glauber Algorithm

The Glauber algorithm is one of the algorithms that produces transition rates satisfying Eq.(2.6) . The expression for w_{lk} is usually written as [22]:

$$w_{lk} = \frac{e^{-\beta[H(l)-H(k)]}}{1 + e^{-\beta[H(l)-H(k)]}} \tag{2.7}$$

If we exchange the index k and l in the last equation, we immediately obtain the transition rate w_{kl}:

$$w_{kl} = \frac{e^{-\beta[H(k)-H(l)]}}{1 + e^{-\beta[H(k)-H(l)]}} \tag{2.8}$$

If we put these expressions for w_{lk} and w_{kl} back into Eq.(2.6), we find that both sides of Eq.(2.6) turn out to be $\frac{1}{e^{\beta H(k)}+e^{\beta H(l)}}$. Thus, detailed balance is satisfied by the Glauber algorithm.

In general, the Glauber algorithm generates processes that satisfy the detailed balance condition for canonical systems.

2.3 Metropolis Algorithm

In 1953, Nicholas Metropolis, Arianna W. Rosenbluth, Marshall N. Rosenbluth, Augusta H. Teller, and Edward Teller published a paper in the Journal of Chemical Physics named *Equation of State Calculations by Fast Computing Machines* [23]. In this paper, the probability for a system to transit from an equilibrium state k to an equilibrium state l is given by:

$$w_{lk} = \min\{1, e^{-\beta[H(l)-H(k)]}\} \tag{2.9}$$

This means, if the energy increases, the transition probability is $e^{-\beta[H(l)-H(k)]}$. Otherwise if the energy decreases, the transition probability is one and the proposed change is always accepted.

It is not hard to see that the Metropolis algorithm conforms to detailed balance. Assuming $H(l) > H(k)$, the probability that the system transits from state k to state l is $w_{lk} = e^{-\beta[H(l)-H(k)]}$, whereas the probability for the system to transit from state l to state k is $w_{kl} = 1$. If we put the expressions for w_{lk} and w_{kl} back into Eq.(2.6), we have that the left hand side equals the right hand side. It is easily shown that the same holds true for $H(l) < H(k)$.

In other words, like the Glauber algorithm, the Metropolis algorithm also generates pro-

cesses that satisfy the detailed balance condition for canonical systems.

2.4 Non-conserved (Glauber) Dynamics

In Ising systems each lattice site is characterized by a variable that can take one of two possible states. In Potts systems the variable at each lattice site can take one of q ($q > 2$) possible states. For non-conserved or Glauber dynamics a lattice site is randomly chosen and its state is changed, following for example the rules of the Metropolis algorithm [24].

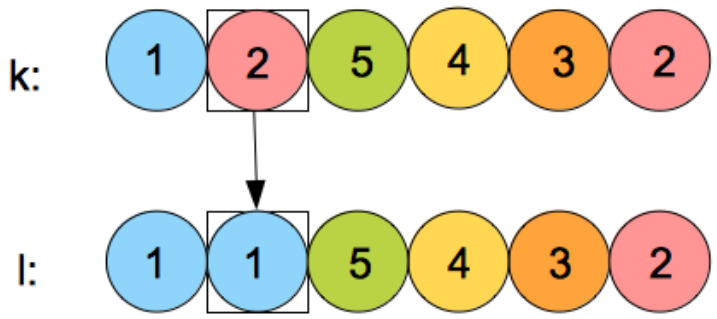

Figure 2.1: Schematic picture of Glauber dynamics in a one-dimensional Potts system.

Fig.2.1 shows an example of Glauber dynamics in a one-dimensional Potts chain. We assume that there are 6 lattice sites on this Potts chain and the variable S_i characterizing each lattice site i can take one of five possible values, i.e. $S_i = 1, 2, 3, 4,$ or 5. Assume that this system is initially in some state k (see Fig.2.1). According to Glauber dynamics, we first randomly choose one site for update (the second site in Fig.2.1). Then we try to transit from state k into state l by replacing $S_2 = 2$ with $S_2 = 1$. Here, Glauber dynamics dictates us to accept the new state with the Metropolis rate (or the Glauber rate). In the next step, we randomly choose another site and try to update that site with the same rule.

In short, Glauber dynamics is a combination of randomly choosing an element of the system and updating that element in a way that detailed balance is satisfied.

2.5 Conserved (Kawasaki) Dynamics

In contrast to Glauber dynamics, which involves the update of the state of one element of the system at a time, conserved or Kawasaki dynamics involves the update of two neighboring elements at the same time [25]. In other words, for a Ising or Potts system, Kawasaki dynamics means that two neighboring lattice sites are randomly chosen and their states are exchanged according to the Metropolis algorithm (or the Glauber algorithm).

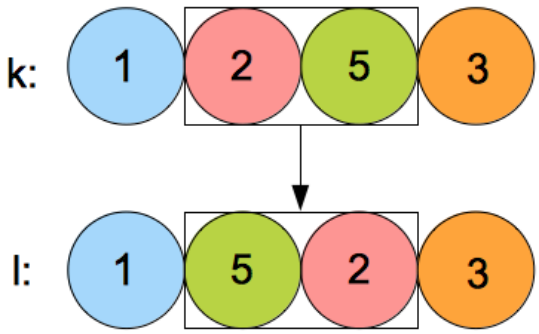

Figure 2.2: Schematic picture of Kawasaki dynamics in a one-dimensional Potts system.

In Fig.2.2, we show how Kawasaki dynamics works in a one-dimensional Potts system. We assume there are only 4 lattice sites in this Potts chain and each site can take one of 5 possible states. In a process that is dictated by Kawasaki dynamics, we first randomly choose two neighboring sites. Next, we check the state of each chosen site. If the two sites have different states, the two sites exchange their states with each other following the Metropolis criterion. See Fig.2.2, where starting from a state k, the second and third sites of the Potts chain are chosen and their states are exchanged.

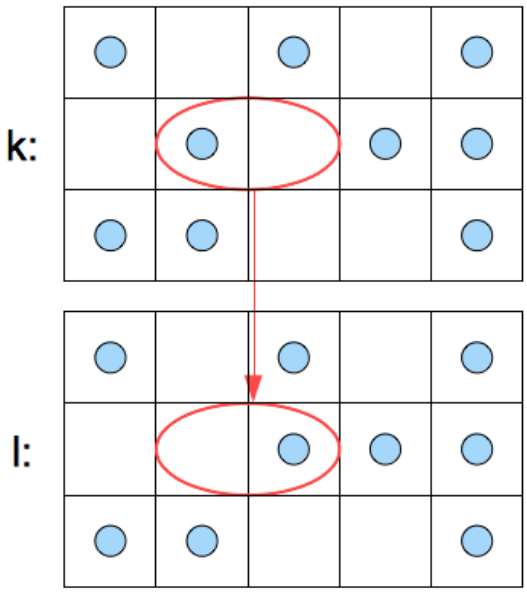

Figure 2.3: Evolution of a two-dimensional lattice gas system governed by Kawasaki dynamics.

In Fig.2.3, we show how Kawasaki dynamics works in a two-dimensional lattice gas. At each site of the two-dimensional lattice the state variable can take one of the two possible occupancy states, namely $S_{i,j} = 1$, when the site (i, j) is occupied by a particle, and $S_{i,j} = -1$, when the the site (i, j) is unoccupied. In a process governed by Kawasaki dynamics, we first randomly choose two neighboring sites and then exchange their occupancy states following the Metropolis criterion. In other words, if the chosen neighboring sites have different occupancy states, one particle will be moved to the neighboring site with a probability that satisfies Eq.(2.9).

To sum up, Kawasaki dynamics is a combination of randomly choosing two neighboring elements of the system and exchanging the states of these elements in a way that satisfies detailed balance.

2.6 Monte Carlo Simulation

Monte Carlo simulations are widely used in computational physics, mostly for simulating many-body systems. These are computational experiments that can produce discrete time series for a dynamical system [26]. One way to achieve this is through importance sampling, where different events take place with pre-assigned probabilities.

In the following, we discuss how we implement algorithms for systems that are either in or out of equilibrium.

2.6.1 Monte Carlo Simulation for Equilibrium Systems

As shown in the previous subsections, for a canonical system in equilibrium we can use either the Glauber algorithm or the Metropolis algorithm as the appropriate scheme to produce events where the detailed-balance condition and the rule of importance sampling are satisfied simultaneously. (The rule of importance sampling for a canonical system follows from Eq.(2.5).) Accordingly, we implement the Monte Carlo simulation for equilibrium systems as follows:

(1) Set up system parameters and initialize the state for each element of the system; set the counting number $c = 1$.

(2) Randomly choose an element (a neighboring element pair in Kawasaki dynamics) for update.

(3) For the given dynamics, use the appropriate updating scheme to update the state of the chosen element (element pair).

(4) The update of this element (element pair) is complete. If c is smaller than the expected

total number of updates, add 1 to c and go back to (1).

In the following, we will give some examples to show how we implement step (2) and step (3) for different models.

Monte Carlo Simulation for Ising Systems in Equilibrium

There are two particular features for the Ising systems in equilibrium. First, the variable characterizing each lattice site can take only one of two possible values. Second, the system is in contact with a heat bath at a given temperature T. With these two features in mind, we can choose the Metropolis algorithm for updating the system.

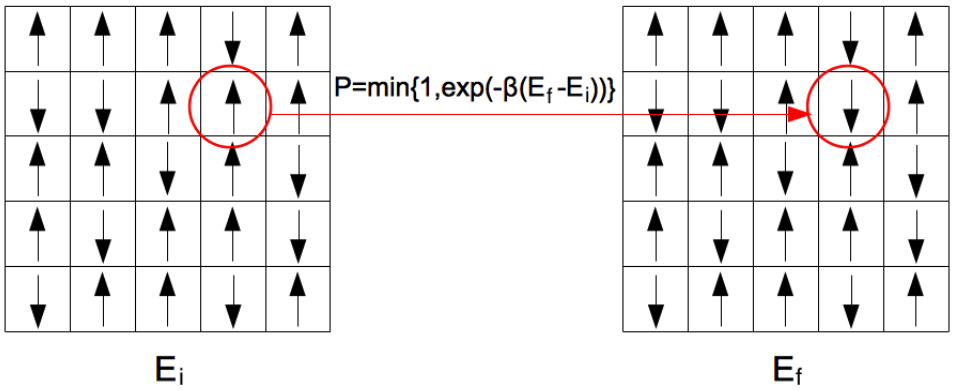

Figure 2.4: Monte Carlo simulation for the two-dimensional Ising model in equilibrium, where spin flips are done according to Metropolis algorithm. The system temperature is T, and $\beta = 1/k_B T$.

Consider, for example, the two-dimensional Ising system with Glauber dynamics (see Fig.2.4). At the beginning of an update, the system has the initial energy E_i (as shown in Fig.2.4). Then, we randomly choose a site and calculate the energy E_f the system would have after flipping the spin characterizing the chosen site. According to the Metropolis algorithm, if $E_f < E_i$, we accept the proposed update with probability 1. If $E_f > E_i$, we

accept the update with probability $e^{-\beta(E_f-E_i)}$.

Monte Carlo Simulation for Potts Systems in Equilibrium

The striking difference between a Potts system and an Ising system is that a Potts system usually has more than two available states for each element. As a result, we choose an improved version of the Glauber algorithm for updating the configuration of the system.

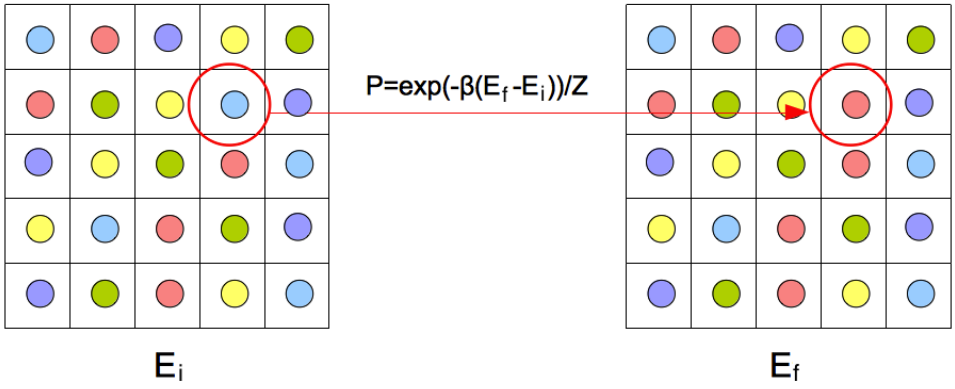

Figure 2.5: Monte Carlo simulation for the two-dimensional Potts model in equilibrium, where spin flips are done according to Glauber algorithm. The system temperature is T, and $\beta = 1/k_BT$.

Fig.2.5 shows schematically a two-dimensional Potts system in equilibrium. Since we are now updating the states of the elements of a Potts lattice, we need to consider different outcomes for the update. According to the Glauber algorithm, if the system starts with a configuration that results in energy E_i, we should randomly choose one new state and calculate the probability for the system to transit to that state. For that we need to calculate the energy E_f for the proposed new configuration. Now we can calculate the probability for the system to transit to that state according to Eq.(2.7), which gives $\frac{e^{-\beta(E_f-E_i)}}{1+e^{-\beta(E_f-E_i)}}$. Finally we make the decision on accepting the new state by generating a random number X with a uniform distribution and comparing it with $\frac{e^{-\beta(E_f-E_i)}}{1+e^{-\beta(E_f-E_i)}}$.

To expedite the computation, in the improved version of the Glauber algorithm we consider all the possible states for update. Instead of choosing one particular state for update in each step, we assign a probability for the system to transit to each of the possible states. The improved algorithm goes as follows: for a system whose elements can take q states, at the beginning of the update we calculate the energy for all possible new states, such as E_0, E_1, E_2, ..., E_{q-1}. Then, we define different probability windows and compute a random number X$\in (0,1]$, drawn from a uniform distribution. If X falls into the first window, the system will be updated to state 0, if X drops into the second one, the system will be updated into state 1, etc. Once the update is done, the next update will start, in which a newly selected lattice site also has q states to choose from.

The probability windows are calculated based on the initial energy E and the new configurations' energies. They are expressed as follows:

$$\begin{aligned} &(0, \frac{e^{-\beta(E_0-E)}}{Z'}], \\ &(\frac{e^{-\beta(E_0-E)}}{Z'}, \frac{e^{-\beta(E_0-E)}+e^{-\beta(E_1-E)}}{Z'}], \\ &(\frac{e^{-\beta(E_0-E)}+e^{-\beta(E_1-E)}}{Z'}, \frac{e^{-\beta(E_0-E)}+e^{-\beta(E_1-E)}+e^{-\beta(E_2-E)}}{Z'}], \\ &...,(\frac{e^{-\beta(E_0-E)}+e^{-\beta(E_1-E)}+...+e^{-\beta(E_{q-2}-E)}}{Z'}, 1] \end{aligned} \tag{2.10}$$

where $Z' = \sum_{i=0}^{q-1} e^{-\beta(E_i-E)}$. If we assume the system to be initially in state i, subtractions of the upper and lower bounds of the probability windows in Eq.(2.10) immediately gives:

$$\frac{e^{-\beta(E_0-E_i)}}{Z'}, \frac{e^{-\beta(E_1-E_i)}}{Z'}, \frac{e^{-\beta(E_2-E_i)}}{Z'}, ..., \frac{e^{-\beta(E_{q-1}-E_i)}}{Z'} \tag{2.11}$$

2.6.2 Monte Carlo Simulation for Non-equilibrium Systems

In the last section, we discussed the implementation of Monte Carlo simulations for canonical equilibrium systems. In this kind of systems, the Monte Carlo simulation produces a series of configurations whose probabilities of occurrence, in a large time limit, reproduce

the Boltzmann distribution. However, in the non-equilibrium systems studied in this thesis, the systems are driven out of equilibrium constantly. In this thesis, we mainly focus on systems that are driven out of equilibrium from the interfaces. In the following we present two examples that show how we implement Monte Carlo simulations for this kind of systems.

One-dimensional Two-temperature Ising Ring with Kawasaki Dynamics

One kind of non-equilibrium systems studied in this thesis involves non-uniform temperatures. One of the simplest models of this kind is the one-dimensional two-temperature Ising ring with Kawasaki dynamics, see Fig.2.6. In this sketch, the upper eight lattice sites are immersed in a heat bath with temperature T_1 (which is finite) and the lower eight lattice sites are immersed in another with temperature T_2 (which is infinite).

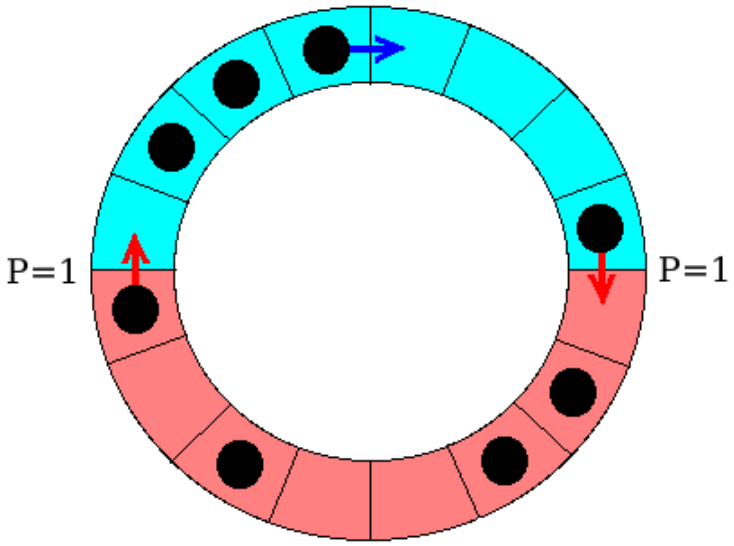

Figure 2.6: Schematic picture of the one-dimensional two-temperature Ising ring with Kawasaki dynamics.

Within a sector at a given temperature, the updating (particle hopping) process only involves the local configuration and the local temperature. (See the sites connected by the blue arrow in Fig.2.6.) Here Kawasaki dynamics works fine and the update favor local equilibrium. However, what will be the update protocol if one particle is in the T_1 (T_2) sector and one hole is in the T_2 (T_1) sector and these two sites are chosen for an update? (See the sites connected by the red arrows in Fig.2.6.) We know we can no longer use Kawasaki dynamics because the proposed process involves two temperatures, as both the Glauber and Metropolis algorithms in Kawasaki dynamics use only one fixed temperature T. As a result, we need to figure out new updating schemes (protocols) for this particular kind of updates.

In our simulations we simply set the hopping rate to be 1 if the particle wants to cross the interface, disregarding which side of the interface the particle is in. We set this updating scheme in order to make the behavior of the holes (sites being empty) the same as that of the particles. Once we have fixed the protocol on the interface, we can start to run the Monte Carlo simulation for this model. The simulation is run as follows:

(1) fix the system size, for example $M(= 2N$, N is the total number of particles);

(2) fix a temperature for the different sectors of the two-temperature system;

(3) label each site with an index according to the location, for example $i = 1, 2, ...M$;

(4) initialize the state for each site, such as using $S_i = 1$ to denote a site being occupied by a particle and $S_i = -1$ to denote a site being vacant;

(5) run the Monte Carlo steps.

In each Monte Carlo step, we do M updates. For each update, we do the following:

i. randomly choose two neighboring sites;

ii. if the two sites have the same occupation state, go to step i;

iii. if the chosen sites are in the same temperature sector, do the Kawasaki exchange with equilibrium rates;

iv. if the chosen sites are in two different temperature sectors, do the Kawasaki exchange with probability 1;

v. go to step i for the next update.

It is very important to point out that at the beginning of the simulation the system is not in any non-equilibrium steady state. We need to wait a certain relaxation time before the non-equilibrium steady state can be attained. In general, a long relaxation time is required before we can characterize a non-equilibrium steady state.

Two-dimensional Potts Lattices with Magnetic Friction

The second type of non-equilibrium systems studied in this work focuses on the magnetic friction between two Ising/Potts lattices. In this type of systems, usually one of the Ising/Potts lattices is moving against the other, which breaks and rewires the interfacial couplings. The following is a schematic picture of this situation.

Because the upper lattice is moving to the right with a velocity v, we have to rewire the interfacial couplings every time the movement happens. This is because we suppose the Ising/Potts lattice sites are always coupled to their nearest neighbors. Before the movement of the upper lattice, we have a Hamiltonian $H(t_1)$ written for the coupling configuration as shown on the left. After the movement of the upper lattice, another Hamiltonian $H(t_2)$ should be written for the new coupling configuration as shown on the right. It is obvious here that the Hamiltonian for such a system is time-dependent.

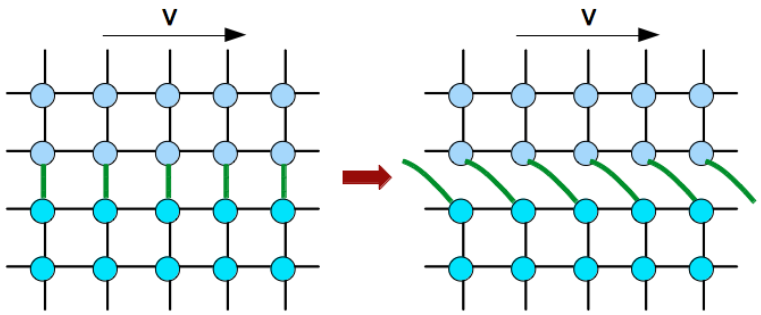

Figure 2.7: Schematic picture of the two-dimensional Ising/Potts system with magnetic friction.

Strictly speaking, the system is changed constantly by an external force. The energy created by rewiring the couplings during the movement should be equal to the work done by that force.

To facilitate the simulation of this kind of system, we make the important assumption that we can still use the Metropolis or Glauber protocol between consecutive movements. That is, we assume that the Hamiltonian of the system is time-independent between two consecutive movements of the upper lattice. Accordingly, the detailed balance condition holds in the short period between the two movements, and we can use the update protocols mentioned in this paragraph.

In the Monte Carlo simulation of this model, we therefore do the following:

(1) fix the height L and the width W of each two-dimensional Ising/Potts lattice;

(2) fix the temperature of the system;

(3) label each site with an index pair (x,y) according to the location, where $x = 1, ...W$, whereas $y = 1, ...L$;

(4) initialize the state for each site $i = (x, y)$ through a variable S_i that ranges from 0 to

$q-1$;

(5) run the Monte Carlo steps.

To facilitate the relative movement with speed v between the upper and lower lattices, we need to rewire the interfacial couplings v times every unit of time. This means, for a sweep of $L \times W$ updates in a Monte Carlo step, we should rewire the couplings after every $(L \times W)/v$ updates. Thus, during each Monte Carlo step, where $L \times W$ updates are undertaken, we need to:

i. set the counting number $c = 0$;

ii. if the remainder of c over $(L \times W)/v$ is zero, do the following two steps:

(a) rewire the interfacial couplings as shown in Fig.2.7;

(b) update the system's total energy.

otherwise skip ii;

iii. randomly choose one site of the system;

iv. update of the state of the chosen site with Metropolis/Glauber algorithm;

v. increase c by 1 and go to step ii for the next update.

Instead of simply rewiring the connections at the interface, we could also shift all the spins in the upper half by one lattice constant. However, this procedure would be way more computer time intensive.

To sum up, the Monte Carlo simulation for canonical equilibrium systems involves local updates with an updating criterium which fulfills detailed balance. If the Hamiltonian

becomes a function of time or if the system takes on more than one temperature, detailed balance is broken and the system ends up in a non-equilibrium steady state.

Chapter 3

Two-dimensional Two-temperature Ising Lattice Gas

In this chapter we present our research on the two-dimensional two-temperature lattice gas model. In this model, energy is constantly pumped into the system locally at the interface between the two halves of the system, while each half of the system is in contact with a heat bath at a different temperature. My numerical study shows different non-equilibrium states emerging because of the constant energy input at the interface. Especially, when the system size and the system temperatures are in certain ranges, we can observe novel non-equilibrium steady states where stripe shaped patterns show up in one half of the system. The main results of this chapter have been summarized in the paper [28]

3.1 Model and Background

In our model we have a two-dimensional Ising lattice whose energy is given by the Hamiltonian:

$$H = -J \sum_{x,y} (S_{x,y} S_{x+1,y} + S_{x,y} S_{x,y+1}) \tag{3.1}$$

In this Hamiltonian, the spin $S_{x,y} = \pm 1$ characterizes the state of the site located at (x, y), while J quantifies the coupling strength between neighboring sites. Only short range interactions happen in this system, and the change of a spin can only change the local energy between the spin itself and its four neighboring sites. The local energy for a site located at (x, y) is given by:

$$H_{x,y} = -J(S_{x,y} S_{x+1,y} + S_{x,y} S_{x-1,y} + S_{x,y} S_{x,y+1} + S_{x,y} S_{x,y-1}) \tag{3.2}$$

Our model is an Ising lattice gas system where the number of particles is conserved. Accordingly, $S_{x,y} = +1$ stands for a lattice site being occupied, while $S_{x,y} = -1$ stands for a lattice site being unoccupied. If we set the total number of particles to be equal to half of the number of sites in the lattice, we have zero "magnetization" for the system:

$$M = \frac{\sum_{x,y} S_{x,y}}{N} = 0 \tag{3.3}$$

Here N is the total number of sites in the system. Another important feature of our model is that our lattice system is in contact with two different temperature baths, see Fig. 3.1.

If we set the width of the system to be $2W$ and the length of the system to be $2L$, there are $N = 4LW$ sites in the system as shown in Fig.3.1. Now, we immerse the upper sector with $2LW$ sites in a heat bath with a finite temperature $T = T_0$, whereas the lower sector with $2LW$ sites is in contact with a heat bath at infinite temperature $T = \infty$. Kawasaki dynamics is governing the evolution of the system when the updates are done in each of the two sectors. (See the arrows pointing in horizontal directions in Fig.3.1

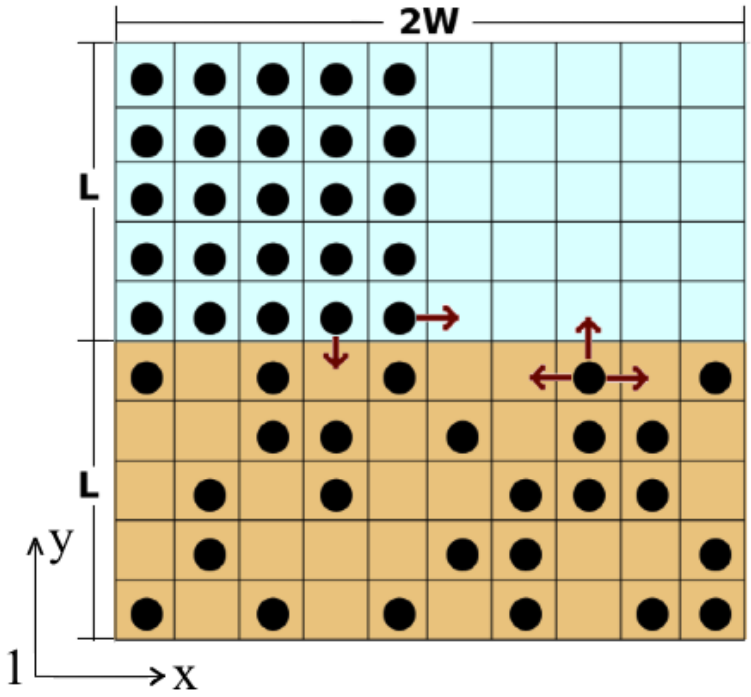

Figure 3.1: Schematic picture of the two-dimensional two-temperature Ising lattice gas. The upper sector (with lattice sites in blue) has a temperature of $T = T_0$, whereas the lower sector (with lattice sites in orange) has a temperature of $T = \infty$

for illustration.) However, if the update of the system involves sites in both sectors (see the arrows pointing in vertical directions in Fig.3.1 for illustration), this process can no longer follow Kawasaki dynamics because of the lack of a well defined temperature.

For this special kind of updates each Kawasaki exchange would involve two different temperatures (see the updates highlighted by the blue and red circles in Fig.3.2). The updating schemes for equilibrium systems (such as the Glauber algorithm or the Metropolis algorithm) fail to work since they all assume a single temperature when computing the acceptance rates. In our model, we set the probability for a particle to hop between sectors to one, independent on how the total energy is changed. In this way, detailed balance is not fulfilled at the interface, and, as a result, energy is pumped into the system

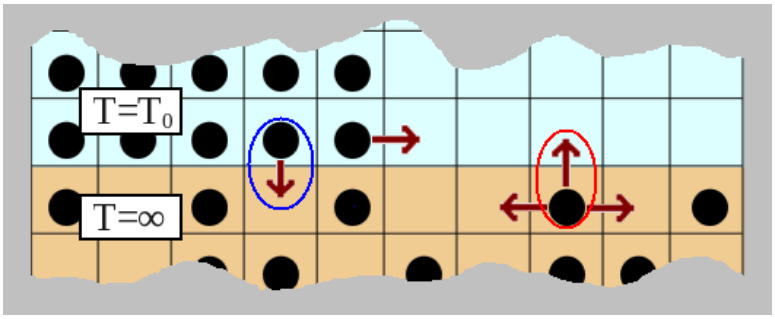

Figure 3.2: Illustration of the interface-crossing updates. The update highlighted in the blue circle illustrates a process in which one particle hops from the upper sector to the lower sector. The update highlighted in the red circle illustrates a process in which one particle hops from the lower sector to the upper sector.

at the interface.

Periodic boundary conditions are implemented on all four sides of the two-dimensional lattice. For the initial configuration we group $N/4$ particles on the left corner of the upper sector of the lattice and spread another $N/4$ particles randomly among the sites of the lower sector of the lattice. Thus, we prepare the system in the upper half in the $T = 0$ equilibrium configuration, whereas the initial configuration in the lower half is the $T = \infty$ equilibrium configuration.

Before discussing my results for this model, I want first to introduce some background information. In 2010, a paper published by M. Pleimling, et al., showed the appearance of convection cells in the same two-dimensional two-temperature Ising lattice gas system, but with a different boundary condition [27].

In that paper, in order to stabilize the convection cells that are moving along the boundary between the hot and cold sectors, the states of the spins located at the top row of the cold sector are fixed from the very beginning. That is to say (see Fig.3.1), the spins in the first half of the top row are kept in the state $S_{x,2L} = 1$ ($x \in [1, W]$), whereas the spins

in the second half of the top row are in the state $S_{x,2L} = -1$ ($x \in [W+1, 2W]$). With this *pinned* boundary condition all the updates that involve spins in the top row of the lattice are forbidden, and as a result the bulk cluster on the left hand side of the cold sector can neither be moved nor broken. After setting up this boundary condition, the authors measured the *probability current* $\vec{j}(x,y) = (j_x(x,y), j_y(x,y))$ and calculated the *average vorticity* $\langle w(x,y)\rangle$ at each location of the system. The symbol $\langle ...\rangle$ denotes taking both time and ensemble averages. The relation between the vorticity and the probability current is given as follows:

$$w(x,y) \equiv j_x(x,y) + j_y(x+1,y) - j_x(x,y+1) - j_y(x,y). \tag{3.4}$$

Further, the authors introduced the *average scalar stream function* $\langle \psi(x,y)\rangle$, which is related to the probability current [27] in the following form:

$$j_x(x,y) = \partial_y \psi(x,y) \tag{3.5}$$

$$j_y(x,y) = -\partial_x \psi(x,y) \tag{3.6}$$

It is not hard to find from Eq.(3.5) and Eq.(3.6) that $\vec{j}(x,y)$ is the vector that we obtain when taking the gradient of ψ and rotating the resultant vector by 90°. Accordingly, the average scalar stream function was calculated through numerical integration once the data for $j_x(x,y)$ and $j_y(x,y)$ were obtained from simulations.

The data for the average scalar stream function and the average vorticity obtained in [27] are shown in Fig.3.3. Fig.3.3(a) and Fig.3.3(b) show $\langle \psi(x,y)\rangle$ and $\langle w(x,y)\rangle$ for a system with $W = L = 25$ and $T_0 = 0.88T_c$, where $T_c \approx 2.269$ is the critical temperature of the classical two-dimensional Ising model. In Fig.3.3(a), one peak is observed around $x = y = 25$ and one trough is observed around $x = 1, y = 25$ (this is the same trough as that at $x = 50, y = 25$ because of the periodic boundary condition in the x direction). This means that there is a counterclockwise vortex around (25, 25) and there is a clockwise vortex around (1, 25).

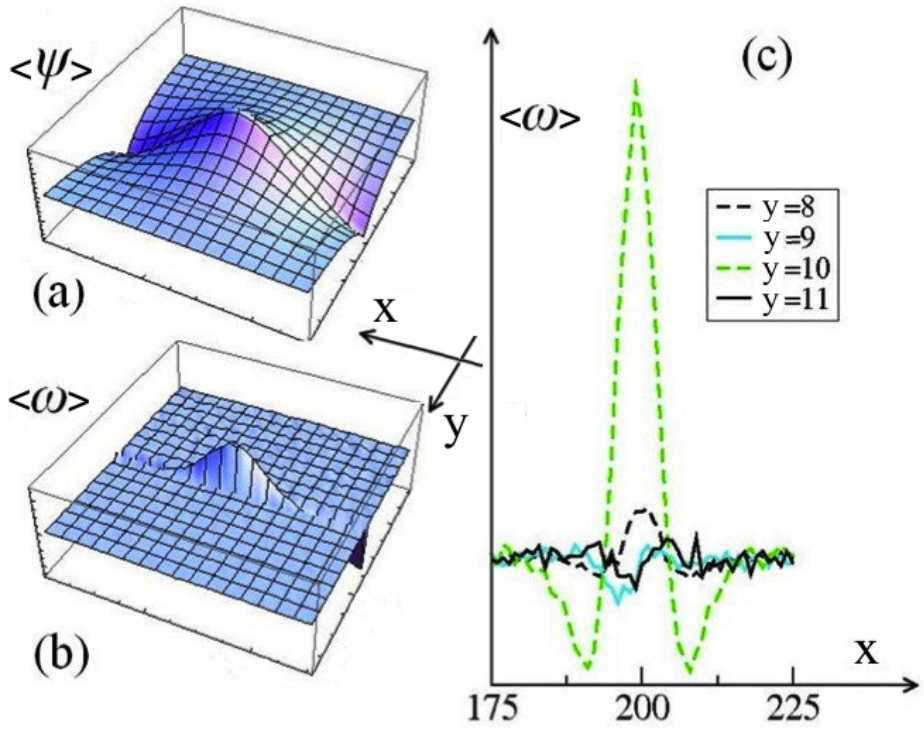

Figure 3.3: (Figure from [27], reprinted with permission from IOP Publishing.) Persistent currents and vortices present in a 50×50 system, with $T_0 \approx 0.88T_c$ and $T = \infty$, characterized by (a) the average stream function $\langle\psi(x,y)\rangle$ and (b) the average vorticity $\langle w(x,y)\rangle$. (c) Average vorticity in a 400×20 system: $\langle w(x,y)\rangle$ vs. x for several values of y, showing that the vortex is essentially localized at the sector boundary ($y = 10$), with counter-flow cells about 10 lattice spacing on either side of the primary vortex. Arbitrary units are used for both $\langle\psi\rangle$ and $\langle w\rangle$. The data for $\langle\psi(x,y)\rangle$ and $\langle w(x,y)\rangle$ presented in this figure are calculated numerically, based on the data for the probability current $\vec{j}(x,y) = (j_x(x,y), j_y(x,y))$ obtained in Monte Carlo simulations.

In Fig.3.3(b), we find that the values of $\langle w(x,y)\rangle$ are non-vanishing only along the interface between the two sectors. Again, for $\langle w(x,y)\rangle$, the peak is located around (25, 25) and the trough is located around (1, 25). To illustrate the localization of the non-vanishing values of the vorticity, data for $\langle w(x,y)\rangle$ are shown in Fig.3.3(c) for a system with $W = 200$ and $L = 10$. Clearly, the values of the vorticity decay very quickly to zero when moving away from the interface.

In summary, prior research with fixed boundary conditions has demonstrated that in a two-dimensional two-temperature Ising lattice gas system a non-equilibrium steady state can exist in the form of vortices that spread over the whole system. In the following section non-equilibrium states are studied in systems with periodic boundary conditions in both x and y directions. The following discussion greatly expands the published short account [28].

3.2 Non-equilibrium States

For the normal one-temperature two-dimensional Ising lattice gas with Kawasaki dynamics, the equilibrium state for temperatures smaller than the critical temperature $T_c(\approx 2.269)$ is a phase separated state. Yet, in our model, there is a constant energy input at the interfaces separating the two different sectors of the system. In fact, our simulation results show that the energy input at the interfaces influences not only the movements of particles near the interfaces, but also the movements of particles far away.

In our research, we extensively simulated the two-dimensional two-temperature Ising lattice gas for different combinations of system parameters. These system parameters include the system sizes L and W as well as the temperature T_0 of the upper (cold) sector.

Firstly, we simulated the Ising lattice gas at fixed temperatures for different system sizes

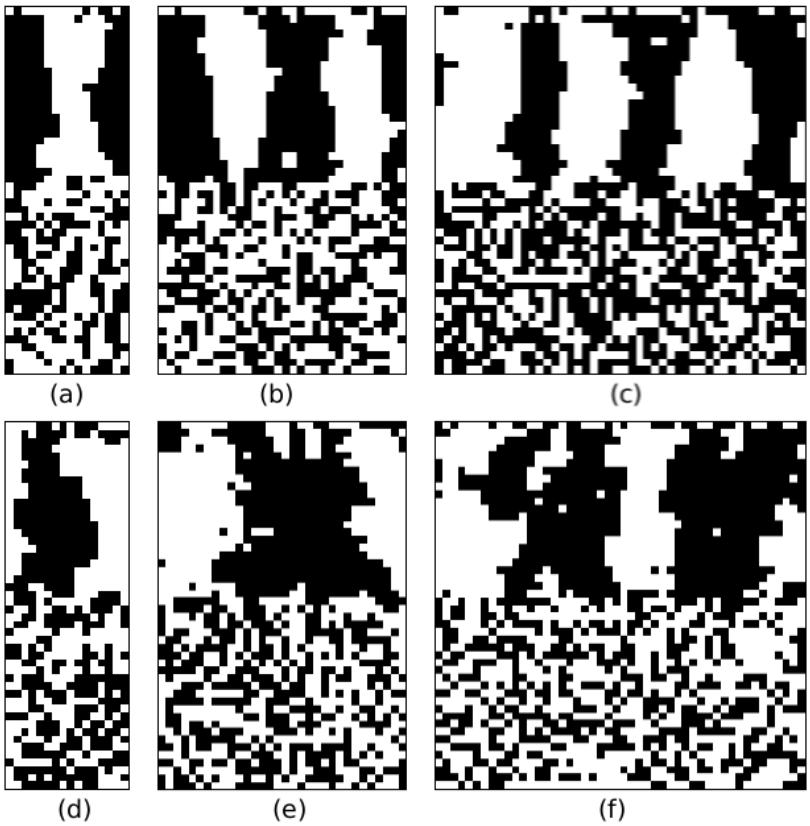

Figure 3.4: Snapshots of the two-temperature two-dimensional Ising lattice gas. In these simulations, the following system parameters are used: the system size is $L = 24$, the temperature is $T_0 = 0.5$ in (a)(b)(c) and $T_0 = 1.5$ in (d)(e)(f). We ran simulations for different system widths $W = 8, 16$, and 24.

W. The pictures in Fig.3.4 are snapshots of systems with $T_0 = 0.5$ (see Fig. 3.4 (a)(b)(c)) and 1.5 (see Fig. 3.4 (d)(e)(f)), $L = 24$, whereas $W = 8$, 16, and 24. Initially, one half of the particles is put in the left corner of the upper sector (forming a single cluster) and another half is distributed randomly in the lower sector. Each snapshot in Fig.3.4 is taken after 100,000 Monte Carlo steps since preparation of the system.

Interestingly, in the cases where $T_0 < T_c$, we find in our simulations that the system settles into a state where the single cluster in the upper sector is split into multiple clusters. This

is a long lived state. It is also found that if we keep all other parameters the same, the number of clusters formed after relaxation increases when increasing the width W of the system. As is shown in Fig.3.4, if $T_0 = 0.5$, the number of clusters (formed after relaxation) in the upper sector increases from 1 to 3 when increasing W from 8 to 24; and if $T_0 = 1.5$, the number of clusters (formed after relaxation) in the upper sector increases from 1 to 2 when increasing W from 8 to 24.

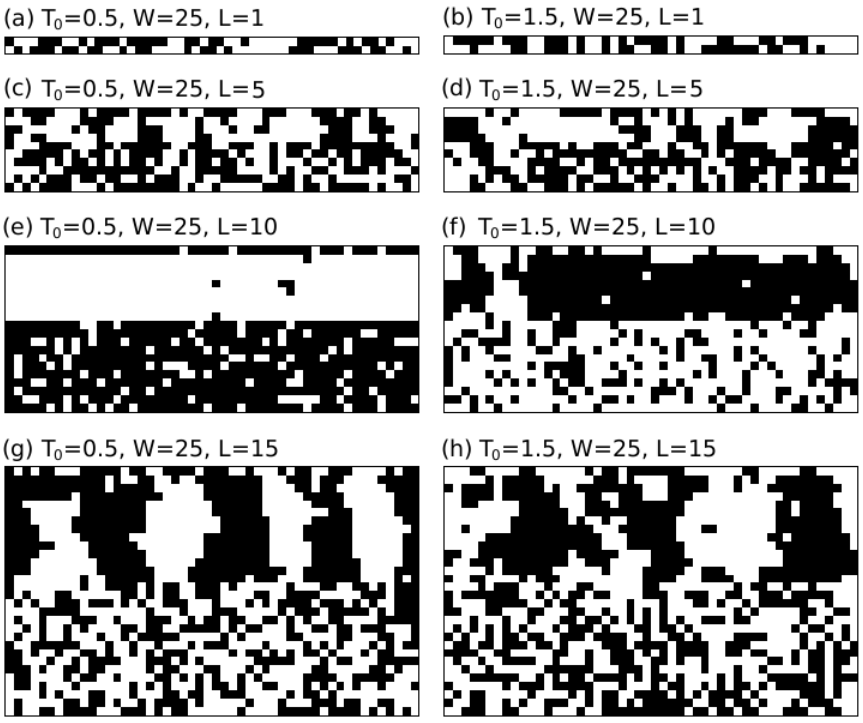

Figure 3.5: Snapshots of the two-temperature two-dimensional Ising lattice gas. In these simulations, the following system parameters are used: the system width is W=25, the temperature is T_0=0.5 in (a)(c)(e)(g) and T_0=1.5 in (b)(d)(f)(h). We ran simulations for different system sizes $L = 1, 5, 10$, and 15.

We also ran simulations for systems with fixed temperature $T_0 = 0.5$ (1.5), fixed size W(=25), but different sizes L(=5, 10, 15, 20 and 25). The corresponding snapshots are shown in Fig.3.5 and Fig.3.6. The initial conditions for these simulations were the same

Figure 3.6: Snapshots of the two-temperature two-dimensional Ising lattice gas. In these simulations, the following system parameters are used: the system width is $W = 25$, the temperature is $T_0 = 0.5$ in (a)(c) and $T_0 = 1.5$ in (b)(d). We ran simulations for different system sizes $L = 20$ and 25.

as before. The snapshots were taken after 100,000 Monte Carlo steps.

It is found in Fig.3.5 (a)(b)(c)(d) that when the system size L is 5 or less, particles in both sectors are moving randomly, forming no patterns at all after large relaxation times. However, as is shown in Fig.3.5 (e)(f), we find for $L = 10$ that almost all the particles in the system go to one sector, leaving the other sector almost vacant. Yet, if the size L is as large as 15, multiple clusters emerge in the upper sector. More snapshots with L=20 and 25 are shown in Fig.3.6. A comparison of the snapshots of systems with these larger

L values tells us that the number of formed clusters decreases as the size L increases. For example, when $T_0 = 0.5$, we have that the total number of stripe-shaped clusters decreases from 4 to 3 when L increases from 15 to 25; when $T_0 = 1.5$, we have that the total number of clusters decreases from 3 to 2 when L increases from 15 to 25.

We can also compare simulations for systems with fixed sizes ($W = L = 25$) and different values of T_0. The snapshots in Fig.3.7 show the following: if T_0=0.5, the system relaxes into a state where 3 separate clusters are formed in the upper sector; if T_0=1.5, the system relaxes into a state where 2 separate clusters are formed in the upper sector; if T_0=2.5, which is above the equilibrium critical temperature of the two-dimensional Ising lattice gas, the system under investigation relaxes into a state where no cluster can be clearly identified.

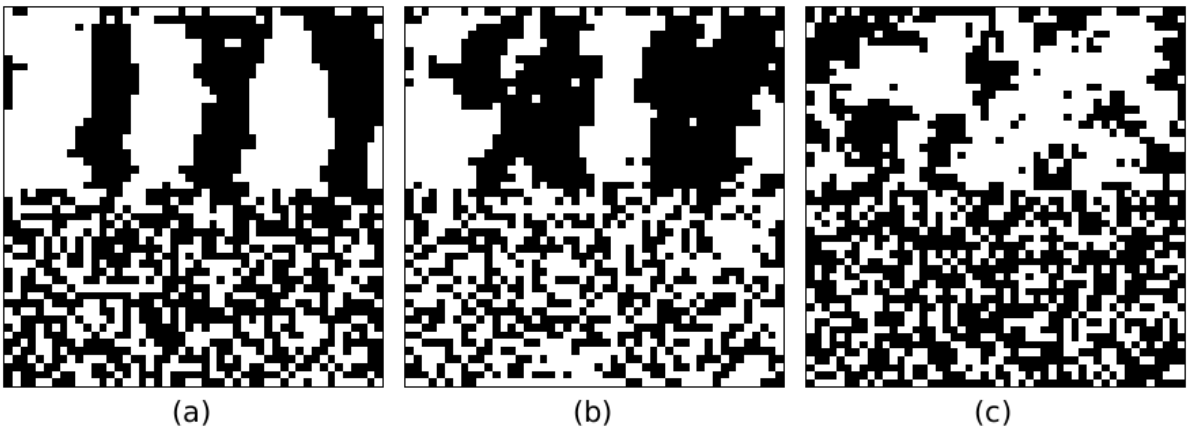

Figure 3.7: Snapshots of the two-temperature two-dimensional Ising lattice gas. In these simulations, W and L are kept fixed ($W = L = 25$), while the temperature T_0 is varied: T_0 =0.5, 1.5 and 2.5 from left to right.

In Fig.3.7 (c) we can find a noticeable particle density imbalance between the upper and lower sectors. That is to say, in the system as shown in Fig.3.7 (c), $M_{upper} < 0$, and $M_{lower} > 0$, where the magnetizations of the upper and lower sectors M_{upper} and M_{lower} are defined as:

$$M_{upper} = \frac{\sum_{x=1}^{2W} \sum_{y=L+1}^{2L} S_{x,y}}{2LW} \tag{3.7}$$

$$M_{lower} = \frac{\sum_{x=1}^{2W} \sum_{y=1}^{L} S_{x,y}}{2LW} \tag{3.8}$$

This means that the non-equilibrium state shown in Fig.3.7 (c) is not a state of complete disorder, even though the temperatures at both sectors are higher than the T_c of the classical two-dimensional Ising lattice.

In the following, we will characterize all the non-equilibrium states observed in the previous snapshots. The method of characterization will be discussed and a non-equilibrium finite-size phase diagram will be determined.

3.2.1 The Fully Disordered State

The previous examples show that the system can relax into different non-equilibrium states depending on the system parameters. One of the most obvious patterns observed is the *fully disordered state*.

As is found in Fig.3.5 (a)(b)(c)(d) and Fig.3.7 (c), the *fully disordered state* takes place in systems with small $L(< 10)$ or large $T_0(> T_c \approx 2.269)$. To better understand how a system reaches such a disordered state, we show in Fig.3.8 snapshots of the system at different times.

In this figure, we set $W = 60$, $L = 20$ and $T_0 = 2.5$. From Fig.3.8(a) to Fig.3.8(c), we find an obvious imbalance of particle density in the lower (hot) sector of the system, where the particle density is higher on the left side than on the right side. This signals that, at the very beginning (with $t <=100$), particles on the left of the system are flowing from the

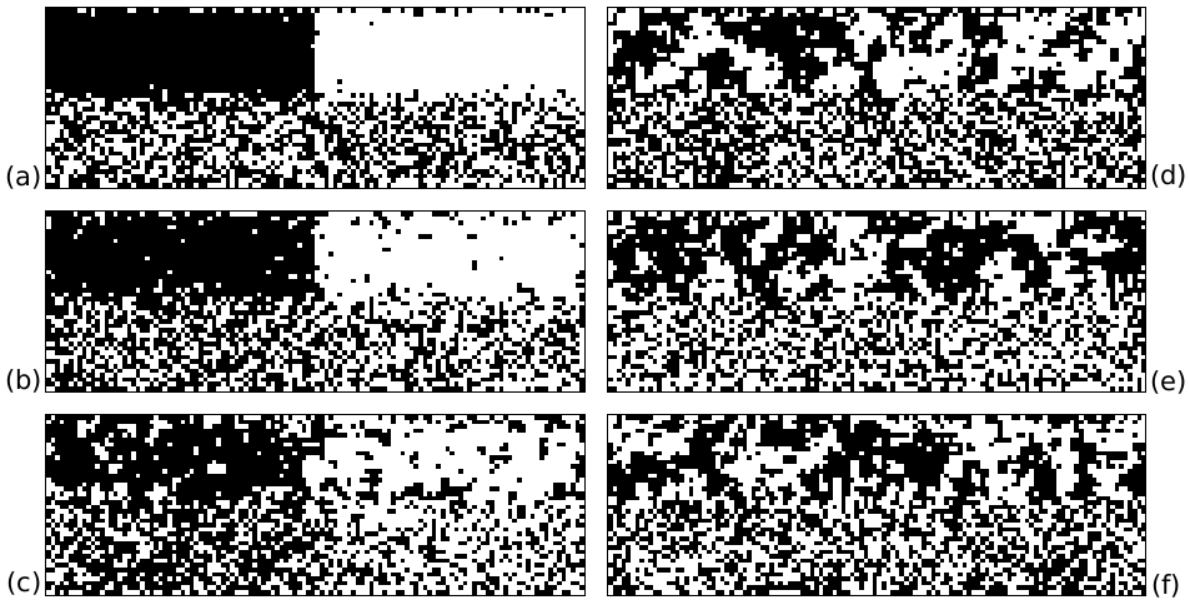

Figure 3.8: Snapshots of the two-temperature two-dimensional Ising lattice gas in a single simulation at different instants of time. The system parameters are $W = 60$, $L = 20$, and $T_0 = 1.0$. Figure (a)/(b)/(c)/(d)/(e)/(f) shows the snapshot taken after the 1^{st}/ the 10^{th}/ the 100^{th}/ the 1000^{th}/ the $10,000^{th}$/ the $100,000^{th}$ Monte Carlo step.

upper sector to the lower sector, and simultaneously particles on the right part start to flow from the lower sector to the upper sector. However, at later times, this imbalance of the particle density is gradually eliminated, until after a long relaxation time both sides are fully disordered, as is shown in Fig.3.8(f). The different sizes of the small clusters in the two sectors reveal the different values of the temperature-dependent correlation length.

3.2.2 The Fully Phase Separated State

In our simulations, we also find a *fully phase separated state*, as is shown in Fig.3.5 (e)(f). In general, we only observe this pattern when the system size L is relatively small

($L \approx 10$).

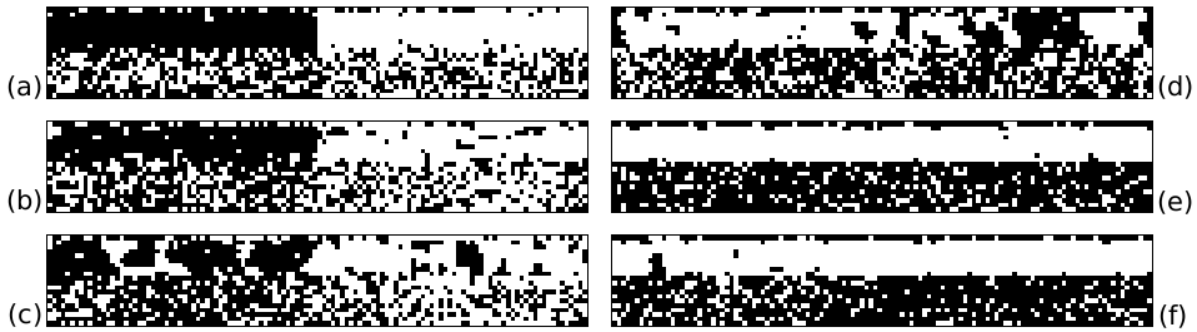

Figure 3.9: Snapshots of the two-temperature two-dimensional Ising lattice gas in a single simulation at different instants of time. The system parameters are $W = 60$, $L = 10$, and $T_0 = 1.0$. Figure (a)/(b)/(c)/(d)/(e)/(f) shows the snapshot taken after the 1^{st}/ the 10^{th}/ the 100^{th}/ the 1000^{th}/ the $10,000^{th}$/ the $100,000^{th}$ Monte Carlo step.

In Fig.3.9 we show snapshots of the simulation at different times. At the beginning of the evolution, an unbalanced particle density is again observed in the lower sector where the particle density is higher in the left part than in the right part, see Fig.3.9(a)(b)(c). This again reveals a flow of particles. Yet, in Fig.3.9(d), when the time reaches 1000 Monte Carlo steps, we can see that the particle densities become very unbalanced between the upper and lower sectors. In Fig.3.9(e) and (f) almost all particles are sitting in the lower sector. We can qualitatively understand this as caused by a particle current that is larger on the left side than on the right side, making the total particle number bigger in the lower sector than in the upper sector. Because of the symmetry of the Hamiltonian, particles may also accumulate in the upper sector, yielding a different equivalent non-equilibrium steady state.

3.2.3 The Modulated State

At last, we discuss the most interesting non-equilibrium state that we observed in our simulations. In Fig.3.10, we show the time evolution of a system with $W = 60$, $L = 30$, and $T_0 = 1.0$. Unlike before, we do not find an obvious particle density imbalance in the lower sector at the beginning of the evolution, compare Fig.3.10(a)(b)(c) with Fig.3.8(a)(b)(c) and Fig.3.9(a)(b)(c). Rather, after a short period, particle (hole) clusters

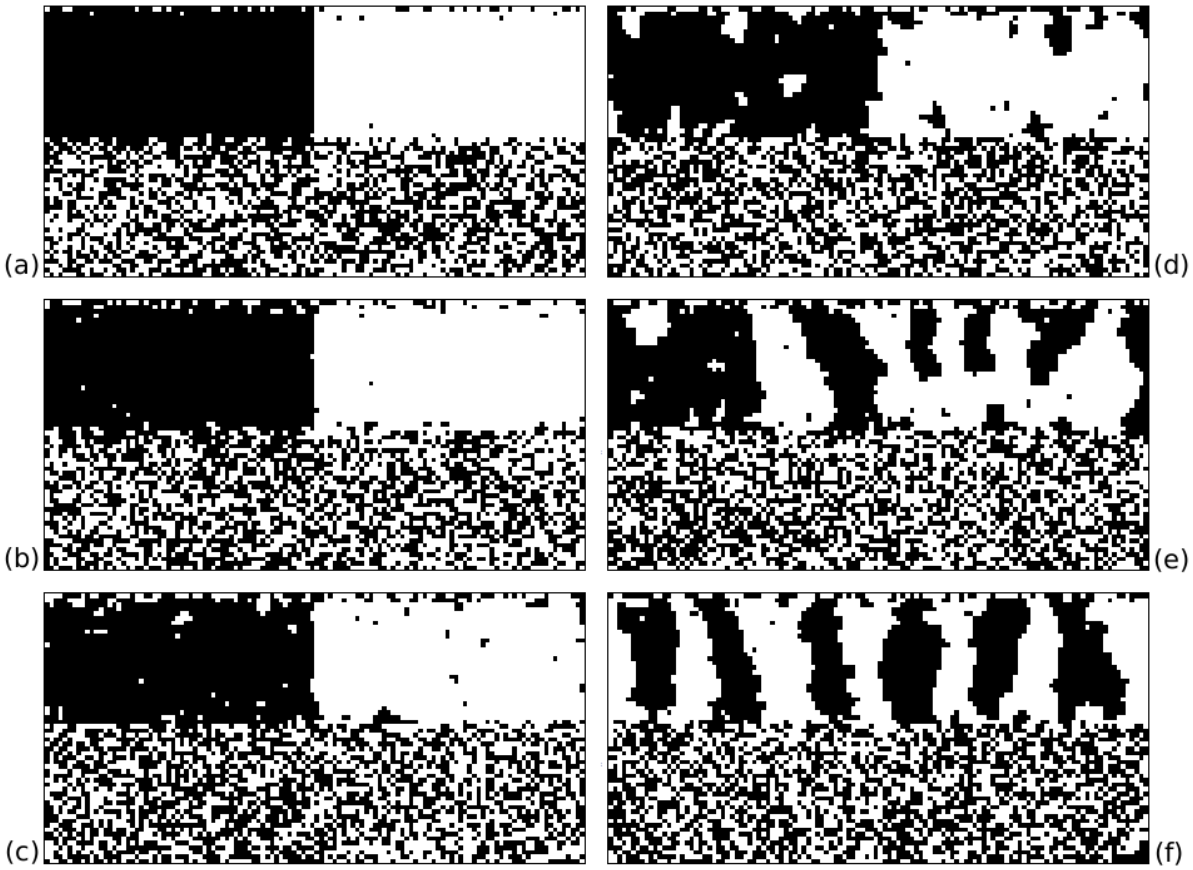

Figure 3.10: Snapshots of the two-temperature two-dimensional Ising lattice gas in a single simulation at different instants of time. The system parameters are $W = 60$, $L = 30$, and $T_0 = 1.0$. Figure (a)/(b)/(c)/(d)/(e)/(f) shows the snapshot taken after the 1^{st}/ the 10^{th}/ the 100^{th}/ the 1000^{th}/ the $10,000^{th}$/ the $100,000^{th}$ Monte Carlo step.

of smaller sizes are formed and start to extend to the empty part in the upper sector, see Fig.3.10(d) and (e). In fact, we can also understand the emergent clusters in the cold sector as a result of particle currents in the W direction. The total particle current going from the upper sector to the lower sector should be quite balanced by the total particle current going from the lower sector to the upper sector, leaving the magnetization of the upper sector and the lower sector the same as at the beginning ($M_{upper} = M_{lower} = 0$). The resulting stripe-shaped patterns (as shown in Fig.3.10(f)) are long lasting, and the multiple clusters never coalesce into a single cluster, in contrast to what is observed in the equilibrium two-dimensional Ising lattice with Kawasaki dynamics. What we observe in Fig.3.10(f) is a novel non-equilibrium steady state that we call the *modulated state*.

Our extensive Monte Carlo simulations for different combinations of L and T_0 indicate that this type of *modulated state* is very common in our system and that it takes place for a wide range of parameters. For example, when the system size W is kept fixed at a value of 60, the *modulated state* is encountered when L is larger than 14 and T_0 is smaller than T_c. These simulations also show that the relaxation times needed to enter the *modulated state* can be very different, depending on the values of L and T_0. In general, systems with a larger L and a smaller T_0 require larger relaxation time. In Table 3.1 we show the relaxation time scales needed for various systems to reach their corresponding steady states. To obtain these data, we run simulations for up to $t_{run} = 10^7$ Monte Carlo steps, and a snapshot is made every time when the simulation reaches a Monte Carlo step that is ten times larger than the one of the previous snapshot. An ensemble of eight systems were simulated simultaneously and if a certain pattern became consistently stable in every simulation after a certain time, we considered this to be the relaxation time needed to reach the *modulated steady state*.

Table 3.1: The relaxation times needed to reach the *modulated steady states*.

L vs T_0	0.0	0.5	1.0	1.5
20	10^4	10^4	10^4	10^3
30	10^4	10^4	10^4	10^4
40	10^5	10^5	10^5	10^4
50	10^6	10^6	10^6	10^5
60	10^6	10^6	10^6	10^6

3.2.4 Characterization of Non-equilibrium States

The three types of non-equilibrium states that are observed in our systems have been introduced in the previous three subsections. Advanced technique are needed to fully characterize these states. Rather than merely looking at the snapshots of the systems' configurations directly, we performed a spectrum analysis for the characterization of the non-equilibrium states. The major procedures are discussed in the following (see [28] for a short discussion of some of the most important results).

New insights are gained by performing the discrete Fourier transform of the spins $S_{x,y}$ in the upper sector along a horizontal direction:

$$F_y(k) = \frac{1}{2W} \sum_{x=1}^{2W} S_{x,y} e^{ikx} \tag{3.9}$$

In this formula, k is the wave number.

We also calculate the structure factor, which is the square of the modulus of the Fourier transform in Eq.(3.9):

$$S_y(k) = \left| \frac{1}{2W} \sum_{x=1}^{2W} S_{x,y} e^{ikx} \right|^2 \tag{3.10}$$

or,

$$S_y(k) = \frac{1}{4W^2}\left\{[\sum_{x=1}^{2W} S_{x,y} cos(kx)]^2 + [\sum_{x=1}^{2W} S_{x,y} sin(kx)]^2\right\}. \tag{3.11}$$

Since we want to characterize the non-equilibrium states by checking the horizontal pattern in the upper sector, we calculate the line-averaged structure factor where we take the average of Eq.(3.10) over several lines in the middle of the upper sector. For more accurate statistics, we also take time and ensemble averages. Thus, we use the averaged quantity

$$S_{ave}(k) = \frac{3}{L}\sum_{y=4L/3}^{5L/3} \langle S_y(k)\rangle\,, \tag{3.12}$$

to characterize the horizontal patterns and construct the non-equilibrium finite-size phase diagram. Here, $\langle ...\rangle$ means both time and ensemble averages.

It is worth mentioning that the wave number k is directly related to the non-equilibrium steady-state pattern on the two-dimensional lattice. If we define N_s as the number of dark stripes observed in the cold sector, then we have the following relation between N_s and k:

$$N_s = kW/\pi. \tag{3.13}$$

Since the width of the two-dimensional lattice is $2W$, and the smallest stripe width is two lattice sites, the stripe number (N_s) runs from 0 to W. Thus, when k is equal to zero, we have according to Eq.(3.13) that N_s is also equal to zero. This means that we have no periodic pattern in the horizontal direction in the cold sector. Thus $k = 0$ corresponds to the *fully phase separated state*.

However, if k is larger than zero, the corresponding N_s number will be equal to $1, 2, 3, ...$, denoting a surface configuration with N_s full periods in the horizontal direction in the cold sector. Thus, $k = \frac{\pi \times N_s}{W}$ corresponds to the *modulated state* with N_s stripes in the cold sector.

From the relation given in Eq.(3.13), we can also view the structure factor as a function of the stripe number N_s:

$$S_{ave}(N_s) = \frac{3}{L} \sum_{y=4L/3}^{5L/3} \left\langle S_y(\frac{\pi \times N_s}{W}) \right\rangle, \tag{3.14}$$

If the structure factor calculated according to Eq.(3.12) has one pronounced peak at a certain N_s value, it means that the system is in a non-equilibrium steady state, either a *modulated state* with N_s stripe, or in the *fully phase separated state* in which all the particles go to one sector. On the other hand, if the structure factor has no pronounced peak at any N_s value, this means that the system is in the *fully disordered state* where no horizontal periodicity is present in the cold sector. Fig.3.11 and Fig.3.12 illustrate how we use the averaged structure factor $S_{ave}(N_s)$ to characterize the non-equilibrium state of the system. The data in both figures are averages over: (1)1,000,000 Monte Carlo steps after having relaxed the system for 5,000,000 Monte Carlo steps, and (2) 10 independent runs.

In Fig.3.11(a), from the most pronounced peak of each curve, we conclude that the systems with $W = 60, L = 24$ and $T_0 = 0, 0.2, ..., 1.2$ finally relax into *modulated states*. When $T_0 = 0, 0.2$ and 0.4, we expect to observe 9 stripes in the cold sector, whereas when $T_0 = 0.6$ we expect to observe 8 stripes. For $T_0 = 0.8$, the data in Fig.3.11(a) indicate that we may have configurations with either 7 or 8 stripes. Fig.3.11(b) shows that a further increase of T_0 yields curves that peak at even smaller N_s values, meaning that we observe fewer but wider stripes. With $T_0 = 2.0$, we expect to see 4 stripes in the cold sector, whereas with $T_0 = 2.2$, we expect to see zero stripes. (Zero stripes in the cold sector indicates a *fully phase separated state.*) This is because when $T_0 = 2.2$, even though a minor peak exists at $N_s = 3$, another peak at $N_s = 0$ develops abruptly. Finally, when T_0 is increased to 2.4, we find that the peak (in pink) at $N_s = 0$ is decreased and the overall layout of the S_{ave} curve becomes more uniform, which corresponds to less order in the cold sector.

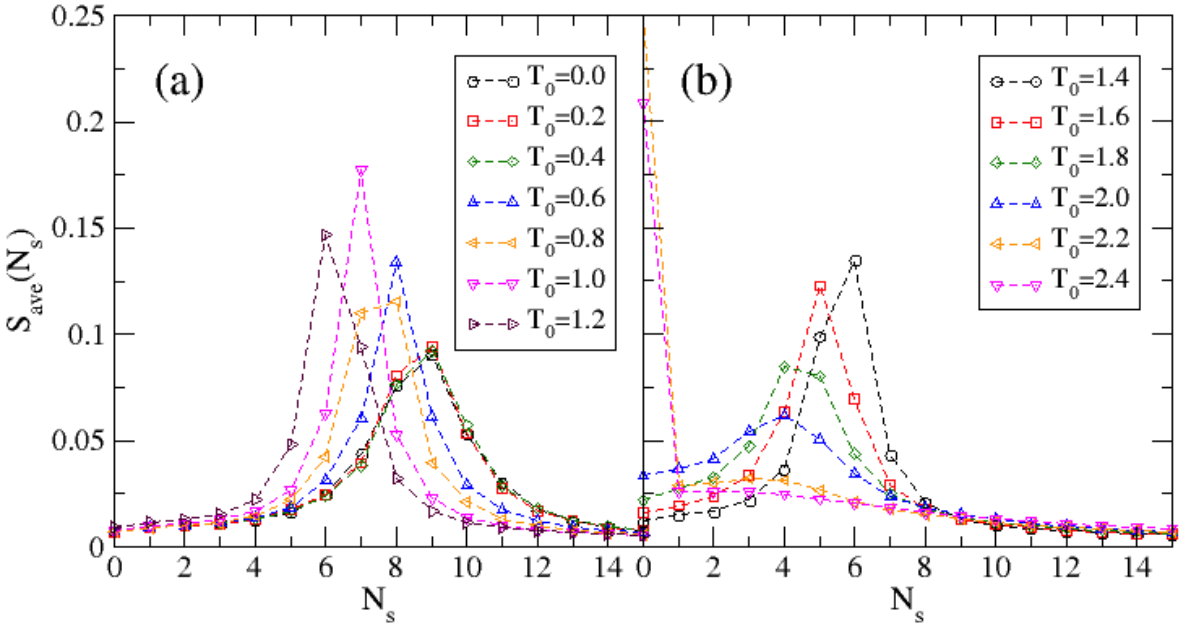

Figure 3.11: Averaged structure factor S_{ave} for the two-temperature two-dimensional Ising lattice gas system with $L = 24$, $W = 60$. The structure factor curves are presented as function of N_s, which is proportional to the wave number k. (a) shows $S_{ave}(N_s)$ for systems with $T_0 = 0.0, 0.2, ..., 1.2$; (b) shows $S_{ave}(N_s)$ for systems with temperature $T_0 = 1.4, 1.6, ..., 2.4$.

Fig.3.12(a)(b) show the structure factor for systems with $W = L = 60$ and $T_0 = 0, 0.2, ..., 2.4$. It is found that the system ends up in a *modulated states* for all temperatures T_0 smaller than 2.2. When $T_0 = 2.4$, no apparent peak shows up in the structure factor (see the pink curve in Fig.3.12(b)). The appearance of a peak at $S_{ave}(N_s) = 1$ means that at $T_0 = 2.2$ the system is in a *modulated state* with a single stripe in the cold sector, similar to what one observes for an equilibrium system at temperatures below T_c. For $T_0 = 2.4$, the system is in a *fully disordered state*.

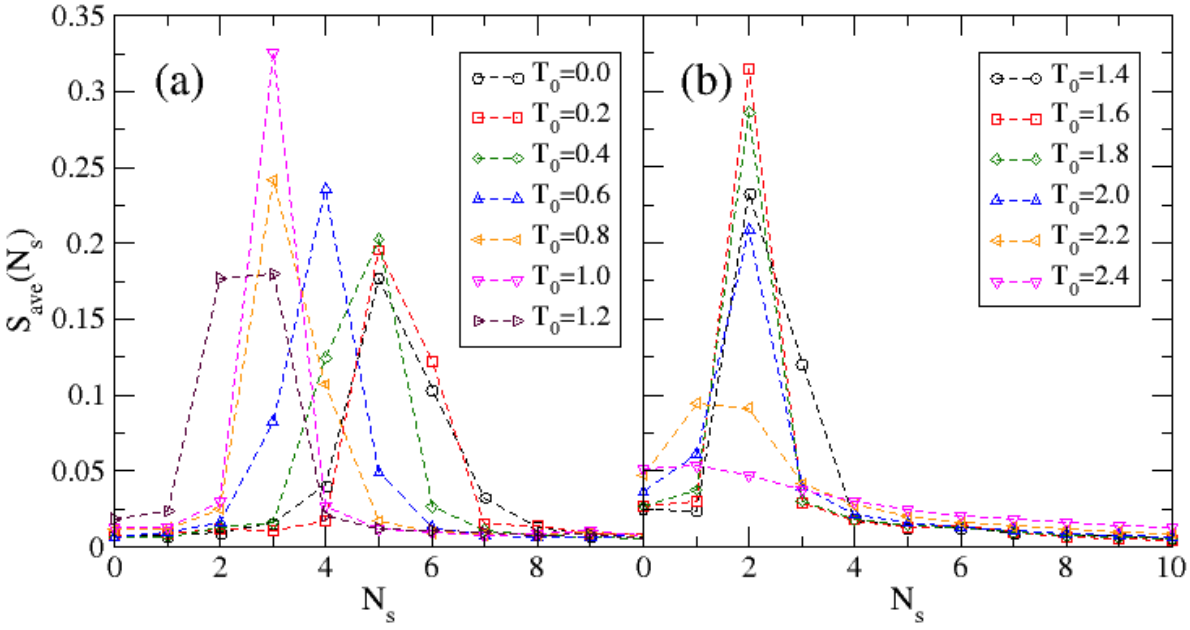

Figure 3.12: Averaged structure factor S_{ave} for the two-temperature two-dimensional Ising lattice gas system with $L = W = 60$. The structure factor curves are presented as function of N_s, which is proportional to the wave number k. (a) shows $S_{ave}(N_s)$ for systems with $T_0 = 0.0, 0.2, ..., 1.2$; (b) shows $S_{ave}(N_s)$ for systems with temperature $T_0 = 1.4, 1.6, ..., 2.4$.

3.2.5 The Finite-size Phase Diagram

As illustrated in the last subsection, we can use spectrum analysis to systematically characterize the non-equilibrium states of the system as a function of system sizes and temperature T_0. Accordingly, we can map out a finite-size phase diagram of the non-equilibrium states as a function of system size ratio L/W and the temperature ratio T_0/T_c, keeping W constant at $W = 60$, see Fig.3.13.

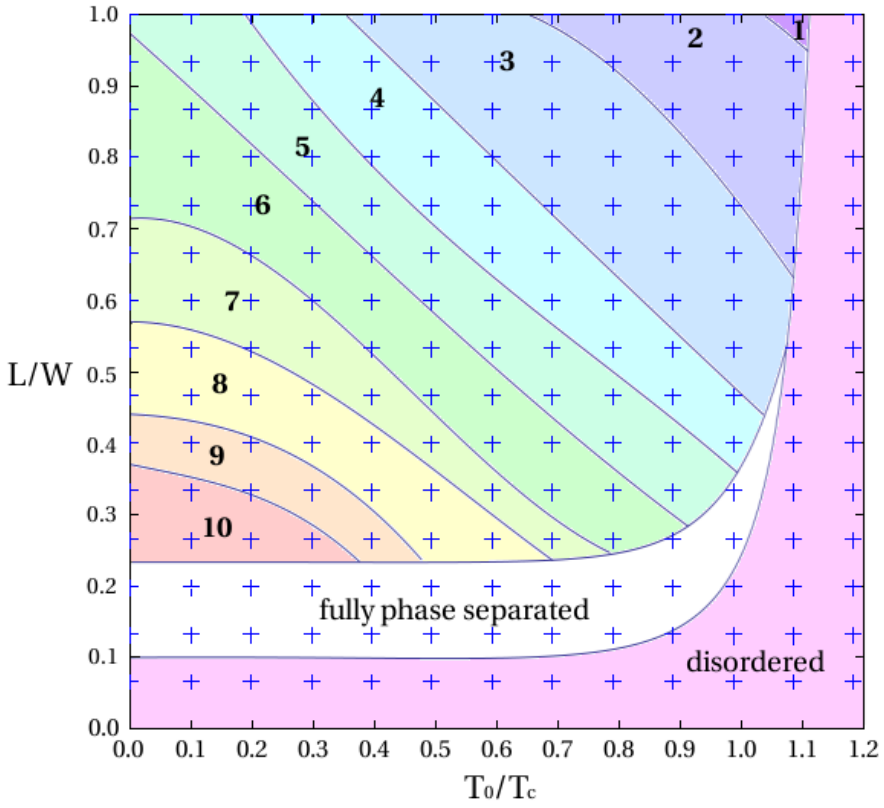

Figure 3.13: (Figure from [28], reprinted with permission from IOP Publishing.) Finite-size phase diagram of the two-temperature two-dimensional Ising lattice gas system with $2W = 120$, as a function of T_0/T_c and L/W. The fully disordered state, the fully phase separated state and the modulated states are readily identified from this finite-size phase diagram. The regions labeled indicate modulated states with certain number of stripes that are formed in the cold (T_0) sector. The crosses indicate the temperatures and system sizes at which the numerical simulations were done. The lines separating the different phases result from splines through the midpoints between crosses that yield different phases.

To obtain this finite-size phase diagram, we ran simulations for systems at temperatures $T_0 = 0.0, 0.2, ..., 2.4$ and sizes $L = 4, 8, 12, ..., 60$. The non-equilibrium states are characterized using the method illustrated in the last subsection. The parameter values used for the simulations are marked by crosses in Fig.3.13.

What can be immediately found in this finite-size phase diagram are the three regions which represent the three types of non-equilibrium states. The fully disordered state is located in the region where the system size is small or the temperature is large (see the pink area in Fig.3.13). The fully phase separated state is located in the region where both the system size and the temperature are relatively small (see the white area in Fig.3.13). The modulated state is located in the region where the system size is relatively large while the temperature is relatively small (see the area that is labeled by numbers in Fig.3.13). The region of the modulated state is composed of many subregions characterized by different numbers of stripes in the cold sector.

The finite-size phase diagram in Fig.3.13 is obtained by simulations with $W = 60$. One question for this finite-size phase diagram is if the modulated states survive when the W increase to infinity, while keeping the aspect ratio L/W the same. Data from simulations of $W = 30$ and $W = 90$ systems along with data for the $W = 60$ system show that: with $T_0 = 0.4, L/W = 1$, the stripe number increase from 3 to 5 to 6, when W increase from 30 to 60 to 90. This means the finite-size phase diagram in Fig.3.13 changes with the system size W. The theory for finding the true phase diagram with infinite system size is still absent.

3.2.6 Further Analysis of the Non-equilibrium States

As discussed in the first section of this chapter, it was found in [27] that long-lasting vortices are spreading over the whole system if pinned boundary conditions are applied

to the two-dimensional two-temperature lattice model. These vortices characterize the non-equilibrium steady state in that situation. In that paper the authors used the average stream function $\langle\psi(x,y)\rangle$ and the average vorticity $\langle w(x,y)\rangle$ to describe this non-equilibrium state quantitatively, see Fig.3.3. However, when periodic boundary conditions are applied in both x and y directions, the cluster of particles in the cold sector can move in the horizontal direction. Accordingly, the vortices that show up at the corners of the bulk cluster can move along the interfaces freely. Consequently, the averaged quantities $\langle\psi(x,y)\rangle$ and $\langle w(x,y)\rangle$ are trivially zero when using periodic boundary conditions.

We solved this problem by introducing (we here go back to the language of magnetic spin systems) the *spin-vorticity correlation function* $\langle S_{x',y'}w(x,y)\rangle$. Here $w(x,y)$ is the vorticity related to the plaquette centered at $(x+1/2, y+1/2)$ and $S_{x',y'}$ is the occupancy state for a site that is located at (x',y'). In our research, the occupancy state is usually obtained from a site in the cold sector where $L < y < 2L$. In the following, we want to demonstrate how the spin-vorticity correlations can be used to characterize the non-equilibrium modulated states.

In the Monte Carlo simulations, we measure two quantities: $\left\langle S_{W/2,3L/2}w(W,L)\right\rangle$ and $\left\langle S_{3W/2,3L/2}w(W,L)\right\rangle$. The first quantity correlates the occupancy state at $(W/2, 3L/2)$ with the vorticity at $(W+1/2, L+1/2)$, the second quantity correlates the occupancy state at $(3W/2, 3L/2)$ with the vorticity at $(W+1/2, L+1/2)$. Now, let us focus on $\left\langle S_{W/2,3L/2}w(W,L)\right\rangle$. From the sketch in Fig.3.14 we can see that the modulated state with $N_s = 1$ should give $\left\langle S_{W/2,3L/2}w(W,L)\right\rangle > 0$, the modulated state with $N_s = 3$ should yield $\left\langle S_{W/2,3L/2}w(W,L)\right\rangle < 0$, whereas the modulated states with $N_s = 2, 4$ should give $\left\langle S_{W/2,3L/2}w(W,L)\right\rangle = 0$. If N_s extends to larger numbers, it is not hard to prove that all systems with modulated states with $N_s = 4n+1$ $(n = 0, 1, 2, 3...)$ should result in positive values of $\left\langle S_{W/2,3L/2}w(W,L)\right\rangle$, whereas all systems with modulated states with $N_s = 4m-1$ $(m = 1, 2, 3, 4...)$ should give negative values of $\left\langle S_{W/2,3L/2}w(W,L)\right\rangle$.

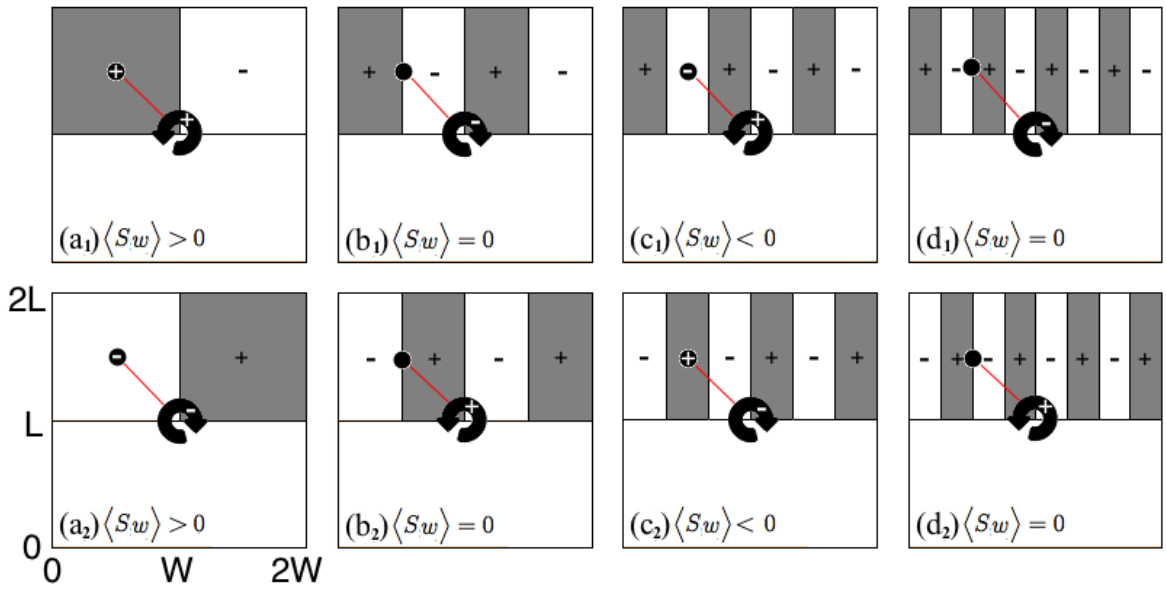

Figure 3.14: Schematic pictures that show how we quantify the non-equilibrium steady states in our system by using the quantity $\langle S_{W/2,3L/2}, w(W,L)\rangle$. (a_1) and (a_2) illustrate that the modulated state with one stripe in the cold sector yields a positive value of $\langle S_{W/2,3L/2}, w(W,L)\rangle$; (b_1) and (b_2) illustrate that the modulated state with two stripes in the cold sector yields a negative value of $\langle S_{W/2,3L/2}, w(W,L)\rangle$; (c_1) and (c_2) illustrate that the modulated state with three stripes in the cold sector yields a zero value of $\langle S_{W/2,3L/2}, w(W,L)\rangle$; (d_1) and (d_2) illustrate that the modulated state with four stripes in the cold sector yields a zero value of $\langle S_{W/2,3L/2}, w(W,L)\rangle$.

From Fig. 3.14, we see how the modulated states can be related to the different values of $\left\langle S_{3W/2,3L/2} w(W,L)\right\rangle$. It is not hard to find from the same figure that, due to symmetry, the occupancy state at (3W/2,3L/2) is always taking the sign opposite to the sign of the occupancy state at (W/2,3L/2). Therefore, the value of $\left\langle S_{3W/2,3L/2} w(W,L)\right\rangle$ should always have a similar magnitude but different sign compared to the value of $\left\langle S_{W/2,3L/2} w(W,L)\right\rangle$. From this, we can readily prove that all systems with modulated states with $N_s = 4n+1$ $(n = 0,1,2,3...)$ give negative values of $\left\langle S_{W/2,3L/2} w(W,L)\right\rangle$, all systems with modulated states with $N_s = 4m-1$ $(m = 1,2,3,4...)$ give positive values of $\left\langle S_{W/2,3L/2} w(W,L)\right\rangle$,

whereas all systems with $N_s = 2l$ $(l = 0, 1, 2, 3, ...)$ give $\left\langle S_{W/2,3L/2} w(W, L) \right\rangle = 0$.

The data for the spin-vorticity correlation $\left\langle S_{W/2,3L/2} w(W, L) \right\rangle$ obtained in our simulations for $W = L = 60$ are shown in Fig.3.15. If the temperature is relatively low (such as $T_0 = 0.088T_c$ or $T_0 = 0.176T_c$), $\left\langle S_{W/2,3L/2} w(W, L) \right\rangle$ is positive (0.0008 or 0.0012). With the aforementioned relation between the modulated states and the sign of the spin-vorticity correlation, we expect to have modulated states with $N_s = 1, 5, 9...$ in order to produce such $\langle Sw \rangle$ values. When T_0 is increased to $0.264T_c$, we find that $\left\langle S_{W/2,3L/2} w(W, L) \right\rangle$ is zero within our numerical precision. We then should have a modulated state with an even number of stripes. When T_0 is further increased to larger values, such as $0.353T_c, 0.441T_c, 0.529T_c$ and $0.617T_c$, we measure negative values for $\left\langle S_{W/2,3L/2} w(W, L) \right\rangle$. This reflects the occurrence of the modulated states with $N_s = 3, 7, 11....$ For even higher temperatures, $\langle Sw \rangle$ approaches zero.

Let us now compare Fig.3.15 with Fig.3.13. For the first two data points in Fig.3.15, where $T_0 = 0.088T_c$ and $0.176T_c$, we have in Fig.3.13 that these two temperatures correspond to modulated states with $N_s = 5$. For the third data point, we find that the steady state at that the temperature $(0.264T_c)$ corresponds to a modulated state with $N_s = 4$. For the data with $T_0 = 0.353T_c, 0.441T_c, 0.529T_c$ and $0.617T_c$, we find from Fig.3.13 that the system should be in the modulate states with $N_s = 3$. Finally, for the last three data points in Fig.3.15, we have the modulate state with $N_s = 2$. Therefore, all the data shown in Fig.3.15 are consistent with the finite-size phase diagram in Fig.3.13.

Thus, even though it is more difficult to derive the exact number of stripes, the spin-vorticity correlation correctly captures features of the stripe patterns. Most importantly, non-vanishing values of the spin-vorticity correlation proves that the appearance of the striped pattern and the appearance of the vortices (at the corners of the stripes) are closely related.

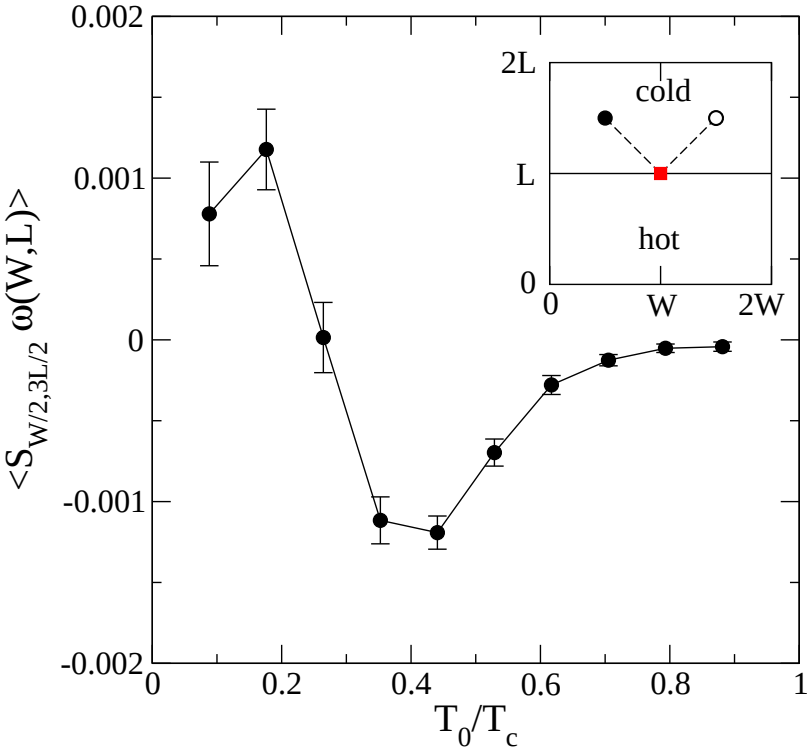

Figure 3.15: (Figure from [28], reprinted with permission from IOP Publishing.) Temperature dependence of the spin-vorticity correlation $\langle S_{W/2,3L/2}, w(W,L)\rangle$ that relates the vorticity around a plaquette in the middle of the interface separating the hot and cold sectors to the spin $S_{W/2,3L/2}$ located inside the cold sector. The system contains $2W \times 2L$ sites, with $W = L = 60$. The inset shows the positions of the plaquette (square) and of the spin $S_{W/2,3L/2}$ (full circle) in the sample. The correlation $\langle S_{3W/2,3L/2}, w(W,L)\rangle$ with the spin $S_{3W/2,3L/2}$, shown by the open circle in the inset, only differs from $\langle S_{W/2,3L/2}\, w(W,L)\rangle$ by the sign.

Thus, even though it is more difficult to derive the exact number of stripes, the spin-vorticity correlation correctly captures features of the stripe patterns. Most importantly, non-vanishing values of the spin-vorticity correlation proves that the appearance of the striped pattern and the appearance of the vortices (at the corners of the stripes) are closely related.

In conclusion, in addition to the structure factor, we can also use the spin-vorticity correlation $\langle S_{x',y'} w(x,y) \rangle$ to characterize modulated states. The prediction of the possible modulated states from this quantity is consistent with the results given by the structure factor.

3.3 Phase Transition between Non-equilibrium States

We can obtain interesting information about the non-equilibrium phase transitions occurring in our system from the finite-size phase diagram shown in Fig.3.13. For example, when the system size L is very small ($L \leq 6$), the system will stay in the *fully disordered state* without any phase transition for all temperatures $T_0 < T_c$. When the system size L is relatively small ($6 < L \leq 12$), the two-temperature system may transit from the *fully phase separated state* to the *fully disordered state* when increasing T_0. For larger systems ($L > 12$), transitions between different *modulated states* take place when changing the temperature T_0. Finally, for a larger value of T_0 a phase transition to the *fully phase separated state*, and/or the *fully disordered state* takes place.

3.3.1 Phase Transition between Different Modulated States

From the plots of the structure factors (see Fig.3.11 and Fig.3.12), we know that in most cases the *modulated state* is characterized by a structure factor that has a peak at a

specific wave number. Examples are readily seen in Fig.3.12(a), when the temperature T_0 is equal to 0.0, 0.2, 0.4, 0.6, or 0.8.

However, there are also some cases where the structure factor is large for more than one value of N_s, as is seen for example for the $T_0 = 1.2$ case in Fig.3.12(a) or the $T_0 = 2.2$ and 2.4 cases in Fig.3.12(b). In order to better understand this behavior, we analyze the structure factor as a function of the continuous wave number k. What we find in Fig.3.16

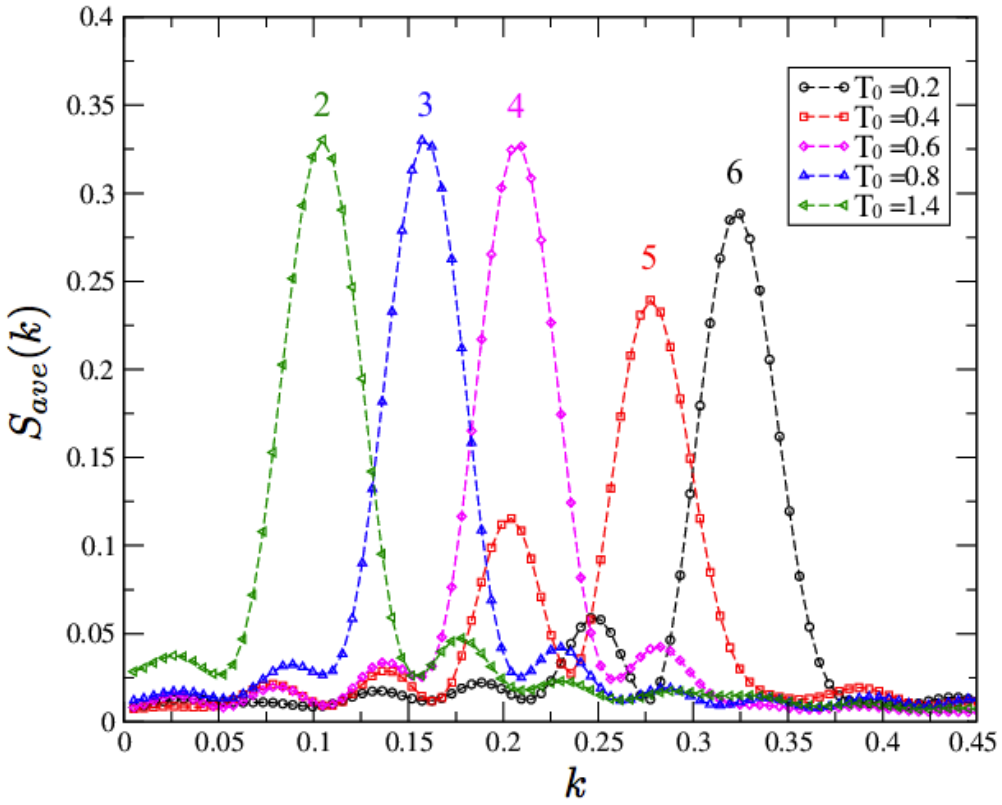

Figure 3.16: Averaged structure factor $S_{ave}(k)$ for a system with $W = L = 60$, at various temperatures T_0 of the cold sector [28]. Each data point is an average of 10 simulations. In each simulation we averaged over 10^7 MCSs after relaxing the system for 5×10^6 MCSs. The label on the maxima corresponds to the number of stripes.

is that the structure factor of the system (for a fixed size of $W = L = 60$) usually exhibits one major maximum for each temperature (see the curves for $T_0 = 0.2, 0.6, 0.8$ and 1.4

systems in Fig.3.16). There is the trend that the maximum shifts to smaller k values with the increase of the system temperature T_0. Using the language of stripe numbers, it means that the larger T_0, the less stripes will be observed in the cold sector of the two-temperature lattice gas system.

In some cases the structure factor as a function of k shows two pronounced maxima (see the curve for $T_0 = 0.4$ in Fig.3.16). The presence of two pronounced maxima can be interpreted as the coexistence of two non-equilibrium modulated states with different numbers of stripes (4 and 5 in our example). The coexistence of the two states indicates that the phase transition between the two modulated states is discontinuous (first order).

The symmetry reason behind the discontinuous character of the transition is the periodicity in the translation in the direction parallel to the interface (the stripe pattern with n stripes is invariant when shifting the whole structure by W/n lattice sites).

3.3.2 Phase Transition between the Modulated State and the Fully Phase Separated State

To better understand the phase transition behavior when the system transits between a modulated state and the fully phase separated state, we show the $S_{ave}(k)$ data for systems with $W = 60, L = 20$, and $T_0 = 1.8, 2.0, 2.2$ in Fig.3.17.

In this figure, when the system temperature is as low as $T_0 = 1.8$, we see only one prominent maximum located at $N_s = 5$ (see the black curve). When T_0 is raised to 2.0, no maximum is found for either $N_s = 5, 4$ or 3. Instead, we observe a pronounced maximum located at $N_s = 0$, with a $S_{ave}(0)$ value being around 0.2 (see the red curve). If we increase T_0 to 2.2, the maximum further increases (see the blue curve).

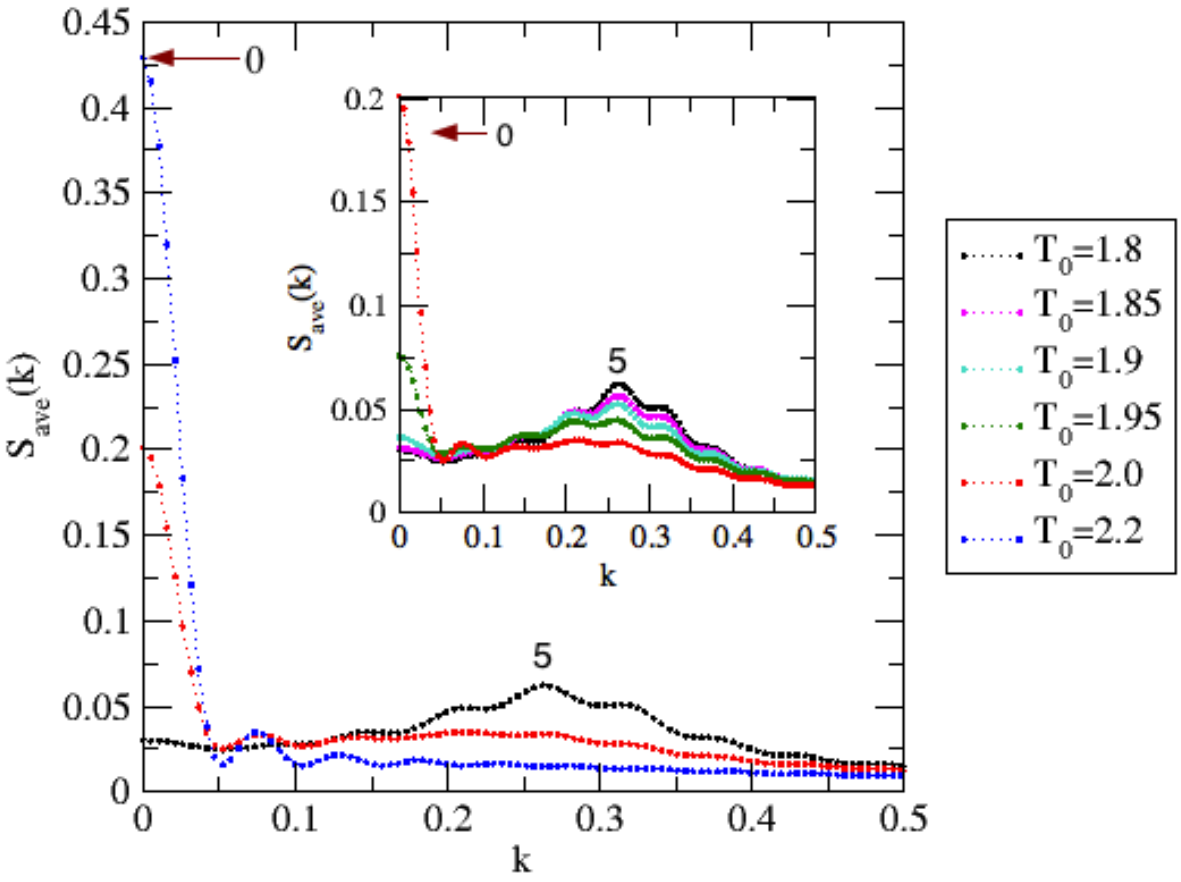

Figure 3.17: Averaged structure factor $S_{ave}(k)$ for a system with $W = 60, L = 20$, with $T_0 = 1.8$, 2.0 and 2.2. The inset shows the $S_{ave}(k)$ data for the same system at $T_0 = 1.8$, 1.85, 1.9, 1.95, and 2.0. Each data point is an average of 16 simulations and for each simulation 10^7 MCSs were done after relaxing the system for 5×10^6 MCSs. The label on the maxima corresponds to the number of stripes.

More detailed information can be obtained from the $S_{ave}(k)$ data at additional temperatures between $T_0 = 1.8$ and $T_0 = 2.0$, as shown in the insect of Fig.3.17. Comparing the data for systems with $T_0 = 1.8, 1.85, 1.9, 1.95$ and 2.0, it seems that the dominant maximum shifts from $N_s = 5$ to $N_s = 0$ when T_0 increases from 1.9 to 1.95.

To sum up, our simulations indicate that the system transits directly from a finite k to the $k = 0$ state, without going through other modulated states with medium k values. As a result the phase transition between the modulated state and the fully phase separated state is discontinuous (first order).

3.3.3 Phase Transition between the Fully Phase Separated State and the Fully Disordered State

In order to study the phase transition when the system transits between the fully phase separated state and the fully disordered state, we calculate through Monte Carlo simulations $S_{ave}(k)$ for systems with $W = 60, L = 20$, and $T_0 = 2.2, 2.4, 2.6, 2.8$. The $S_{ave}(k)$ data for different temperatures are shown in Fig.3.18.

In this figure, we first examine $S_{ave}(k)$ for a system with its T_0(=2.2) very close to the $T_c(\approx 2.269)$ of the classical two-dimensional Ising model (see the black curve). We observe a large maximum at the origin ($S_{ave}(0)$ ≈0.43) with minor maximum located at other k values. The first minor maxima is located at $k \approx 0.0733$ ($N_s \approx 1.4$) with a value of $S_{ave}(k) \approx 0.0346$, the second minor maximum is located at $k \approx 0.1309$ ($N_s \approx 2.5$) with a value of $S_{ave}(k) \approx 0.0216$, etc. One notices that the minor peaks are not located at integral N_s values. To explain this phenomenon we studied in detail the configurations showing up in the simulations. We find that when the system is in the fully phase separated state, there is a small but non-zero probability that all the particles collectively flow from one temperature sector to the other. This particle flow contributes to $S_{ave}(k)$

in a very complicated way and shows up in the form of these minor maxima. When the temperature T_0 is raised to 2.4 (see the red curve), the $S_{ave}(k)$ curve still peaks at $k = 0$, but with a much smaller value ($S_{ave}(0) \approx 0.1624$). When $k > 0$, the $S_{ave}(k)$ values become slightly larger and more uniform compared to the $T_0 = 2.2$ counterpart.

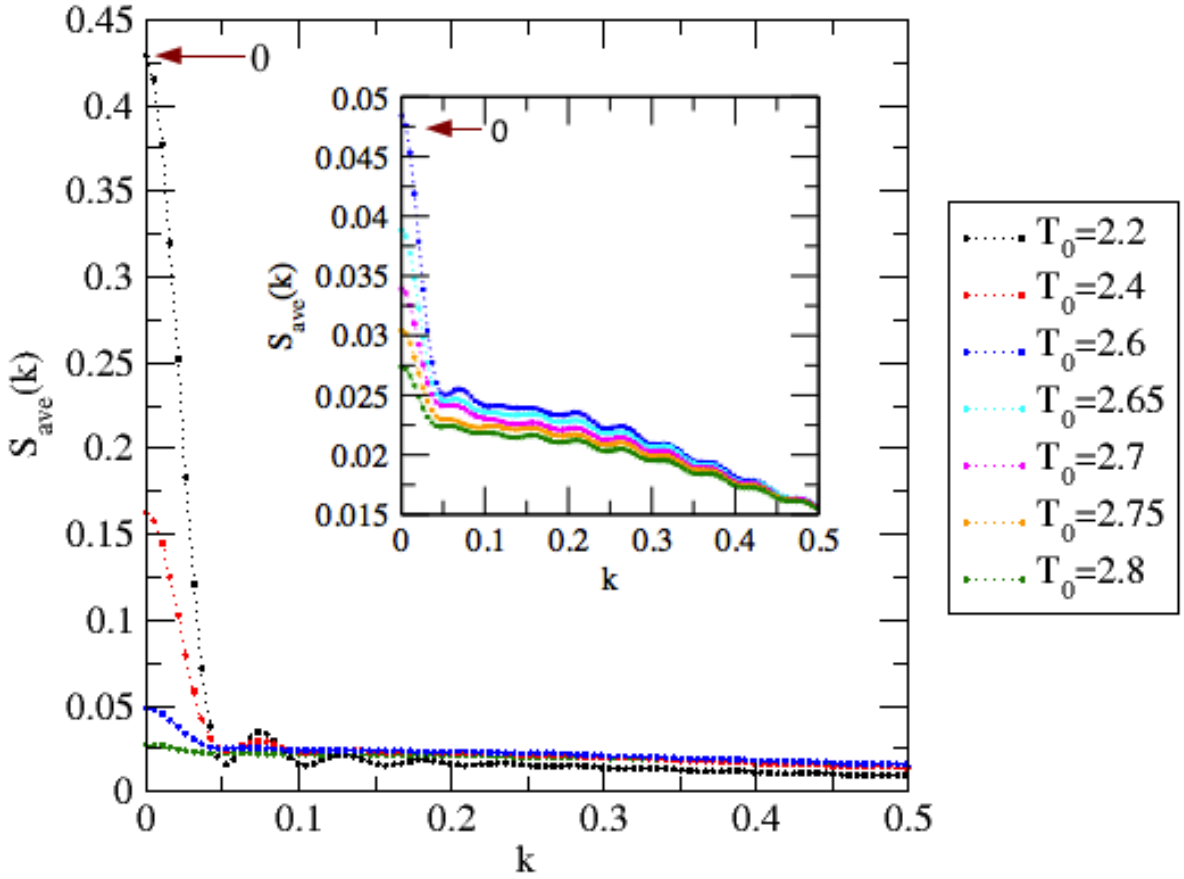

Figure 3.18: Averaged structure factor $S_{ave}(k)$ for a system with $W = 60, L = 20$, and the cold sector temperature $T_0 = 2.2$, 2.4, 2.6 and 2.8. The inset shows the $S_{ave}(k)$ data for the same system at $T_0 = 2.6$, 2.65, 2.7, 2.75 and 2.8. Each data point is an average of 16 simulations and for each simulation the data were averaged over 10^7 MCSs after relaxing the system for 5×10^6 MCSs.

Especially, the first minor maximum is taking a smaller value. When T_0 reaches 2.6, as shown in the blue curve, $S_{ave}(0)$ drops to a small number around 0.0484. For $k > 0$, no minor maximum can be observed and the structure factor decreases almost linearly once k becomes larger than 0.05. Finally, for $T_0 = 2.8$ (see dark green curve), the curve is very uniform and no obvious maximum can be distinguished from the rest. Thus, at $T_0 = 2.8$ the system is in the fully disordered state.

To check what happens exactly when the temperature T_0 is raised from 2.6 to 2.8, we ran simulations for $T_0 = 2.65, 2.7$ and 2.75. These extra data, along with the $T_0 = 2.6$ and 2.8 data, are shown in the inset of Fig.3.18. When T_0 increases from 2.6 to 2.8, the $S_{ave}(k)$ values decrease for all k's. The only difference is that the rate of decrease (as a function of T_0) is much larger for the wave vectors that are close to $k = 0$. This makes the $S_{ave}(k)$ profile more and more uniform.

3.3.4 Phase Transition between the Modulated State and the Fully Disordered State

Fig.3.19 shows the $S_{ave}(k)$ data for systems with $L = 52, W = 60$ and T_0 =1.6 to 2.4. It is apparent from the figure that the system's major maximum discontinuously jumps from $N_s = 3$ to $N_s = 2$ when T_0 increase from 1.6 to 1.8, whereas it stays at $N_s = 2$ when T_0 is further increased to 2.0. However, for the same system no major maximum is observed from the $S_{ave}(k)$ data at $T = 2.2$ (see the dark green curve). Instead, we can see two minor maxima, one located at ($N_s = 1$), the other located at ($N_s = 2$). In this case, the k (N_s) range in which $S_{ave} > 0.05$ starts from 0.0209 (0.4) and ends at 0.1414 (2.7). This broad range of very similar k (N_s) values is a demonstration that the system is no longer dominated by a modulated state, but that a certain degree of disorder exists in the cold sector of the system. At $T_0 = 2.4$, the $S_{ave}(k)$ curve is further flattened and its value is very similar for all the k (N_s) values. It follows that the cold sector of the system

is now in complete disorder. This continuous change indicates that the phase transition between a modulated state and the fully disordered state is a continuous transition.

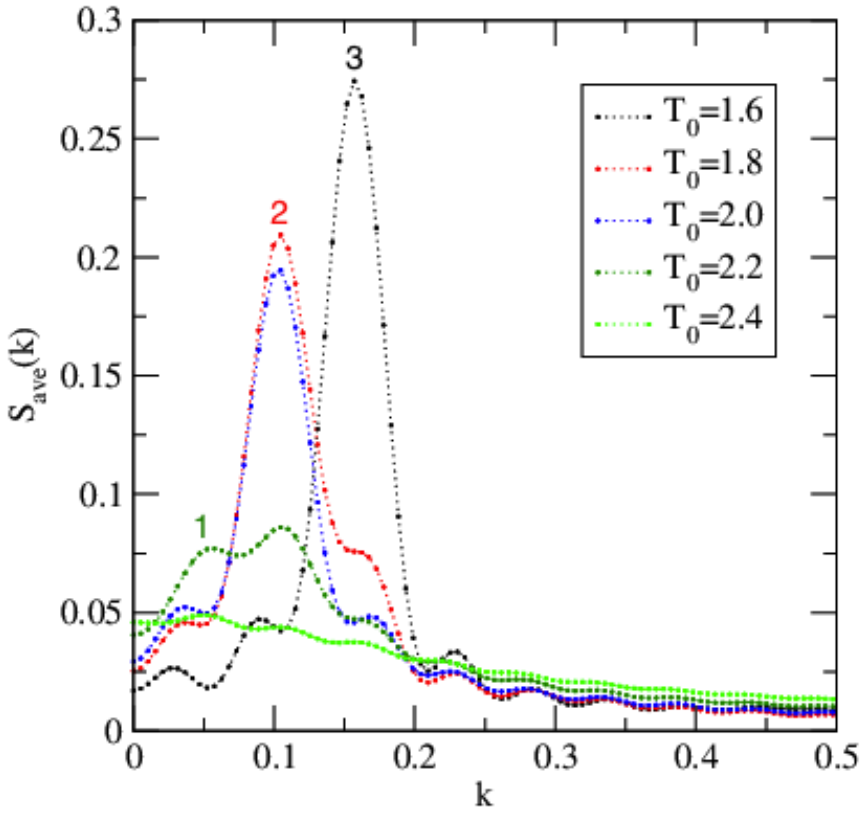

Figure 3.19: Averaged structure factor $S_{ave}(k)$ for a system with $W = 60, L = 52$, at various temperatures T_0 of the cold sector. Each data point is an average of 16 simulations and for each simulation 10^7 MCSs were performed after relaxing the system for 5×10^6 MCSs. The label on the maxima corresponds to the number of stripes.

3.4 Summary

In this chapter, I introduced a two-temperature two-dimensional lattice gas model. In this model, free hopping is enforced on the interfaces of the two sectors (with different

temperatures), which leads to breaking of detailed balance and energy influx at the interfaces. From extensive MCMC (Markov Chain Monte Carlo) simulations of systems with lengths of $2L$, we observed three different non-equilibrium states for different system parameters T_0 (temperature of the cold sector) and L (the distance from one interface to another). These non-equilibrium states include a *fully disordered state*, a *fully phase separated state*, and a *modulated state*. The modulated state can be further subcategorized into non-equilibrium states according to the pattern (number of stripes) appearing in the cold sector of the systems. A finite-size phase diagram of the system is constructed by calculating the structure factors during the MCMC simulations.

In addition, we calculated the spin-vorticity correlations to characterize the modulated states, which corresponds well with the information given by the finite-size phase diagram (where the phases are characterized by structure factors). At last, we examined the phase transitions between different non-equilibrium states by varying the cold sector temperatures of the lattice gas systems. Our observation shows that the phase transition between a modulated state and any other state (another modulated state, a fully phase separated state, or a fully disordered state) is discontinuous in k (the wave number).

Chapter 4

Magnetic Friction between Surfaces

Magnetic systems, whose surfaces are coupled by boundary spins, experience magnetic friction if one system is moving with a relative velocity along the coupled surface. In this Chapter, we first investigate the phase transition behavior of the free surfaces of the Potts systems [29–33]. The new results about the surface critical exponents for two-dimensional Potts systems shed light on how the free surfaces should behave when the surface of a Potts system is not in contact with other Potts systems. Then, we turn to the study of three-dimensional Potts systems in which both interfacial couplings and relative movement between two contacting surfaces exist. These new systems are Potts systems with magnetic friction. To study the behavior of contacting surfaces, we focus on systems with two kinds of geometries. The first kind consists of two identical Potts blocks in which the bottom surface of the upper block is coupled to and moving along the top surface of the lower block. The second kind of geometry consists of a wedge-shaped Potts lattice on the top and a Potts block at the bottom, with the tip of the wedge sliding along the top surface of the lower block. Since the first kind of system involves full contact between the two surfaces of the coupled lattices and the second kind involves only partial contact, we expect to see the emergence of different phenomena as a result of magnetic friction.

4.1 Phase Transition in a Potts System with a Free Surface

Before studying the magnetic behavior of contacting surfaces with magnetic friction, we should first understand the magnetic behavior of the free surfaces. In the following, we first introduce the concept of free surfaces of Potts systems in different dimensions and then discuss critical properties of the free surfaces in certain scenarios. Some of the results obtained for Potts systems with free surfaces have been summarized in the publication [33].

4.1.1 The Free Surfaces of Potts Systems

In general, a free surface of a D dimensional Potts lattice is a $D-1$ dimensional surface layer, where every site has two bonds to neighboring sites in each of the first $D-1$ dimensions and only one bond in the D^{th} dimension.

The concept of a free surface can be illustrated by the schematic pictures in Fig.4.1. For example, in Fig.4.1(a), in which we have a Potts system with $D = 1$, each of the lattice sites inside (the bulk sites shown in brown) has two bonds in the only given dimension. Yet, the site on the top (the boundary site shown in dark green) has only one bond, which couples it to a bulk site. Similarly, in Fig.4.1(b), in which we have a Potts system with $D = 2$, we see that all the bulk sites have two bonds in both dimensions, while the sites on the surface have two bonds in the first dimension and only one bond in the other.

The missing bond in the D^{th} dimension of each lattice site makes the magnetic behavior of the surface different from that of the bulk inside. In the following subsections, we will present both previously established results as well as our new results on the behavior of

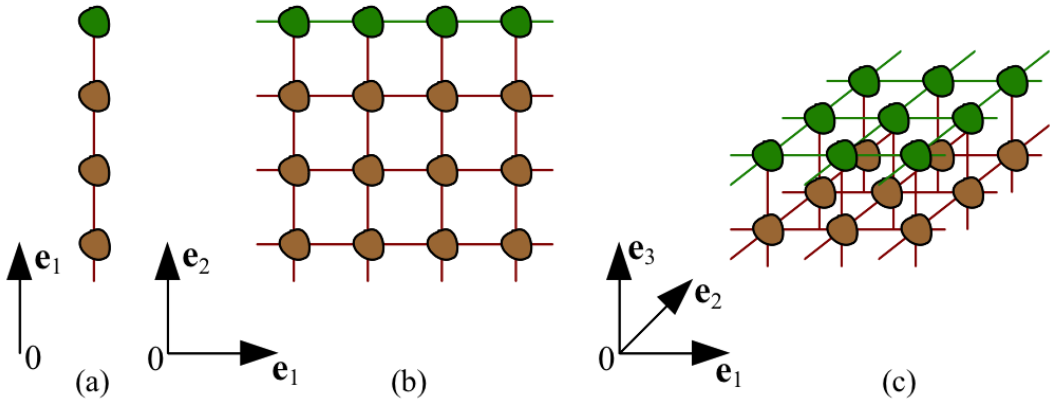

Figure 4.1: Illustrations of free surfaces for Potts systems in different dimensions. In (a), the zero-dimensional dark green lattice site is the free surface of the one-dimensional Potts chain. In (b), the one-dimensional dark green chain of lattice sites is the free surface of the two-dimensional Potts bulk. In (c), the two-dimensional dark green layer of lattice sites is the free surface of the three-dimensional Potts bulk.

free surfaces at phase transitions. Our focus will be on the surface critical exponents at discontinuous bulk transitions of two dimensional Potts systems (as shown in Fig.4.1(b)). This two-dimensional system is characterized by the following hamiltonian:

$$H = -J_b \sum_{bulk} \delta(s_{x,y} - s_{x',y'}) - J_s \sum_{surface} \delta(s_{x,y_s} - s_{x',y_s}) \tag{4.1}$$

Here, the Kronecker delta in the first summation term gives the energy produced by two neighboring spins where at least one of them does not belong to the surface, whereas the Kronecker delta in the second summation term gives the energy produced by two neighboring spins that are both located at the surface.

4.1.2 Background: Surface Phase Transition at a Continuous Phase Transition

The free surfaces of spin systems are well known to change the critical properties locally [29].

Fig.4.2 shows the magnetizations of each layer of a three-dimensional Ising system with surfaces when the temperature is close to the equilibrium critical temperature of the bulk.

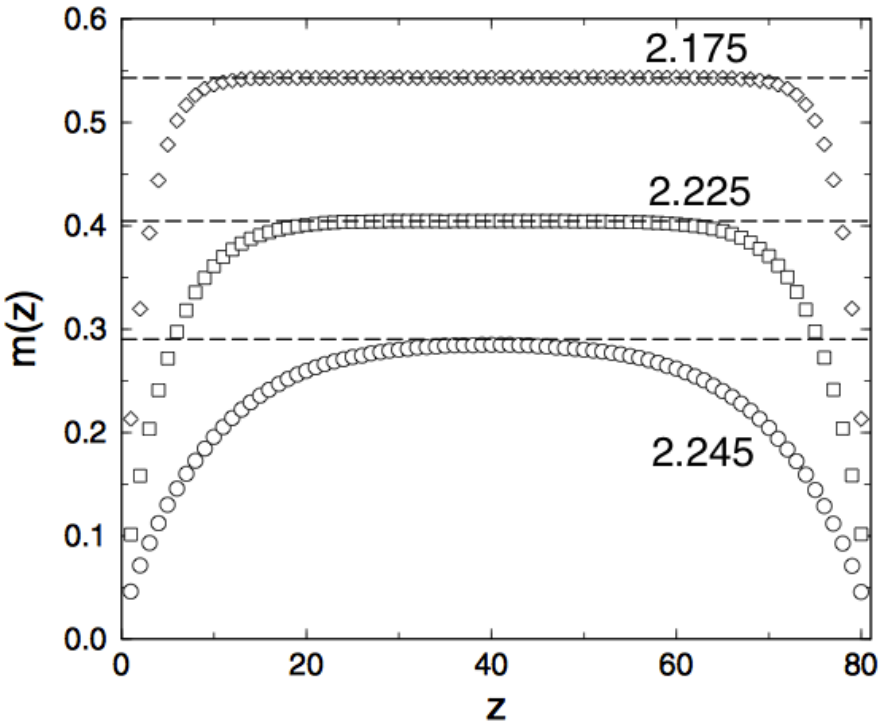

Figure 4.2: (Figure from [30], reprinted with permission from IOP Publishing.) Order parameter profiles $m(z)$ of a three-dimensional Ising film with 80 layers at three different temperatures k_BT/J_b (all below the bulk critical temperature). The dashed lines denote the bulk values.

It is not hard to find from Fig.4.2 that the magnetizations of the surface layers with $z = 1$ and $z = 80$ are much smaller than that of the layers deep in the bulk (such as the layers

at $z = 40$). For example, with an increase of temperature from 2.175 to 2.245, the surface magnetizations decrease from 0.22(1) to 0.04(1), whereas the magnetizations at $z = 40$ decrease from 0.54(1) to 0.29(1).

Fig.4.3 presents the surface phase diagram of the three-dimensional Ising system, where the differences between the transitions at the free surface and the transitions in the bulk are readily seen.

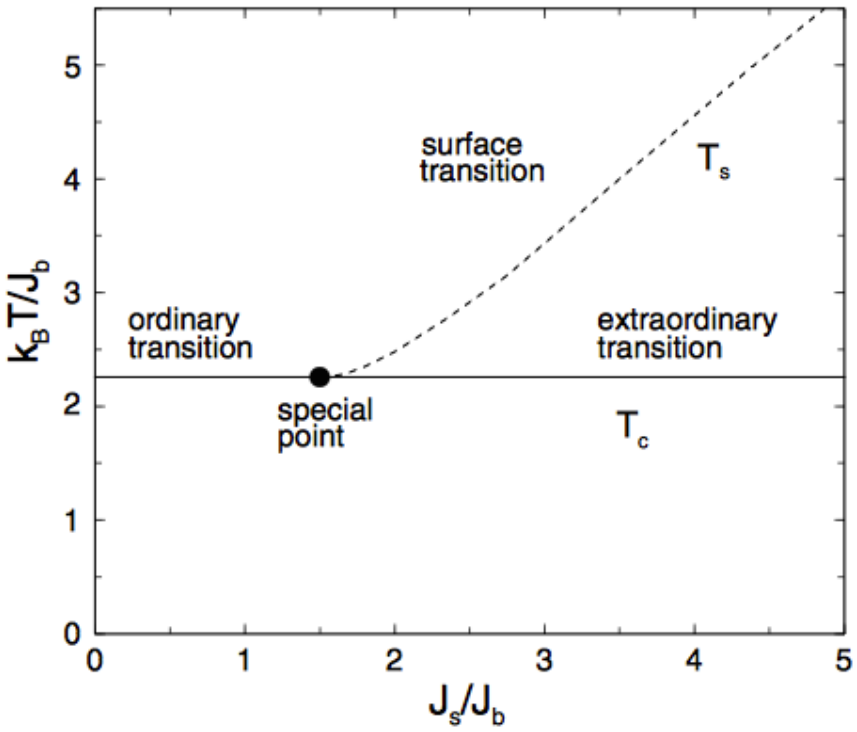

Figure 4.3: (Figure from [30], reprinted with permission from IOP Publishing.) Surface phase diagram of the semi-infinite three-dimensional Ising model. J_s is the coupling strength on the surface, and J_b is the coupling strength in the bulk.

As shown in Fig.4.3, if the value of the ratio $r = J_s/J_b$ is smaller than value $r_{sp} \approx 1.50$ at the special point, the transition temperature of the surface ($T_s \approx$2.267) is the same as the transition temperature of the bulk ($T_c \approx$2.267). However, if the value of r exceeds that of the special point (or coupling strength of the surface becomes more than r_{sp} times

bigger than that of the bulk), the transition temperature of the surface (T_s) starts to deviate from the transition temperature of the bulk ($T_c \approx 2.267$). In this case, the bulk experiences an extraordinary phase transition in the presence of ordered surfaces. At the special point where r is equal to r_{sp}, the surface critical properties deviate from those at the ordinary transition and from those at the extraordinary transition.

4.1.3 Surface Phase Transition at Discontinuous Bulk Transitions

To study the surface phase transition at discontinuous bulk transitions, we focus on Potts systems with large numbers of states.

In 1982, R. Lipowsky published a paper where he showed that a continuous critical behavior can be observed at surfaces in cases where the bulk transition is discontinuous [34]. He calculated the surface critical exponents in the framework of Landau theory. The generic form of the Landau expansion of the free energy produces the same set of critical exponents for Potts systems with different dimensionality and different total number of states [32]. In our research, we use Monte Carlo simulations to compute the surface critical exponents of Potts systems with discontinuous transitions in the bulk [33].

Critical Exponents Investigated

For a two-dimensional semi-infinite Potts lattice as shown in Fig.4.4, we computed four different surface critical exponents which are related to four different quantities. These quantities include surface magnetization m_1, surface excess magnetization m_s, surface-surface spin correlation $C_{ss}(x)$ and surface-bulk spin correlation C_{sb} [33].

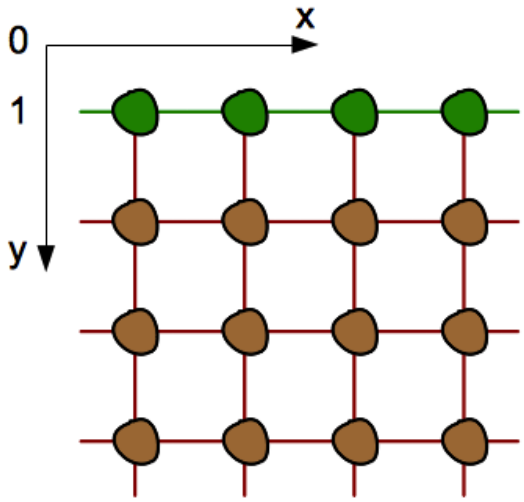

Figure 4.4: Schematic picture of a two-dimensional semi-infinite Potts system.

The local magnetization of the y_{th} row is expressed as:

$$m(y) = (qN_m(y)/L - 1)/(q - 1) \tag{4.2}$$

where $N_m(y)$ is the number of majority spins in the row y. The surface magnetization is the local magnetization at $y = 1$ ($m_1 = m(1)$). The local magnetizations for the layers adjacent to the surface (m(z) with $z \ll \infty$) are smaller than the bulk magnetization ($m_b = m(\infty)$). Thus, we define the surface excess magnetization as follows:

$$m_s = \sum_{y=1}^{\infty}(m_b - m(y)) \tag{4.3}$$

The surface-surface spin correlation and surface-bulk spin correlation are given by:

$$C_{ss}(x) = \frac{q}{q-1}\left\langle \delta(s_{1,1} - s_{x,1}) - \frac{1}{q} \right\rangle - m_1^2 \sim e^{-x/\xi_{\parallel}} \tag{4.4}$$

$$C_{sb}(x) = \frac{q}{q-1}\left\langle \delta(s_{1,1} - s_{1,y}) - \frac{1}{q} \right\rangle - m_1 m(y) \sim e^{-y/\xi_{\perp}} \tag{4.5}$$

Given these four quantities, we can compute the four surface critical exponents $\beta_1, \beta_s, \nu_{\parallel}$ and $\nu_{\perp}$ according to the following relations [32, 34, 35]:

$$m_1 \sim [(T_c(q) - T)/T_c(q)]^{\beta_1} \tag{4.6}$$

$$m_s \sim [(T_c(q) - T)/T_c(q)]^{\beta_s} \tag{4.7}$$

$$\xi_{\parallel} \sim [(T_c(q) - T)/T_c(q)]^{-\nu_{\parallel}} \tag{4.8}$$

$$\xi_{\perp} \sim [(T_c(q) - T)/T_c(q)]^{-\nu_{\perp}} \tag{4.9}$$

In Eq.(4.8) and Eq.(4.9), $\nu_{\parallel}$ and $\nu_{\perp}$ are correlation exponents that respectively stand for the correlations parallel and perpendicular to the surface. In Eq.(4.6)-Eq.(4.9), $T_c(q)$ is the critical temperature of a infinite two-dimensional Potts system whose total number of states is q, whereas $t = (T_c(q) - T)/T_c(q)$ is the reduced temperature.

The explicit expression for the four surface critical exponent can be obtained by taking the logarithm of both sides of the above equations and taking the limit of $t = (T_c(q) - T)/T_c(q) \to 0$. For example, to calculate β_1, we have [30]:

$$\beta_1 = \lim_{t\to 0} \beta_{1,eff}(t) = \lim_{t\to 0} \frac{\mathrm{d}\ln(m_1)}{\mathrm{d}\ln(t)} \tag{4.10}$$

Scaling Relations

In 1999 Iglói and Carlon published a paper discussing the boundary and bulk phase transition in the two-dimensional Potts systems for number of states larger than 4 [36]. They considered two-dimensional Potts lattices with an extra large size (L) in the direction parallel to the free surface, but a very small size (M) in the direction perpendicular to the free surface. The two ends of the ribbon shaped lattice are connected by periodic boundary conditions, whereas at one of the edges of the ribbon a pinned boundary condition (all sites on an edge have the same unchangeable spin state) was used. With such a system at T_c (the critical temperature of the two-dimensional Potts system with infinite size and $q > 4$), it is shown that the surface magnetization m_1 and the lattice width M have the following relation:

$$m_1 \sim M^{-x_1} \tag{4.11}$$

Here x_1 is the scaling dimension. The authors further confirmed the scaling relation involving x_1, β_1 and $\nu_\perp$:

$$x_1 = \beta_1/\nu_\perp \tag{4.12}$$

at both critical and tricritical surface phase transitions.

In the two dimensional semi-infinite system, surface critical exponents and scaling relations can be derived from the singular part of the surface free energy f_s. The scaling form of f_s is given as follows [34]:

$$f_s = |t|^{2-\alpha_s}\, \Omega(|t|^{-\Delta_1}\, h_1) \tag{4.13}$$

Here α_s and Δ_1 are two independent surface exponents, and all other surface critical exponents can be derived from these two exponents. For example, we have [34]:

$$\beta_1 = 2 - \alpha_s - \Delta_1 \tag{4.14}$$

$$\beta_s = 1 - \alpha_s \tag{4.15}$$

$$(d-1)\nu_\parallel = 2 - \alpha_s \tag{4.16}$$

For our two-dimensional Potts lattice, we have $d = 2$. Thus, the combination of Eq.(4.15) and Eq.(4.16) form another important scaling relation:

$$\nu_\parallel = 1 + \beta_s \tag{4.17}$$

In our research, we use the two scaling relations in Eq.(4.12) and Eq.(4.17) to check the consistency of our numerical data from extensive Monte Carlo simulations.

4.1.4 Numerical Data

To study the surface behavior of the Potts system with a large number of states ($q > 4$), we first run Monte Carlo simulations for systems of different q (=5, 9, 16 and 100) with

Table 4.1: Surface critical exponents for two-dimensional Potts models with q states that have a first-order bulk transition.

q	β_1	β_s	$\nu_\parallel$	$\nu_\perp$
5	0.64(2)	−0.63(3)	0.42(3)	0.56(5)
9	0.79(1)	−0.54(2)	0.53(4)	0.46(2)
16	0.90(2)	−0.46(3)	0.55(3)	0.43(2)
100	0.95(2)	−0.40(2)	0.59(2)	0.38(2)

fixed size ($L = 640, M = 320$). At the start of each simulation, the Potts system starts with a pure state at a low temperature. At each temperature point, the parameters $m_1, m_s, C_{ss}(x)$ and $C_{sb}(y)$ are computed (see Eq.(4.2)-Eq.(4.5)).

To obtain β_1 and β_s, we first calculate the effective surface exponent by taking the logarithmic derivative with respect to the reduced temperature t ($=\frac{T-T_c}{T_c}$). Then we take the limit $t \to 0$ for each surface critical exponent. To obtain $\nu_\parallel$ and $\nu_\perp$, we need to calculate first the values of $\ln(C_{ss}(x))$ and $\ln(C_{sb}(y))$ and derive the correlation lengths $\xi_\parallel(t)$ and $\xi_\perp(t)$, from which we can calculate the values of $\nu_\parallel$ and $\nu_\perp$. Table 4.1 show our numerical estimates of the four exponents β_1, β_s, $\nu_\parallel$ and $\nu_\perp$ for systems with different number of states.

Fig.4.5 shows the typical layer magnetizations for systems at $q = 9$ and $q = 100$. The data in Fig.4.5 allow us to calculate $\beta_{1,eff}$ and $\beta_{s,eff}$ at different temperatures [33]. The data of $\beta_{1,eff}$ and $\beta_{s,eff}$ as functions of reduced temperatures are plotted in Fig.4.6.

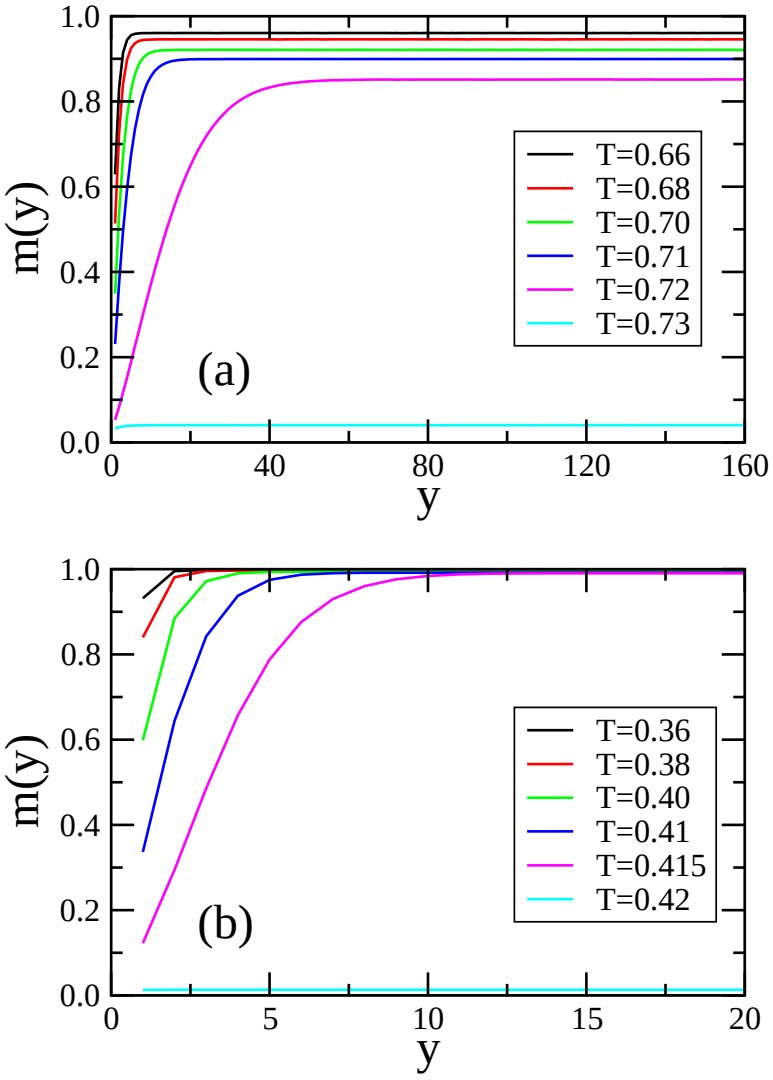

Figure 4.5: (Figure from [33], reprinted with permission from American Physical Society.) Layer magnetization density as a function of layer index y for (a) $q = 9$ and (b) $q = 100$ states. The layer $y = 1$ is the surface layer. Approaching the bulk transition temperature from below, the surface magnetization decreases continuously whereas deep inside the bulk the local magnetization displays a discontinuous jump. The highest temperature included is just above the corresponding bulk transition temperature. The data have been obtained for a system composed of 640×320 spins. Error bars, that result from averaging over typically ten independent runs, are of the order of the thickness of the lines.

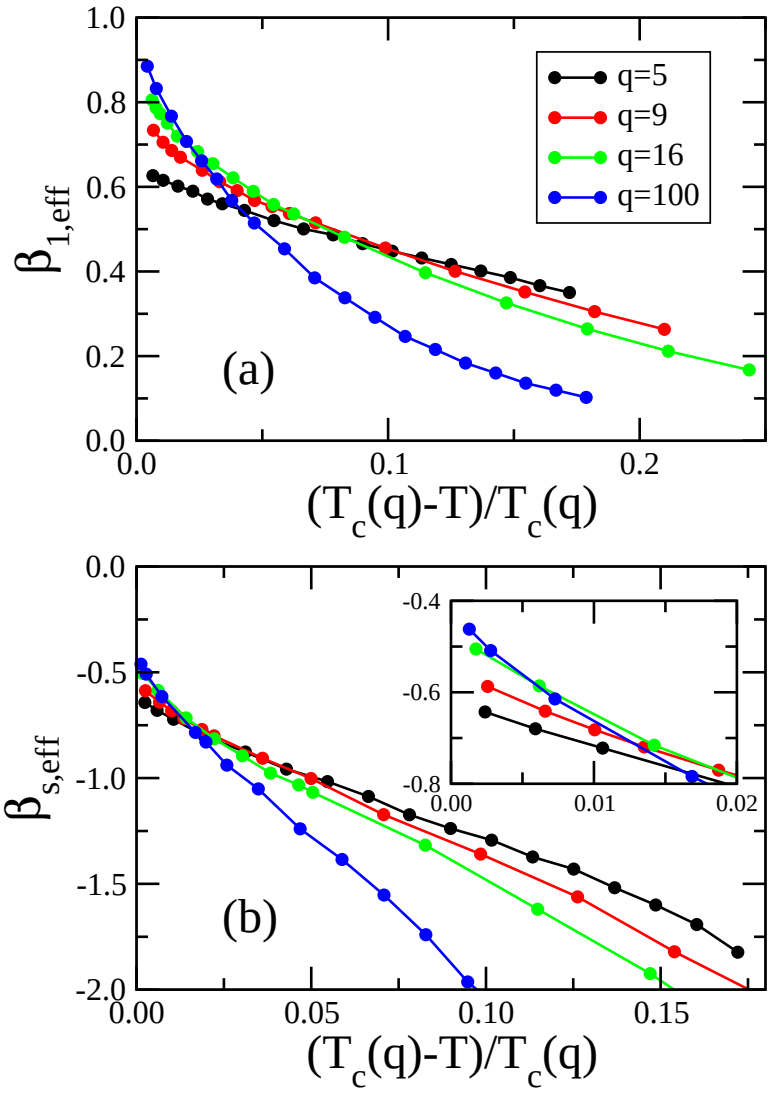

Figure 4.6: (Figure from [33], reprinted with permission from American Physical Society.) (a) Effective exponent of the surface magnetization and (b) effective exponent of the surface excess magnetization as function of the reduced temperature $(T_c(q)-T)/T_c(q)$ for systems with different numbers of states q. Here, $T_c(q)$ is the bulk transition temperature for the model with q states. The inset in (b) shows a blow-up close to the transition temperature. The values of the exponents obtained from extrapolating to the transition temperature are given in Table 4.1. Only data not affected by finite-size effects are shown. Error bars are of the order of the symbol sizes in the main figures.

In Fig.4.6, we first find that the effective exponents changes continuously, which is a signature of second-order phase transition. Extrapolating the data of $\beta_{1,eff}$ and $\beta_{s,eff}$ to $t = 0$ leads to the estimated β_1 and β_s values listed in Table 4.1. Here exploration using different functions results in slightly different values for the critical exponents. The error bars in Table 4.1 take in account the differences made by using different extrapolation functions.

Interestingly, from Fig.4.6(a) and the inset of Fig.4.6(b), we find that $\beta_{1,eff}$ and $\beta_{s,eff}$ approach different values with the decrease of the reduced temperature. In Table 1, the estimated values of both β_1 and β_s are found to depend on the total number of states. This finding is different from what is claimed in [32], where it is stated that the surface critical exponents are identical for systems with different number of states.

In our research, we also obtained estimates for the exponents $\nu_{\parallel}$ and $\nu_{\perp}$. According to Eq.(4.4)-Eq.(4.5), we can first compute the values of $\xi_{\parallel}$ and $\xi_{\perp}$ by finding the ratios $\ln(C_{ss}(x))/x$ and $\ln(C_{sb}(y))/y$. The profiles of $\ln(C_{ss}(x))$ and $\ln(C_{sb}(y))$ for systems with $q = 9$ and different temperatures are shown in Fig.4.7. An exponential dependence on the distance is found in both Fig.4.7(a) and Fig.4.7(b) after some short distance regime, and the ratios $\ln(C_{ss}(x))/x$ and $\ln(C_{sb}(y))/y$ are estimated by finding the slopes of the curves that best fit the data points.

The numerically determined correlation lengths $\xi_{\parallel}$ and $\xi_{\perp}$ are shown in Fig.4.8, as functions of reduced temperature (see the filled and open black circles for the $q = 9$ system). In the same figure, we also show the $\xi_{\parallel}$ and $\xi_{\perp}$ data for the $q = 100$ system (see the filled and open red circles). It is not hard to find from Fig.4.8 that the two curves with same color (red or black) have slightly different slopes, indicating the spatial anisotropy in both the $q = 9$ and $q = 100$ systems. It is also found from Fig.4.8 that the curves with same symbol shape (filled or open circle) also have slightly different slopes. This fact tells us that the exponent $\nu_{\parallel}$ and $\nu_{\perp}$ are q dependent.

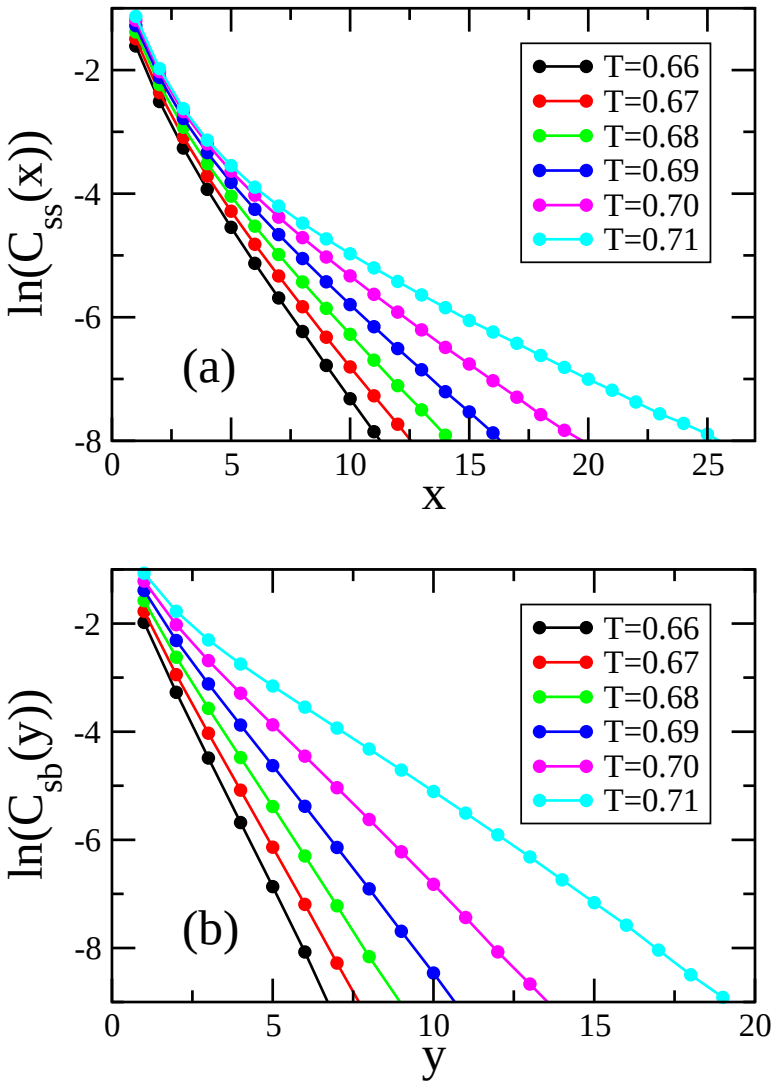

Figure 4.7: (Figure from [33], reprinted with permission from American Physical Society.) (a) Surface-surface and (b) surface-bulk correlation for the $q = 9$ case and different temperatures below the bulk transition temperature. Both quantities display an exponential decay characterized by a typical temperature dependent length, see Fig. 4.8. The data have been obtained for a system with 640×320 spins after averaging over at least fifty independent runs. Error bars are smaller than the size of the symbols.

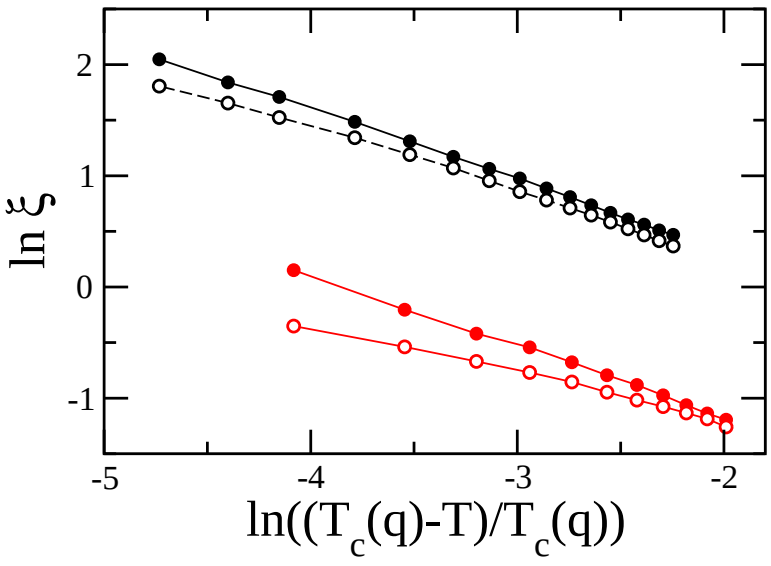

Figure 4.8: (Figure from [33], reprinted with permission from American Physical Society.) Temperature dependent correlation lengths as obtained from the spatial correlation functions, see Fig. 4.7 for examples. The black (red) lines are for the $q = 9$ ($q = 100$) system, with filled (open) symbols indicating the correlation length parallel (perpendicular) to the surface. On approaching the bulk transition temperature the correlation lengths display an algebraic behavior. The values of the correlation length exponents obtained from the slopes in this figure are collected in Table 4.1.

According to Eq.(4.8) and Eq.(4.9), the negative of the slopes found in Fig.4.8 give us the values of $\nu_{\|}$ and $\nu_{\perp}$ for systems with $q = 9$ and $q = 100$ (see Table 4.1). In Table 4.1, we also show our numerical results of $\nu_{\|}$ and $\nu_{\perp}$ for systems with $q = 5$ and $q = 16$.

So far, we have shown how the four surface critical exponents (β_1, β_s, $\nu_{\|}$ and $\nu_{\perp}$) are obtained by numerical simulation. Now, we can first check the correctness of our data $\nu_{\|}$ and β_s (see Table 4.1) by comparing with the scaling relation Eq.(4.17). The value of $\nu_{\|} - \beta_s$ obtained from Table 4.1 is: 1.05±0.06 for $q = 5$, 1.07±0.06 for $q = 9$, 1.01±0.06 for $q = 16$, and 0.99±0.04 for $q = 100$ [33]. Here the values of $\nu_{\|} - \beta_s$ in all four systems with different number of states are close to 1 and thus the data are agree with Eq.(4.17).

According to Eq.(4.12), we need to find the scaling dimension x_1 to check the correctness of β_1 and $\nu_\perp$. As is introduced in the last subsection, we follow [36] and calculate the surface magnetization (m_1) of a two-dimensional ribbon-shaped Potts lattices, as a function of the width (M) of the ribbon-shaped lattice. In [36], the scaling relation Eq.(4.12) is estimated for the $L = \infty$ systems. However, Monte Carlo simulations can only simulate systems with finite L. In our research we vary the size of L and carefully monitor the finite-size effects in that direction.

Fig.4.9(a) shows the data for the surface magnetization as a function of M from our Monte Carlo simulation. From the data of $m_1(M)$ we can obtain an effective exponent x_{eff} by taking the logarithmic derivative:

$$x_{eff}(M) = -\frac{d \ln m_1(M)}{d \ln M} \tag{4.18}$$

The data of x_{eff} are shown in Fig.4.9(b). In this figure, we only include data that are not affected by finite-size effects, where $L = 64000$. In Fig.4.9(b) we also include the data published in [36] (see the data points marked by asterisk symbols), which are x_{eff} values obtained for $q = 9$ systems using DMRG (Density Matrix Renormalization Group). Due to limitation of computation time, in Fig.4.9(b) we only include three data points for the $q = 100$ systems where M values are relatively small. In the same figure estimates for x_1 are shown (see the colored bars on the y axis), as obtained from Table 4.1.

In conclusion, we performed extensive Monte Carlo simulation to study the surface exponents of the two-dimensional Potts systems with first-order bulk transition. From the data of the systems with $q = 5, 9, 16$ and 100, we found that all the four surface exponents under investigation are dependent on the total number of states (q).

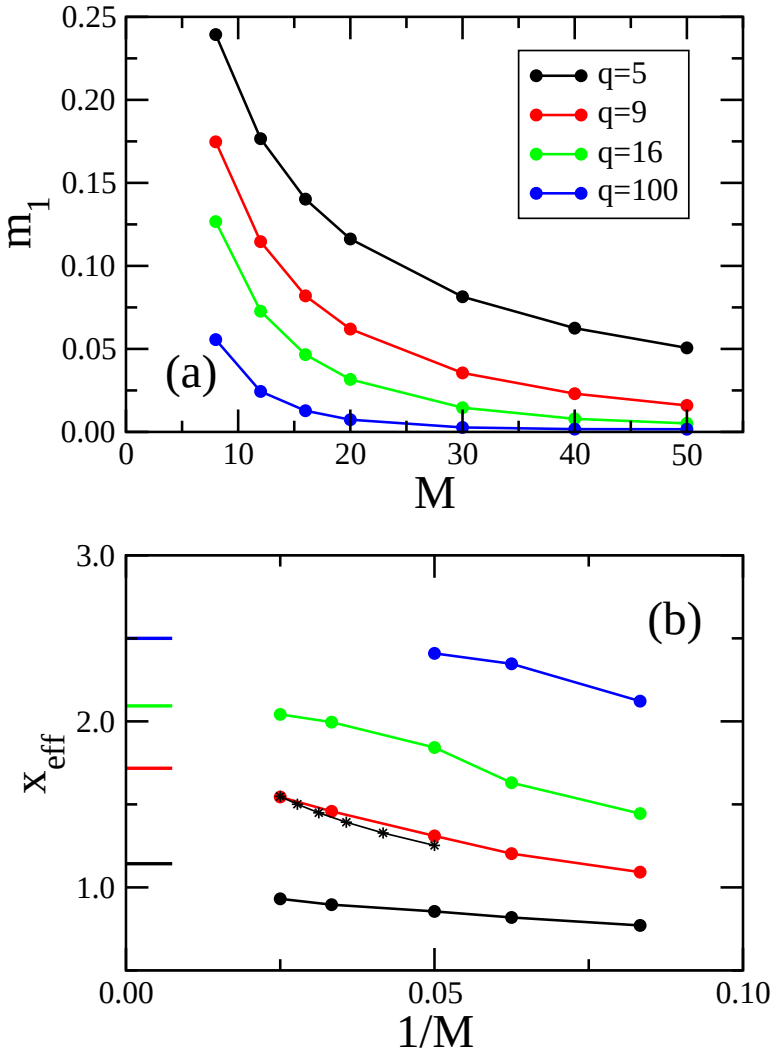

Figure 4.9: (Figure from [33], reprinted with permission from American Physical Society.) (a) Surface magnetization at the bulk transition temperature for stripes of width M where at one of the surfaces we impose fixed boundary conditions. The different curves correspond to different numbers of states q. The length of the system is $L = 64000$. (b) Effective scaling dimension obtained from the data shown in panel (a). Only data not affected by finite size effects are displayed. The bars on the y axis indicate the values obtained from Table I when assuming the scaling relation $x = \beta_1/\nu_\perp$. The stars are the data given in Table IV of Ref. [36] for the $q = 9$ case using DMRG.

4.2 Magnetic Friction between Two Potts Blocks/ Planes

In the last subsection we presented our results on surface critical phenomena at a discontinuous bulk transition. The data from simulations of Potts systems with different values of q show that the surface critical exponents depend on the value of q, which is in contrast to prior claims that these exponents should be universal and independent of q.

In this subsection we study interfacial phenomena in driven systems with magnetic friction. In the following, we will first introduce the model and provide some background information on magnetic friction in spin systems. We will then discuss the non-equilibrium states of the contacting surfaces, which will be followed by a discussion of the related non-equilibrium surface phase transitions.

4.2.1 Background and models

Background

In 2008 Dirk Kadau, Alfred Hucht and Dietrich E. Wolf published a paper discussing magnetic friction in driven Ising systems [37]. In this paper two two-dimensional Ising lattices are studied whose (one-dimensional) surfaces are moving against each other with a sliding velocity v. It was pointed out that during the relative movement energy is pumped into the spin degrees of freedom. In their research, the authors found through Monte Carlo simulations that energy is dissipated from the system to the heat bath, with the energy dissipation rate increasing linearly for small v before saturating for large v.

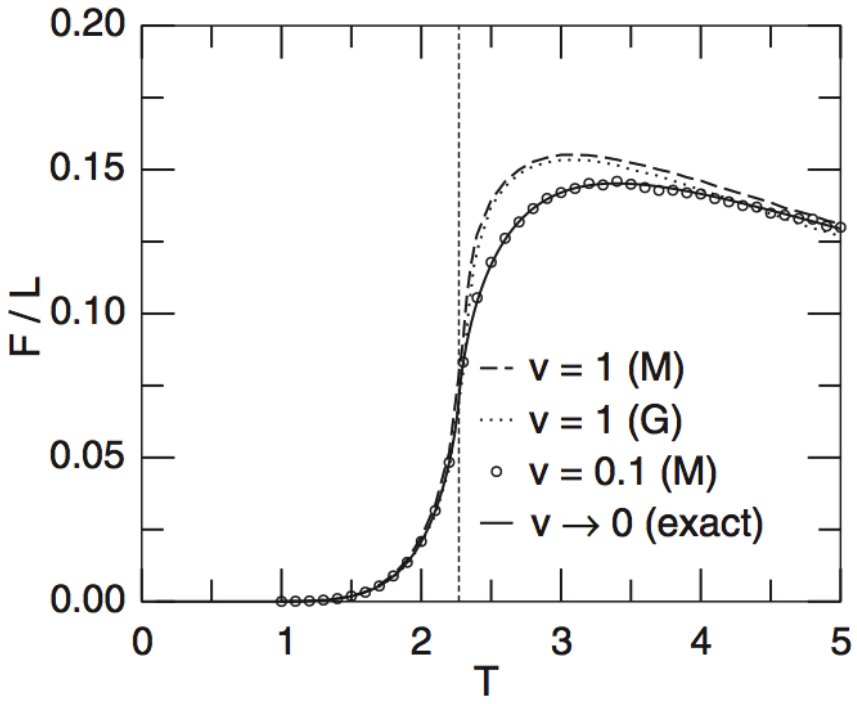

Figure 4.10: (Figure from [37], reprinted with permission from American Physical Society.) Temperature dependence of the friction force per unit length, F/L, in a system of two 40×80 Ising lattices with magnetic friction. Solid line: exact quasi static limit $v \to 0$. Circles: simulation results with Metropolis rates for systems with $v = 0.1$. Dashed (doted) line: simulation results with Metropolis (Glauber) rates for systems with $v = 1$. All data are averaged over 100 runs. The critical temperature is indicated by the dashed vertical line.

This study also found that the magnetic frictional shear stress F/L increases abruptly at the critical temperature, see Fig.4.10.

In the following year, another paper published by Alfred Hucht presented a detailed investigation of the magnetic friction in Ising systems with different geometries [38]. In this paper, the phase transition temperatures and exponents of driven Ising systems of several geometries are analytically derived in the limit of $v = \infty$. In addition, a velocity dependent crossover from the Ising to mean-field universality class is discussed respectively for the $1d$ and $2d_b$ systems. (In a $2d_b$ system, two two-dimensional Ising lattices move against each other along their contacting surfaces.) Interestingly, this paper also shows a phase diagram as a function of velocity v and temperature T for the $2d_b$ system (see Fig.4.11), indicating that the phase transition temperature on the contacting surfaces increases with increasing v and saturates at high values of v.

Recently, magnetic friction in other types of spin models has also been investigated, including the Heisenberg model [39] and the Potts model [40]. The paper [39] focuses on velocity dependent crossover phenomena in systems with magnetic friction, whereas paper [40] presents a detailed study of magnetic friction in one- and two-dimensional Potts systems. Compared to the Ising systems, magnetic friction in Potts system shows many new features. For example, for a two-dimensional Potts system it is found that the magnetic frictional shear stress F/L becomes discontinuous at the phase transition temperature $T_c(q)$ if q (the total number of states of the Potts system) exceeds 3, compare Fig.4.10 and Fig.4.12. It is also shown in this paper how the surface properties of Potts systems with different q values are altered by changing the system parameters κ (the interfacial coupling strength) and v (the driving velocity). For example, interface magnetizations are calculated through simulations of Potts systems in full heating and cooling cycles, which form hysteresis curves from which one can study the non-equilibrium phase transitions of the systems. Fig.4.13 shows the interface magnetization data for the $q = 9$ systems. Interestingly, this study shows that the phase transition on the contacting

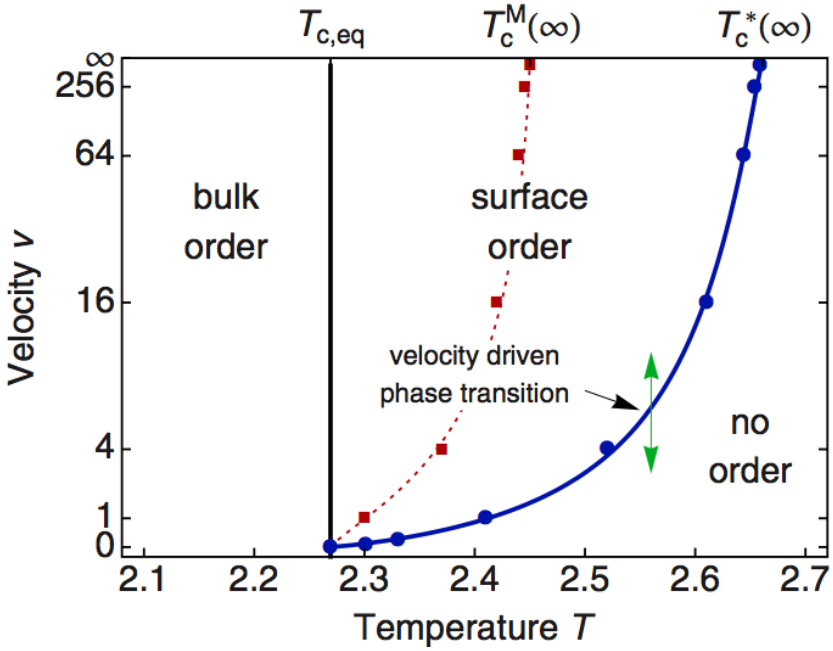

Figure 4.11: (Figure from [38], reprinted with permission from American Physical Society.) Phase diagram of the $2d_b$ case. Below $T_{c,eq}$ the two-dimensional bulk is ordered, while surface order is observed even above $T_{c,eq}$ up to the velocity dependent phase boundary $T_c(v)$. The position of this boundary depends on the algorithm, the blue line holds for the multiplicative rate, while the thin red dotted line holding for the Metropolis rate. At fixed temperatures between $T_{c,eq}$ and $T_c(v)$ a velocity driven phase transition is possible. The points are results from MC simulations.

interface in a two-dimensional Potts system changes from continuous for $\kappa = 0.5$ to discontinuous for $\kappa = 1$ (here κ denotes the interfacial coupling constant where the in-bulk coupling constant is equal to 1), and that the critical temperature increases from 0.72 for $\kappa = 1$ to 0.78 for $\kappa = 2$, see Fig.4.13(a). On the other hand, this research also shows that the phase transition on the interface is hardly changed when varying the driving velocity at the constant interfacial coupling $\kappa = 1$, see Fig.4.13(b).

In the following, we introduce the three-dimensional Potts lattices with magnetic friction

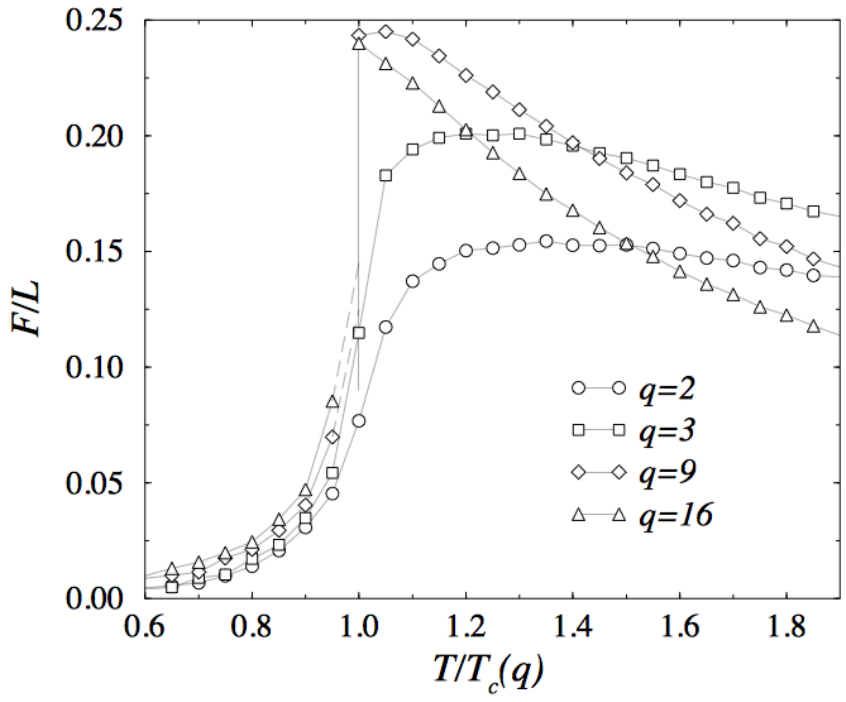

Figure 4.12: (Figure from [40], reprinted with permission from American Physical Society.) Temperature dependence of the friction force per unit length, F/L, in a system of two 40×80 Potts lattices with magnetic friction, where the driving velocity $v = 1$. At $T_c(q)$, F/L becomes discontinuous when $q > 3$.

whose properties will be studied later in this section.

The Two-Block Systems

In our study the system is made up of two three-dimensional Potts blocks. The Hamiltonian for a three-dimensional Potts system can be written as follows:

$$H = -\sum_{x,y,z} [J^{\hat{x}}_{x,y,z}\delta(S_{x,y,z}, S_{x+1,y,z}) + J^{\hat{y}}_{x,y,z}\delta(S_{x,y,z}, S_{x,y+1,z}) + J^{\hat{z}}_{x,y,z}\delta(S_{x,y,z}, S_{x,y,z+1})] \quad (4.19)$$

For the Ising system, the spin value $S_{x,y,z}$ can only take the values 1 or -1, representing

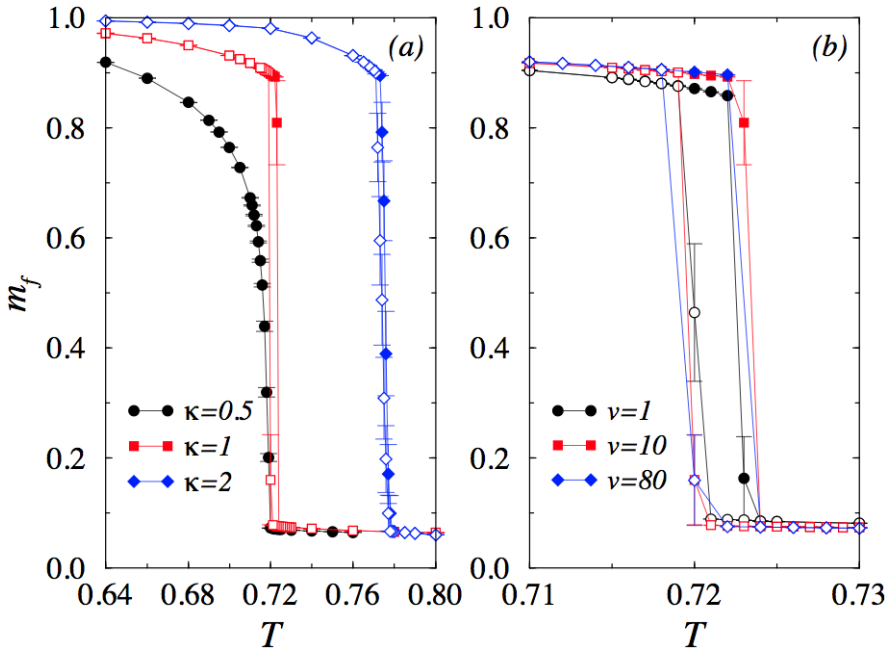

Figure 4.13: (Figure from [40], reprinted with permission from American Physical Society.) Interface magnetization for the $q = 9$ Potts model, with (a) $v = 10$ and various values of κ and (b) $\kappa = 1$ and various values of v. The discontinuous character of the phase transition is revealed by the presence of a thermal hysteresis [filled (open) symbols result when heating (cooling) the system].

the two possible states. For the Potts system with q states, the spin value $S_{x,y,z}$ can take one of the values $0, 1, 2, ..., q-1$. In Eq.(4.19), $J^{\hat{x}}_{x,y,z}(>0)$ is the interaction strength of the coupling between the neighboring sites $S_{x,y,z}$ and $S_{x+1,y,z}$. Likewise, $J^{\hat{y}}_{x,y,z}(>0)$ is the strength of the coupling between $S_{x,y,z}$ and $S_{x,y+1,z}$ and $J^{\hat{z}}_{x,y,z}(>0)$ is the strength of the coupling between $S_{x,y,z}$ and $S_{x,y,z+1}$.

Fig.4.14(a) shows the typical situation considered in the following, where the upper 3D magnetic block is moving in y direction with speed v relative to the lower 3D magnetic block. To each of the two finite-size Potts blocks we assign a length L, a width W and a height H. Thus, for the upper block, $x/y/z$ runs from 1 to $W/L/H$, whereas for the

lower block, x/y also runs from 1 to W/L, while z runs from $H+1$ to $2H$.

Periodic boundary conditions are applied in all three directions so that there are four contacting surfaces located at $z = 1, H, H+1$ and $2H$ (as highlighted by the dark green planes).

In order to model magnetic friction between the two 3D blocks, we introduce interactions between the surfaces of the blocks. As shown in Fig.4.14(c) and (d), we introduce $J^{\hat{z}}_{x,y,H}$ and $J^{\hat{z}}_{x,y,2H}$ to be the coupling constants that couple the sites of immediate contact between the two blocks. These interfacial coupling constants can differ from the coupling constants inside the 3D lattices. In order to model friction between blocks moving with respect to each other with relative speed v, we move the upper block in y direction v times during each Monte Carlo step (there are $W \times L \times 2H$ attempts of single spin updates of a single spin in each Monte Carlo step). Thus, the Hamiltonian for the system under investigation reads:

$$H(t) = H^{(s)} + V(t) \tag{4.20}$$

$$\begin{aligned} H^{(s)} = -\sum_{x=1}^{W}\sum_{y=1}^{L}\sum_{z=1}^{2H}[J^{\hat{x}}_{x,y,z}\delta(S_{x,y,z}, S_{x+1,y,z}) + J^{\hat{y}}_{x,y,z}\delta(S_{x,y,z}, S_{x,y+1,z})] - \\ \sum_{x=1}^{W}\sum_{y=1}^{L}\sum_{z=1(z\neq H)}^{2H-1} J^{\hat{z}}_{x,y,z}\delta(S_{x,y,z}, S_{x,y,z+1}) \end{aligned} \tag{4.21}$$

$$V(t) = -\sum_{x=1}^{W}\sum_{y=1}^{L}[J^{\hat{z}}_{x,y,H}\delta(S_{x,y+vt,H}, S_{x,y,H+1}) + J^{\hat{z}}_{x,y,2H}\delta(S_{x,y+vt,2H}, S_{x,y,1})] \tag{4.22}$$

where $H^{(s)}$ is the energy inside the blocks and $V(t)$ is the energy between the contacting surfaces.

As shown in Eq.(4.22), the interfacial coupling constants $J^{\hat{z}}_{x,y,z}$ ($x = 1, 2, ...W, y = 1, 2, ...L$, $z = H, 2H$) and the driving velocity $v\hat{y}$ are the factors that determine the magnetic friction energy. For simplification, we set the interfacial couplings to be of equal strength κ_f, while the coupling constants for the sites inside the blocks are given by another constant κ (we

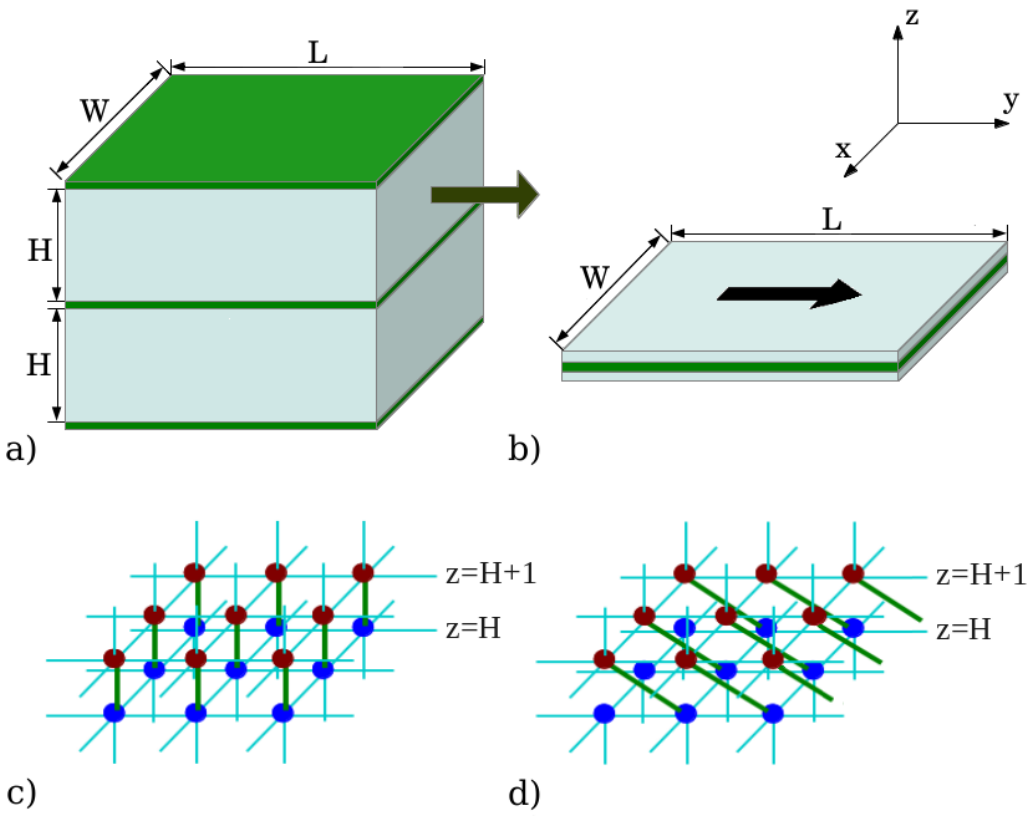

Figure 4.14: a) Schematic sketch of the two-block 3D Potts system. Each of the two blocks has a finite lattice size of $W \times L \times H$. The lower half is at rest, while the upper half moves in y direction with a driving velocity $v\hat{y}$. The dark green color highlights the interfacial couplings of the two blocks. Periodic boundary conditions are applied in all three directions. b) Schematic sketch of the two-plane Potts system. c) Interfacial coupling between the contacting surfaces of the two blocks before the shift of the upper lattice. d) Interfacial coupling between the two blocks after the upper block shifts a distance of one lattice size in the y direction. Instead of moving the complete upper block by one lattice constant, we form new bonds between spins at the interface.

kept $\kappa = 1$ in our simulation so that $\kappa_f/\kappa = \kappa_f$). As a result, Eq.(4.21) and Eq.(4.22) can be rewritten as:

$$H^{(s)} = -\sum_{x=1}^{W}\sum_{y=1}^{L}\sum_{z=1}^{2H}[\delta(S_{x,y,z}, S_{x+1,y,z})+\delta(S_{x,y,z}, S_{x,y+1,z})]-\sum_{x=1}^{W}\sum_{y=1}^{L}\sum_{z=1(z\neq H)}^{2H-1}\delta(S_{x,y,z}, S_{x,y,z+1}) \tag{4.23}$$

$$V(t) = -\kappa_f\sum_{x=1}^{W}\sum_{y=1}^{L}[\delta(S_{x,y+vt,H}, S_{x,y,H+1}) + \delta(S_{x,y+vt,2H}, S_{x,y,1})] \tag{4.24}$$

The Two-Plane Systems

We also studied systems made up of two coupled two-dimensional Potts lattices. The Hamiltonian for a two-dimensional Potts system can be written as follows:

$$H = -\sum_{x,y}[J^{\hat{x}}_{x,y}\delta(S_{x,y}, S_{x+1,y}) + J^{\hat{y}}_{x,y}\delta(S_{x,y}, S_{x,y+1})] \tag{4.25}$$

As before, $S_{x,y}$ stands for the spin located at (x,y), which can take on values from 0 to $q-1$. $J^{\hat{x}}_{x,y}$ is the coupling constant between neighboring sites in x-direction, and $J^{\hat{y}}_{x,y}$ is the coupling constant between neighbors in y-direction.

In Fig.4.14(b), the upper 2D plane is moving in y direction with speed v relative to the lower 2D plane. The sizes of the two planes are identical and equal to $W \times L$. We have periodic boundary condition in both x and y directions. These two planes are coupled so that the Hamiltonian for this 2D-plane system reads:

$$H(t) = H^{(s)} + H'^{(s)} + V(t) \tag{4.26}$$

$$H^{(s)} = -\sum_{x=1}^{W}\sum_{y=1}^{L}[J^{\hat{x}}_{x,y}\delta(S_{x,y}, S_{x+1,y}) + J^{\hat{y}}_{x,y}\delta(S_{x,y}, S_{x,y+1})] \tag{4.27}$$

$$H'^{(s)} = -\sum_{x=1}^{W}\sum_{y=1}^{L}[J'^{\hat{x}}_{x,y}\delta(S'_{x,y}, S'_{x+1,y}) + J'^{\hat{y}}_{x,y}\delta(S'_{x,y}, S'_{x,y+1})] \tag{4.28}$$

$$V(t) = -\sum_{x=1}^{W}\sum_{y=1}^{L}[J_{x,y}^{\hat{z}}\delta(S_{x,y+vt}, S'_{x,y})] \tag{4.29}$$

As shown in Eq.(4.26), the Hamiltonian is formed by three parts: the first part gives the energy in the upper plane; the second part gives the energy in the lower plane; the third part gives the interaction energy between the two planes. Here $J_{x,y}^{\hat{x}}$, $J_{x,y}^{\hat{y}}$, $J_{x,y}^{\prime\hat{x}}$ and $J_{x,y}^{\prime\hat{y}}$ are coupling constants for the interactions in x and y direction in the upper and lower plane, while $J_{x,y}^{\hat{z}}$ stands for the strength of the coupling between the planes.

We can simplify the Hamiltonian of the two-plane system by setting all the interfacial coupling constants $J_{x,y}^{\hat{z}}$ $(x = 1, 2, ...W, y = 1, 2, ...L)$ to be κ_f, whereas all the other coupling constants are set to be 1. We then have:

$$H^{(s)} = -\sum_{x=1}^{W}\sum_{y=1}^{L}[\delta(S_{x,y}, S_{x+1,y}) + \delta(S_{x,y}, S_{x,y+1})] \tag{4.30}$$

$$H'^{(s)} = -\sum_{x=1}^{W}\sum_{y=1}^{L}[\delta(S'_{x,y}, S'_{x+1,y}) + \delta(S'_{x,y}, S'_{x,y+1})] \tag{4.31}$$

$$V(t) = -\kappa_f\sum_{x=1}^{W}\sum_{y=1}^{L}[\delta(S_{x,y+vt}, S'_{x,y})] \tag{4.32}$$

4.2.2 Non-equilibrium States

In order to understand the non-equilibrium steady states at the contacting surfaces, the first quantity that we study is the average surface magnetization in the steady state, which for the q-state Potts model is given by:

$$\overline{\langle m(T)\rangle} = \frac{1}{4}\sum_{z=1,H,H+1,2H}(\frac{qN_m(z,T)}{WL} - 1)/(q-1) \tag{4.33}$$

Here, $\overline{O}$ represents the time average of a quantity O and $\langle O\rangle$ represents the ensemble average of that quantity. $N_m(z,T) = \max(N_0, N_1, ..., N_{q-1})$, where N_i is the average

number of spins in state i in layer z at temperature T. The sum is over all four interfaces of our two-block systems.

For the study of magnetic friction, where anisotropic surface configurations are observed, we also introduce the *directional surface magnetizations* $m_y(T)$ and $m_x(T)$. Here $m_y(T)$ is used to characterize the order of the spin states parallel to the direction of the relative motion, whereas $m_x(T)$ is used to characterize the order of the spin states perpendicular to that direction. The equations for the average directional surface magnetizations are given by:

$$\overline{\langle m_y(T)\rangle} = \frac{1}{4W} \sum_{z=1,H,H+1,2H} \sum_{x=1}^{W} (\frac{qN_m(x,z,T)}{L} - 1)/(q-1) \tag{4.34}$$

$$\overline{\langle m_x(T)\rangle} = \frac{1}{4L} \sum_{z=1,H,H+1,2H} \sum_{y=1}^{L} (\frac{qN_m(y,z,T)}{W} - 1)/(q-1) \tag{4.35}$$

Eq.(4.34) describes the average directional surface magnetization in the y direction, with $N_m(x,z,T) = \max(N_0, N_1, ..., N_{q-1})$, where N_i is now the average number of spins in state i in layer z and row x. Likewise, Eq.(4.35) describes the average directional surface magnetization in the x direction, with $N_m(y,z,T) = \max(N_0, N_1, ..., N_{q-1})$, where N_i is the average number of spins in state i in layer z and column y. A comparison between $\overline{\langle m_x(T)\rangle}$ and $\overline{\langle m_y(T)\rangle}$ helps us to identify the anisotropy of the surface magnetization.

The corresponding expressions for the average directional surface magnetizations are readily obtained for the system composed of two Potts planes.

In the following, we will introduce the different types of non-equilibrium steady states encountered in our systems.

The Weak Anisotropy State

Fig.4.15 shows the time evolution of the surface configurations of the two-block and two-plane systems, where $q = 2$, $\kappa_f = 5$, $v = 80$ and T=3 ($> T_c$). To obtain these configurations, we start the Monte Carlo simulation from a pure state ($S_{x,y} = q - 1$). During the simulation, we take snapshots of the surface configurations of the lower block (plane) at different times ($t = 100, 1000$ and 10000 Monte Carlo Steps).

From Fig.4.15(b) we find that weak anisotropic surface configurations are formed at $t =$ 1000 MCS in the two-block system. For the two-plane system, see Fig.4.15(d), a weak anisotropy shows up as early as $t = 100$ MCS after starting the simulation. In both systems, the anisotropy of the surface magnetization is clearly visible at the 10000^{th} MCS, see Fig.4.15(c)(f).

By looking carefully at the snapshot at $t = 10000$ MCS, we remark that the y direction is more ordered than the x direction, but that the differences are not huge. We call this type of non-equilibrium surface state the *weak anisotropy state*.

The Strong Anisotropy State

Fig.4.16 shows time evolutions of the surface configurations of the two-block and two-plane systems, where $q = 3$, $\kappa_f = 9$, $v = 80$ and T=2.5 ($> T_c$). The snapshots are obtained in the same way as those obtained in Fig.4.15.

Due to the combination of strong interfacial coupling and large driving velocity, phase-separated stripe-shaped clusters are rapidly formed on the contacting surfaces of the two-block system, see Fig.4.16(a)(b)(c). Phase-separated stripe-shaped clusters are also formed on the surface of the two-plane system, see Fig.4.16(d)(e)(f). This strong anisotropy of the spin states is dominating the non-equilibrium steady states.

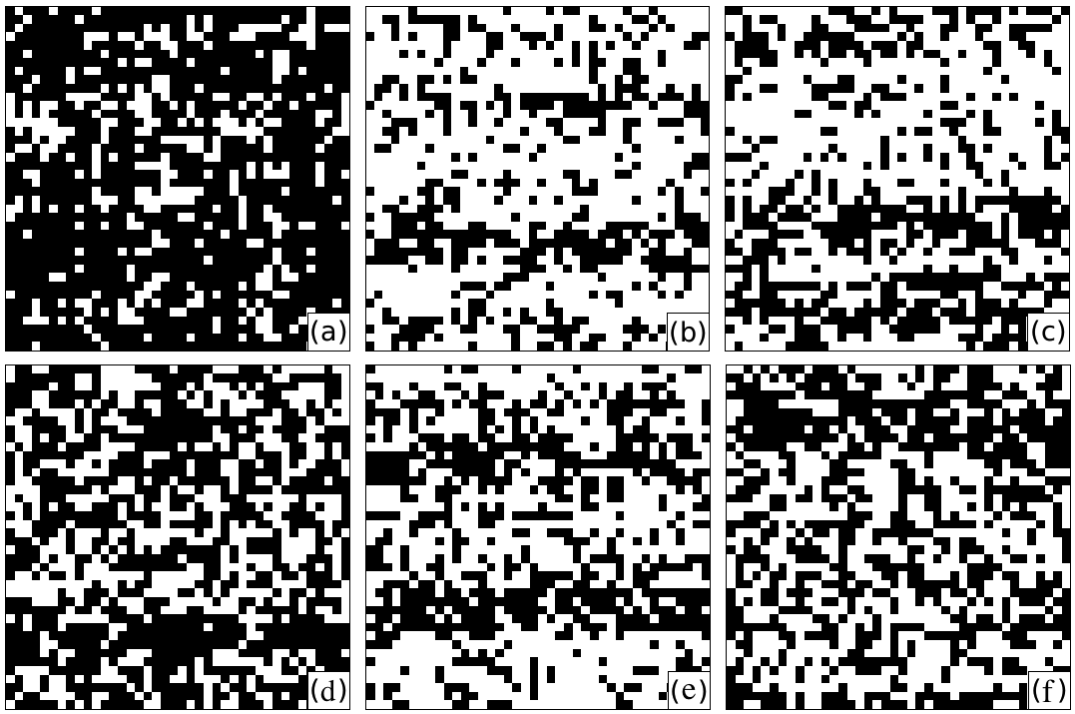

Figure 4.15: (a)(b) and (c) show surface configurations in the layer $z = H$ of a two-block system ($W = L = 2H = 40$) at the times $t = 100, 1000$, and 10000 MCS. (d)(e) and (f) show surface configurations on the lower plane of a two-plane system ($W = L = 40$) at the times $t = 100, 1000$, and 10000 MCS. In both systems, $v = 80$, $\kappa_f = 5$, and $q = 2$. Black color denotes $S_{x,y} = 1$, whereas white color denotes $S_{x,y} = 0$.

Careful observation of the snapshots of the systems at $t = 10000$ reveal one common characteristics, see Fig.4.16(c) and (f): the directional surface magnetization in y direction is much larger than the directional surface magnetization in x direction as the system displays long-range order in direction of the drive. We call this type of non-equilibrium surface state the *strong anisotropy state*.

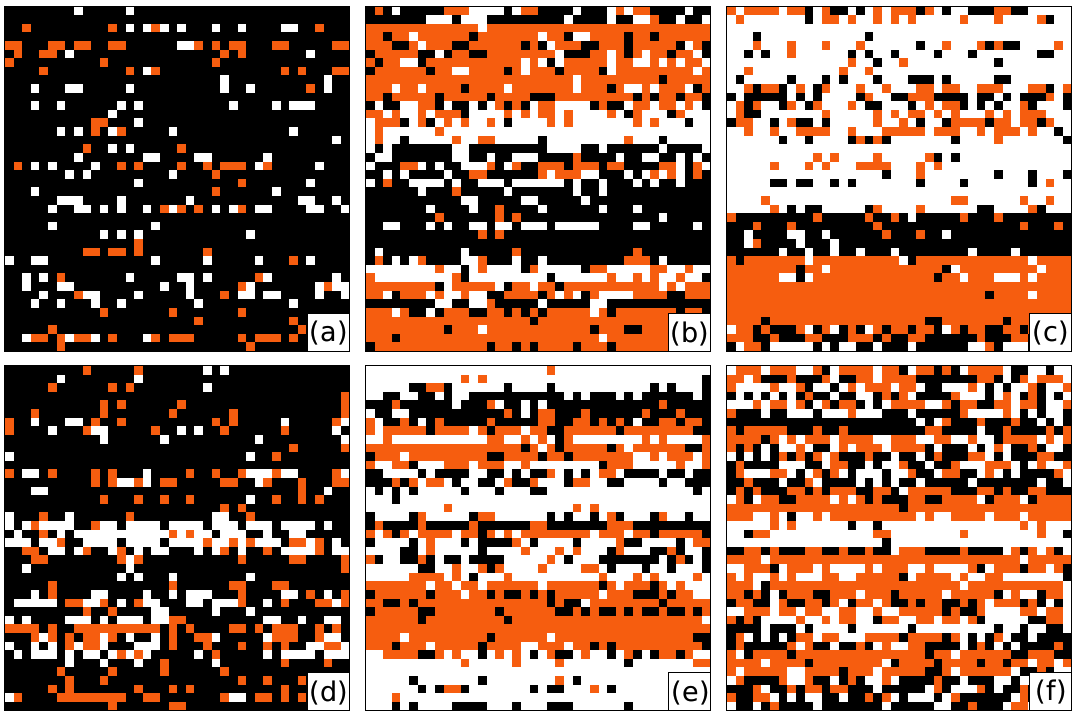

Figure 4.16: (a)(b) and (c) show surface configurations in the layer $z = H$ of a two-block system ($W = L = 2H = 40$) at the times $t = 100, 1000$, and 10000 MCS. (d)(e) and (f) show surface configurations on the lower plane of a two-plane system ($W = L = 40$) at the times $t = 100, 1000$, and 10000 MCS. In both systems, $v = 80$, $\kappa_f = 9$, and $q = 3$. Black color denotes $S_{x,y} = 2$, orange color denotes $S_{x,y} = 1$, and white color denotes $S_{x,y} = 0$.

The Homogeneous State

Fig.4.17 shows time evolutions of the surface configurations of the two-block and two-plane systems with $q = 9$, $\kappa_f = 5$, $v = 80$ and T=1.6 ($> T_c$), i.e. for a large number of states.

For these parameter values the contacting surfaces of both systems maintain for some time structures reminiscent to the initial state where all sites had the spin state $S_{x,y} = q-1 = 8$,

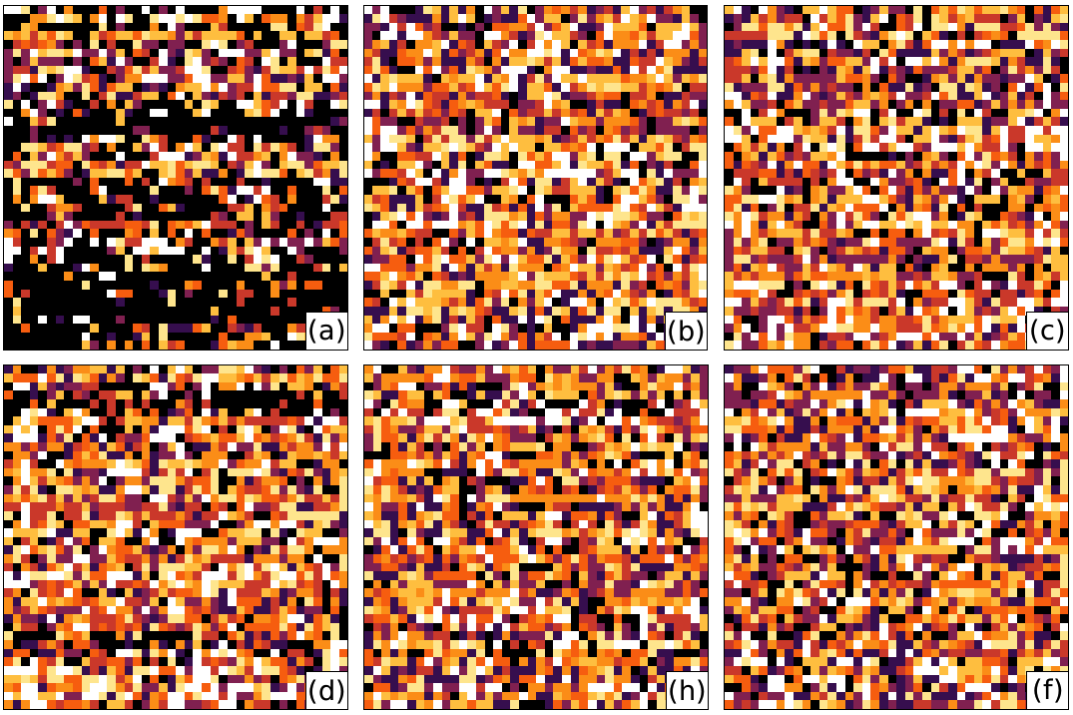

Figure 4.17: (a)(b) and (c) show surface configurations of the layer $z = H$ of a two-block system ($W = L = 2H = 40$) at the times $t = 100, 1000$, and 10000 MCS. (d)(e) and (f) show surface configurations in the lower plane of a two-plane system ($W = L = 40$) at the times $t = 100, 1000$, and 10000 MCS. In both systems, $v = 80$, $\kappa_f = 5$, and $q = 9$. Black color denotes $S_{x,y} = 8$, the initial ordered state, whereas white color denotes $S_{x,y} = 0$. Spin states 0, 1, 2, ..., 8 are represented by 9 different colors from white to black.

see Fig.4.17(a) and Fig.4.17(d).

At later times, the memory of the initial state is lost, see Fig.4.17(c)(f). One common characteristic of the resulting steady states is that the spins are not ordered in any direction. More specifically, the directional surface magnetizations in x and y directions are exactly the same. In these cases we say that the systems are in the *homogeneous state*.

To quantitatively distinguish the three mentioned states in this section, we should first calculate the spin-spin correlation functions in the directions parallel and perpendicular to the relative movement of the two block. The form of the correlation is similar to Eq.(4.4), from which we can obtain the correlation lengths for parallel surface spin-spin correlation $\xi^s_{||}$ and perpendicular surface spin-spin correlation $\xi^s_{\perp}$. The systems in *homogeneous state* typically have $\xi^s_{\perp}/\xi^s_{||} = 1$, the systems in *weak anisotropy state* typically have $\xi^s_{\perp}/\xi^s_{\|}$ larger than 1 but still of the order of 1, and the systems in *strong anisotropy state* typically have $\xi^s_{\perp}/\xi^s_{\|} \gg 1$.

4.2.3 Non-equilibrium Surface Phase Transition

It follows from the previous discussion that we have three regimes according to the interfacial coupling strength κ_f: (1) the weak interfacial coupling regime where $\kappa_f \leq 1$; (2) the medium interfacial coupling regime where $1 < \kappa_f \leq 6$; and (3) the strong interfacial coupling regime where $\kappa_f > 6$.

Phase Transition in the Weak Interfacial Coupling Regime

To understand the effect of weak interfacial couplings, we study the surface magnetization (see Eq.(4.33)) in heating and cooling processes for systems with speeds between 0 and 10. In our simulations, we start each system from a pure state ($S_{x,y,z} = q-1$) at temperature

$T = 0$ and let the system relax for 5000 Monte Carlo steps (MCS). We then measure the average surface magnetization over 1000 MCS. When these first 6000 steps are completed, we raise the system temperature by some amount and repeat this procedure for each new temperature until the maximum temperature T_{max} is reached ($T_{max} > T_c$ is a temperature with a disordered steady state). This heating process is followed by a cooling process where the temperature is decreased in small steps.

It is known from many previous studies that the phase transition in the three-dimensional equilibrium Ising model is of second order [44], whereas the phase transition in the equilibrium three-dimensional Potts lattice with $q = 3$ is of weak first order [45]. In addition, as discussed in Section 4.1, the surface magnetization for the $q = 3$ case changes continuously at the bulk discontinuous transition. Here we are interested in the behavior of the surface magnetization of the contacting surfaces at different temperatures for small κ_f and $v > 0$. Fig.4.18(a) and Fig.4.18(b) show the surface magnetization of the $q = 2$ and $q = 3$ systems with $v = 0$ and $v = 10$ during the heating process.

In Fig.4.18(b) we find that both the equilibrium surface phase transition (with $v = 0$) and the non-equilibrium surface transition (with $v = 10$) of a $q = 3$ system are continuous if the interfacial coupling constant is small (κ_f =0.25 and 0.5, see the black, red and green curves). From Fig.4.18(a) and (b), we also note a great enhancement of the surface magnetization in systems with a larger κ_f and non-zero v (see the green, blue and pink curves in both figures). Interestingly, in both $q = 2$ and $q = 3$ systems with $\kappa_f = 1$ and $v = 10$ the surface phase transition temperature is increased. For the $q = 2$ system the critical temperature of the surface phase transition is shifted from 2.257 to 2.285, whereas for the $q = 3$ system the temperature changes from 1.816 to 1.825.

To gain a better understanding of the effect of magnetic friction on critical properties of the contacting surfaces, we also investigated the "effective exponent" $\beta_{eff}(\tau)$ as a function of the reduced temperature $\tau = (T_c - T)/T_c$, whose symptotic values for $\tau \to 0$

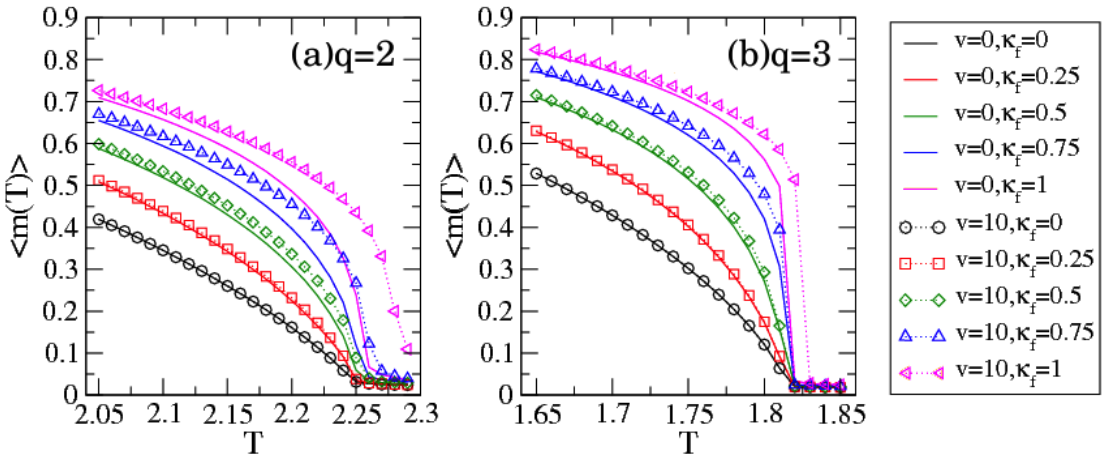

Figure 4.18: Hysteresis curves of the average surface magnetization $\langle m(T)\rangle$ of the three-dimensional two-block systems with $W = L = 2H = 80$. (a) and (b) show the surface magnetization for $q = 2$ and $q = 3$ with $\kappa_f = 0, 0.25, 0.5, 0.75, 1$ and $v = 0, 10$. Each of the data point results from averaging over 30 independent runs. Errors bars are smaller than the size of the symbols.

yields the exact value of the critical exponent β of the surface magnetisation. $\beta_{eff}(\tau)$ can be calculated from the data of the surface magnetization of the system in the following way [42]:

$$\beta_{eff}(\tau) = \frac{d\ln(m)}{d\ln(\tau)} = \frac{\ln(m(\tau_i)/m(\tau_{i+1}))}{\ln(\tau_i/\tau_{i+1})} \tag{4.36}$$

where $\tau_i = (\tau_c - \tau_i)/\tau_c$ is the reduced temperature, $\tau = (\tau_i + \tau_{i+1})/2$, and $m(\tau_i) = \overline{\langle m(\tau_i)\rangle}$ is the average surface magnetization at the reduced temperature τ_i. One point that needs our attention is that the critical temperature of the surface transition may change as a function of system parameters.

Fig.4.19 shows the $\beta_{eff}(\tau)$ data of the $q = 2$ and $q = 3$ systems with $v = 0$ and $v = 10$. From Fig.4.19(a), we can directly read off the critical exponent β for the surface and bulk

magnetization in the three-dimensional Ising system (see the black and pink curves in Fig.4.19(a) respectively). For the system with $v = 0$, $\kappa_f = 0$ and $\tau = 0.0144$, the data shows $\beta_{eff}(\tau) = 0.823$. For the system with $v = 0$, $\kappa_f = 1$ and $\tau = 0.0144$, the data shows $\beta_{eff}(t) = 0.332$. The value of 0.823 is fairly close to 0.80(1), the critical exponent of the surface magnetization of a three-dimensional Ising system [42], whereas the value of 0.332 is very close to 0.3265(3), the critical exponent of the bulk magnetization of a three-dimensional Ising system [43]. This confirms the correctness of our calculations for $\beta_{eff}(\tau)$. In general, we see in Fig.4.19(a) that the critical behavior on the contacting surface transits from surface behavior to bulk behavior with the increase of κ_f. A similar behavior is observed for the $q = 3$, $v = 0$ systems, see Fig.4.19(b). The value of $\beta_{eff}(\tau)$ for systems with $\kappa_f = 0, 0.25, 0.5, 0.75$ and 1 at the smallest temperature ($\tau = 0.0117$) is equal to 0.663, 0.630, 0.504, 0.291 and 0.149 respectively. This reflects a transition from the surface behavior, where the surface magnetization vanishes continuously, to the bulk behavior where the magnetization is discontinuous at the phase transition.

Comparing the data in Fig.4.19(a) and Fig.4.19(c), we find that the effective exponent $\beta_{eff}(\tau)$ is always smaller in Ising systems with relative movement ($v = 10$) when $\kappa_f = 0.5, 0.75$ or 1. A similar behavior is observed for the $q = 3$ Potts systems (see Fig.4.19(b) and Fig.4.19(d)). The differences of the $\beta_{eff}(\tau)$ values between moving and non-moving systems quantifies the effect of magnetic friction observed in Fig.4.18. (The $\beta_{eff}(\tau)$ data for the $v = 1$ and κ_f systems are calculated with estimated transition temperatures 2.285 and 1.825, for $q = 2$ and $q = 3$ systems respectively. These estimated temperatures are obtained from Monte Carlo simulations.)

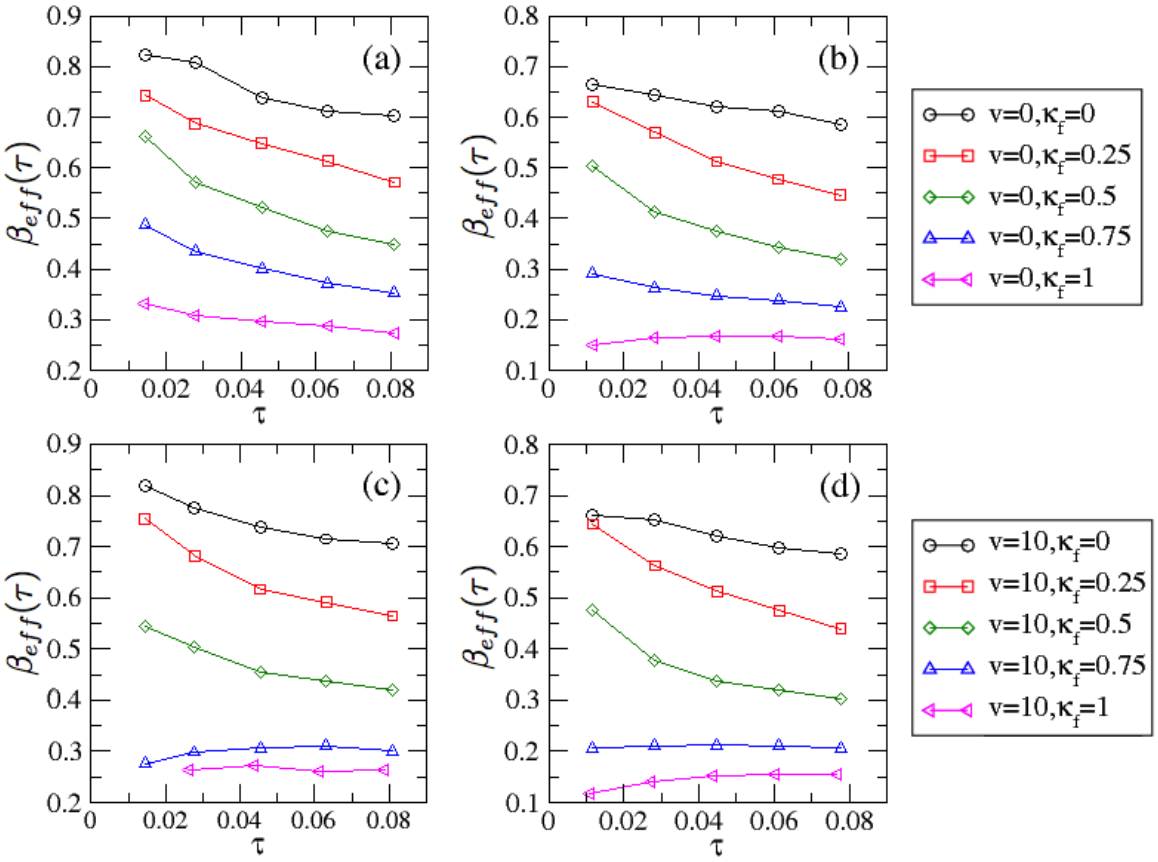

Figure 4.19: $\beta_{eff}(\tau)$ of the three-dimensional two-block systems with $W = L = 2H = 80$. (a) and (b) show $\beta_{eff}(\tau)$ for the $q = 2$ and $q = 3$ systems with $v = 0$, whereas (c) and (d) show $\beta_{eff}(\tau)$ of $q = 2$ and $q = 3$ systems when $v = 10$. The values of $\beta_{eff}(\tau)$ are derived from the data of the average surface magnetization shown in Fig.4.18. Error bars are of the same order of the symbol sizes.

In our research, we also investigated the effect of weak interfacial coupling through the average directional surface magnetization (see Eq.(4.34) and Eq.(4.35)). Similar to the protocol for obtaining the hysteresis loops for the surface magnetization, we let the systems (with different q values ($q = 2, 3$ and 9), different velocities ($v = 0, 1, 10, 80$), and constant $\kappa_f = 1$) go through heating and cooling processes, thereby measuring the average directional magnetizations at different temperatures.

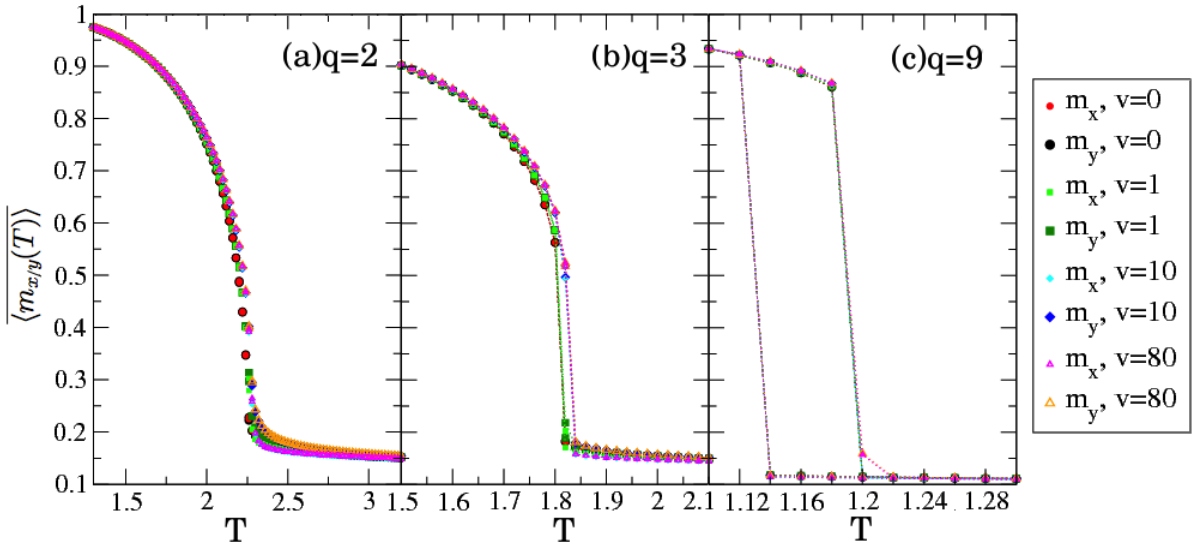

Figure 4.20: Directional surface magnetizations ($\overline{\langle m_x(T)\rangle}$ and $\overline{\langle m_y(T)\rangle}$) of the two-block systems ($W = L = 2H = 40$) with $q = 2$, $q = 3$, $q = 9$, $\kappa_f = 1$ and $v = 0, 1, 10, 80$. The data result from an average over 16 independent runs. At each temperature, 20000 (for q =2 or 3)/40000 (for $q = 9$) MCS are discarded before taking the average over the next 5000 MCS. Error bars are smaller than or of the same order as the symbol sizes.

The data in Fig.4.20 show that the curves for $\overline{\langle m_x(T)\rangle}$ and $\overline{\langle m_y(T)\rangle}$ are overlapping in each case, indicating that the directional surface magnetization in x and y directions are very similar. Detailed comparison of $\overline{\langle m_x(T)\rangle}$ and $\overline{\langle m_y(T)\rangle}$ for the q systems shows that the system changes from a *homogeneous state* at low temperatures to a *weak anisotropy state* at larger temperatures close to T_c. In contrast, the data for the $q = 9$ system shows that the system changes from a *homogeneous state* of complete order at low temperatures

to another *homogeneous state* of complete disorder at larger temperatures. In general, the larger the q values are, the more homogeneous are the contacting surfaces when T is close to T_c.

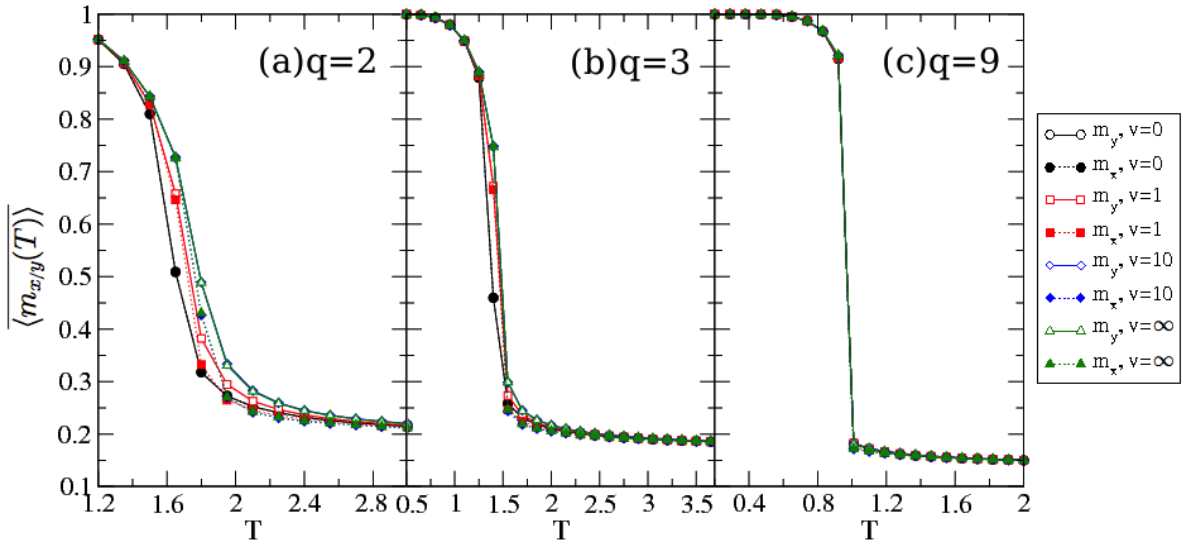

Figure 4.21: Directional surface magnetizations ($\overline{\langle m_x(T)\rangle}$ and $\overline{\langle m_y(T)\rangle}$) of the two-plane systems ($W = L = 20$) with $q = 2$, $q = 3$, $q = 9$, $\kappa_f = 1$ and $v = 0, 1, 10$ and ∞. Each curve is obtained in a heating process. At each temperature, 20000 (for $q = 2$ or 3)/30000 (for $q = 9$) Monte Carlo steps are discarded before taking the average over the next 20000 (for $q = 2or3$)/30000 (for $q = 9$) steps. Finally, data from 16 independent runs are averaged for plotting the curves. Error bars are smaller than the size of the symbols.

We also calculated the average directional magnetizations for the two-plane systems in the weak coupling regime, see Fig.4.21. Here we fix the system size to be $W = L = 20$. The curves in Fig.4.21 show the heating process of systems starting from a pure state at low temperature. From Fig.4.21(a) one can see that the directional magnetizations are larger when v is larger. (To simulate the Potts system with infinite relative velocity, we rewire the couplings on the contact surfaces randomly in each step if the y coordinate of the sites from the two surfaces share the same value. See Fig.4.14.) We also find that for

$q = 2$ systems the values of $\overline{\langle m_y(T)\rangle}$ are consistently larger than the values of $\overline{\langle m_x(T)\rangle}$. These two phenomena are less obvious in the $q = 3$ system and not visible in the $q = 9$ systems as shown in Fig.4.21(b) and Fig.4.21(c).

Phase Transition in the Medium Interfacial Coupling Regime

In the weak interfacial coupling regime, we noticed an increase of the transition temperature when the coupling strength between the two relatively moving blocks increases to 1, see Fig.4.18. Accordingly, we expect that there are also shifts of that temperature if we further increase the value of κ_f. The surface magnetization hysteresis curves for systems with $q = 2, 3, 9$, $v = 10$, and $\kappa_f = 2, 3, 4, 5$, are presented in Fig.4.22. It is obvious from

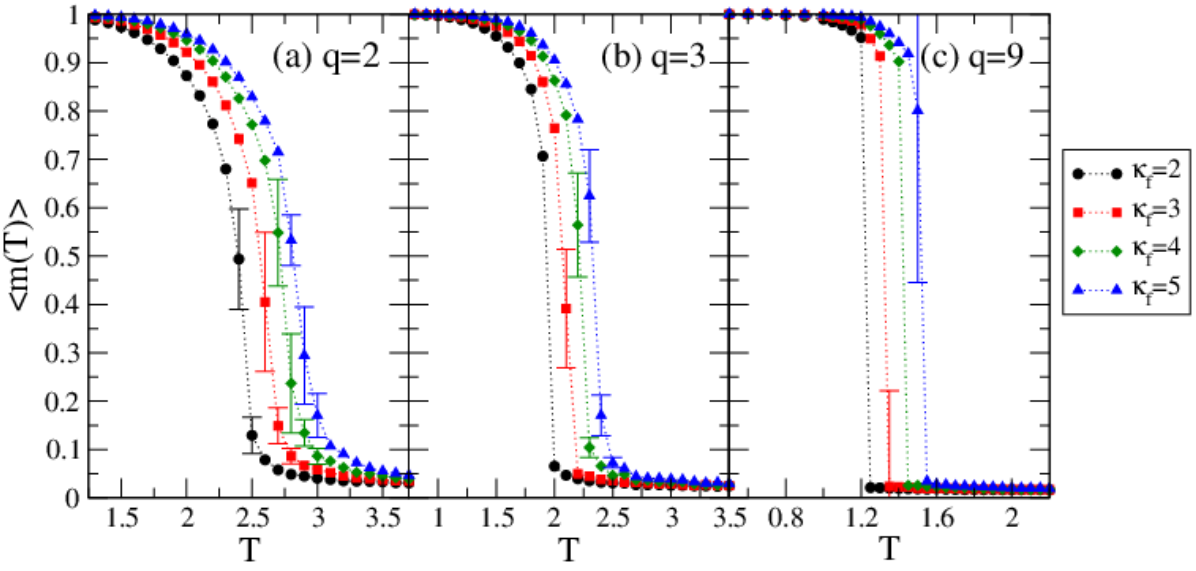

Figure 4.22: Surface magnetization curves of $\langle m(T)\rangle$ in different two-block systems ($W = L = 2H = 40$) with $v = 10$ and $\kappa_f = 2, 3, 4, 5$. The data for systems with $q = 2, 3$ and 9 are shown in panels (a), (b) and (c). At each temperature, the data is an average over 1000 MCS after a relaxation of 5000 (for q=2/3) or 10000 (for q=9) MCS, with an additional average over 16 independent runs. Errors smaller than 0.01 are not shown.

Fig.4.22 that for systems with $q = 2, 3$ and 9, with non-zero v and $\kappa_f > 1$, an increase of κ_f results in an increase of the phase transition temperature.

Since we expect to have heterogeneous magnetization on the contacting surfaces in the moving systems for larger κ_f, we also calculated the average directional surface magnetization in systems with $q = 2, 3, 9$, $\kappa_f = 5$ and $v = 0, 1, 10, 80$, see Fig.4.23. We find that

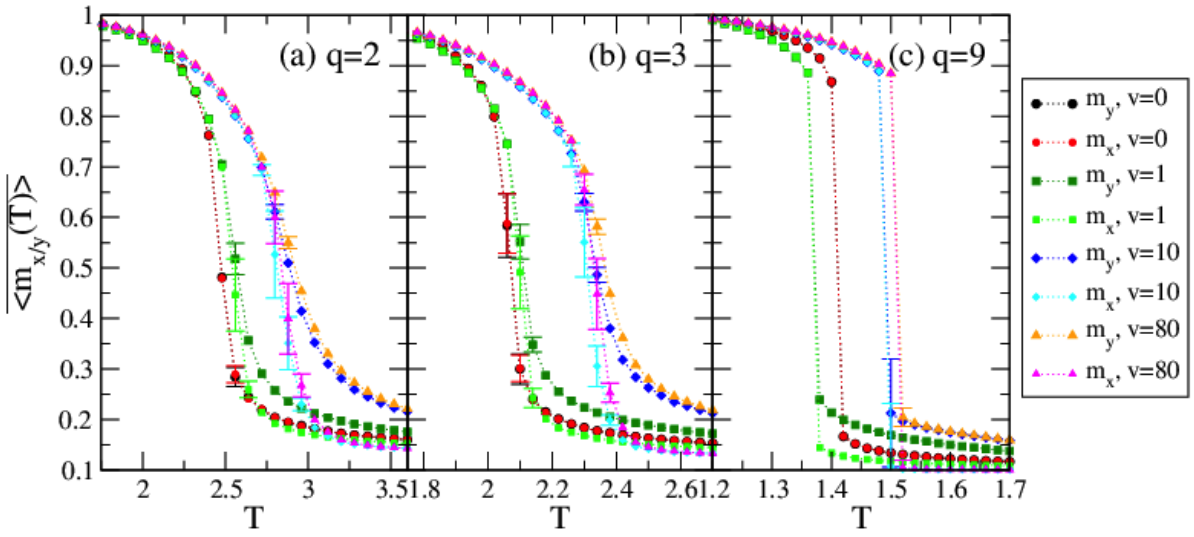

Figure 4.23: Directional surface magnetizations ($\overline{\langle m_x(T)\rangle}$ and $\overline{\langle m_y(T)\rangle}$) of systems ($W = L = 2H = 40$) with $q = 2$, $q = 3$, $q = 9$, $\kappa_f = 5$ and $v = 0, 1, 10, 80$. The data result from an average over 16 independent runs. At each temperature T, 20000 (for $q = 2$ or 3)/40000 (for $q = 9$) MCS are discarded before taking an average over the next 5000 steps. Errors smaller than 0.01 are not shown.

in systems with $\kappa_f = 5$ $\overline{\langle m_x(T)\rangle}$ and $\overline{\langle m_y(T)\rangle}$ behave differently when $v > 1$. Indeed for all three cases $q = 2, 3$ and 9, $\overline{\langle m_x(T)\rangle}$ is considerably smaller than $\overline{\langle m_y(T)\rangle}$. In general, in the medium interfacial coupling regime, small moving velocities (such as $v = 1$) result in *weak anisotropy states* around the phase transition temperature, whereas larger moving velocities (such as $v = 10$ and 80) result in *strong anisotropy states*.

Finally, Fig.4.24 shows the average directional surface magnetizations of the two-plane

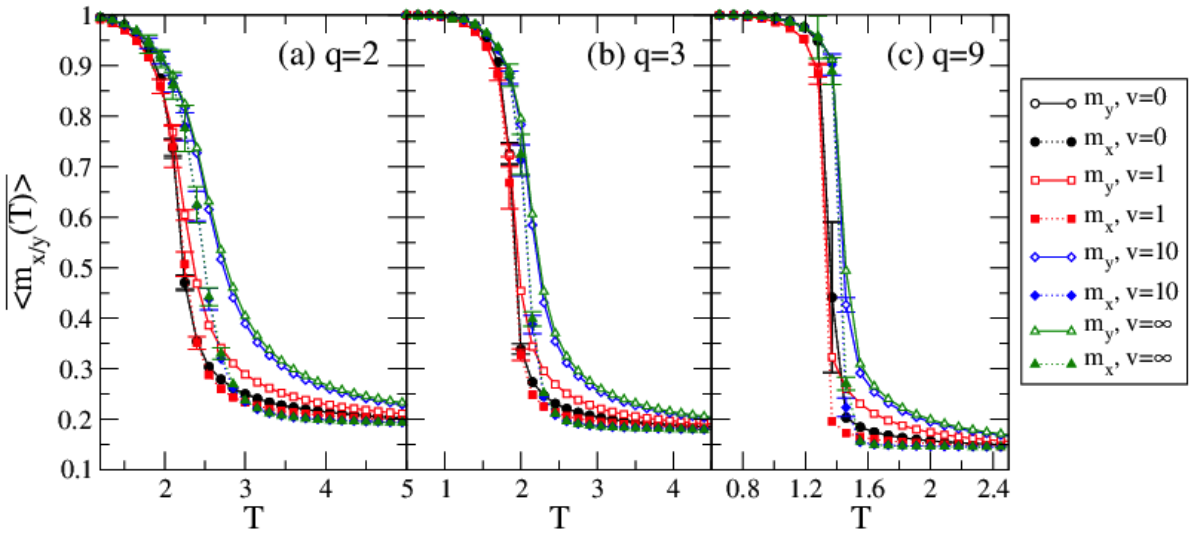

Figure 4.24: Directional surface magnetizations ($\overline{\langle m_x(T)\rangle}$ and $\overline{\langle m_y(T)\rangle}$) of the two-plane systems ($W = L = 20$) for $q = 2$, $q = 3$, $q = 9$, $\kappa_f = 5$ and $v = 0, 1, 10$ and ∞. Each curve is obtained in a heating process. At each temperature, 20000 (for $q = 2$ or 3)/30000 (for $q = 9$) Monte Carlo steps are discarded before taking the average over the next 20000 (for $q = 2$ or 3)/30000 (for $q = 9$) steps. Finally, data from 16 runs are averaged for obtaining these curves. Errors smaller than 0.01 are not shown.

systems during the heating process. Here, κ_f is also set to 5. All the phenomena found in Fig.4.23 are also found in Fig.4.24. In comparison, the average directional surface magnetizations in the two-plane systems have smaller phase transition temperatures compared to their two-block counterparts, which results from the different geometries of the two models.

Phase Transition in the Strong Interfacial Coupling Regime

Fig.4.25 shows $\overline{\langle m_x(T)\rangle}$ and $\overline{\langle m_y(T)\rangle}$ for the two-block systems with $q = 2, 3, 9$, $\kappa_f = 1, 3, 5, 6, 7, 9$ and $v = 10$. From careful observation of the data, we find that the phase

transition temperatures of the $q = 2, 3$ and 9 systems saturate when κ_f reaches 6. Therefore, we categorize a system into the strong interfacial coupling regime once κ_f reaches 6.

Another quantity of interest is the specific heat of the non-equilibrium systems, which corresponds to the specific heat of the equilibrium counterparts. The expression for the specific heat is given by:

$$C(T_i) = \frac{1}{2LWH}\frac{\partial E}{\partial T} = \frac{E(T_i) - E(T_{i-1})}{2LWH \times (T_i - T_{i-1})} \tag{4.37}$$

In the following, we show the numerical data of the specific heat for systems with $q = 2, 3, 9$, $\kappa_f = 1, 5, 9$ and $L = W = 4H = 80$, see Fig.4.26.

In each system with weak interfacial coupling ($\kappa_f = 1$), we observe a single pronounced peak. This means, for a finite system in the weak interfacial coupling regime, the surface phase transition happens at the same temperature as the bulk phase transition. In each system with a medium or strong coupling ($\kappa_f = 5, 9$), we observe two peaks (see the red curves in Fig.4.26). In each curve, the peak at a lower temperature corresponds to the phase transition in the bulk, whereas the peak at the higher temperature corresponds to the phase transition on the contacting surfaces where magnetic friction happens. Thus, we confirm again that for a finite system in the medium or strong interfacial coupling regime, the surface phase transition happens at a higher temperature compared to the corresponding bulk phase transition.

In addition, we studied the directional magnetization of the ($q = 2, 3, 9$) systems with different driving velocities ($v = 0, 1, 10, 80$) and strong interfacial couplings ($\kappa_f = 9$), see Fig.4.27. Unlike what is observed in Fig.4.23, we find that the $\overline{\langle m_x(T)\rangle}$ value drops abruptly to zero when the temperature is still low (at $T \approx 2.00$ for $q = 2$, or at $T \approx 1.15$ for $q = 3$), whereas $\overline{\langle m_y(T)\rangle}$decreases slowly with temperature.

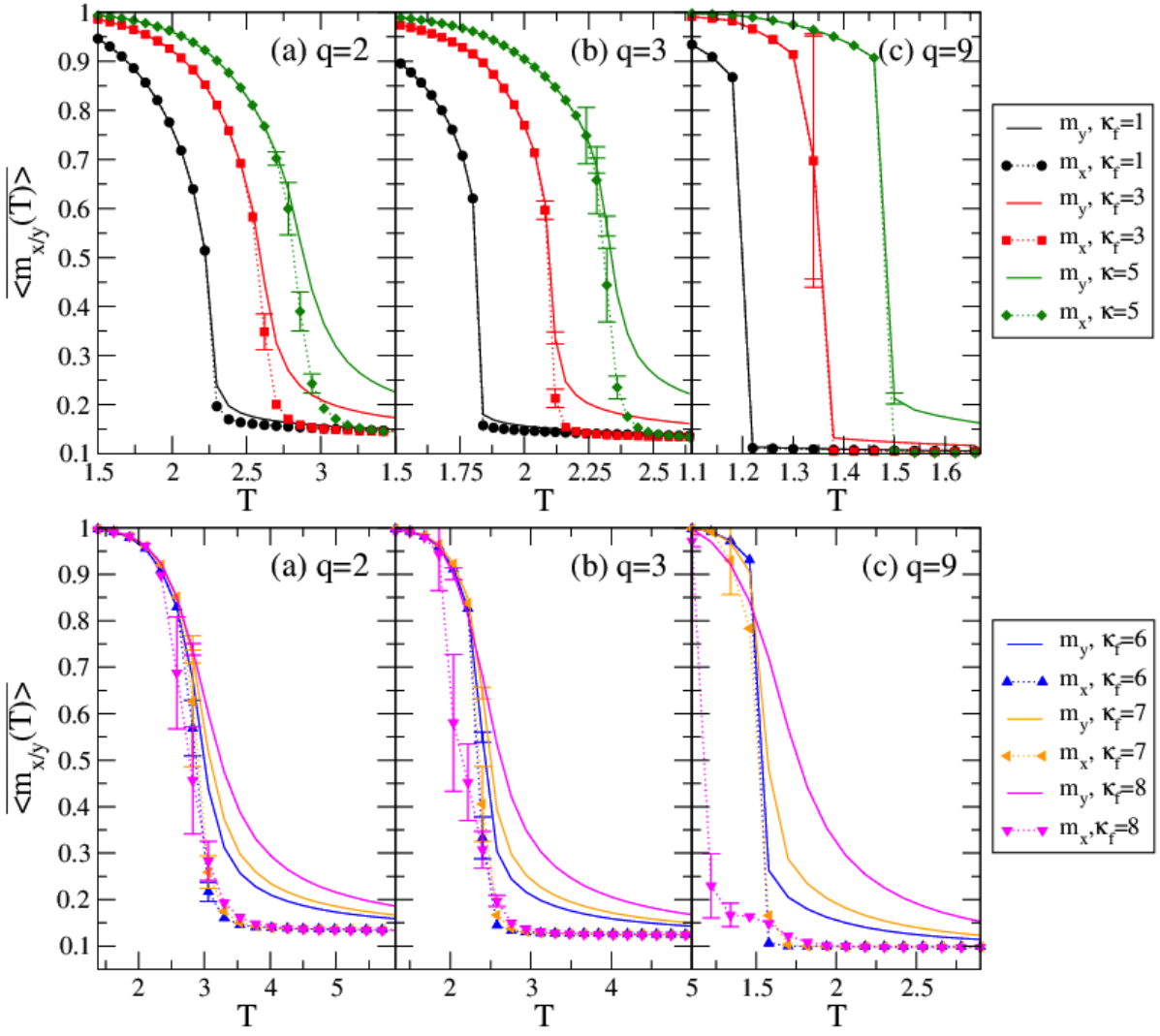

Figure 4.25: Directional surface magnetizations ($\overline{\langle m_x(T)\rangle}$ and $\overline{\langle m_y(T)\rangle}$) of systems ($W = L = 2H = 40$) with $q = 2, 3, 9$, $\kappa_f = 1, 3, 5, 6, 7, 9$ and $v = 10$. Each curve is an average of 16 independent runs. At each temperature T, 20000 (for q =2 or 3)/40000 (for $q = 9$) Monte Carlo steps are discarded before taking the average over the next 5000 steps. Errors smaller than 0.01 are not shown.

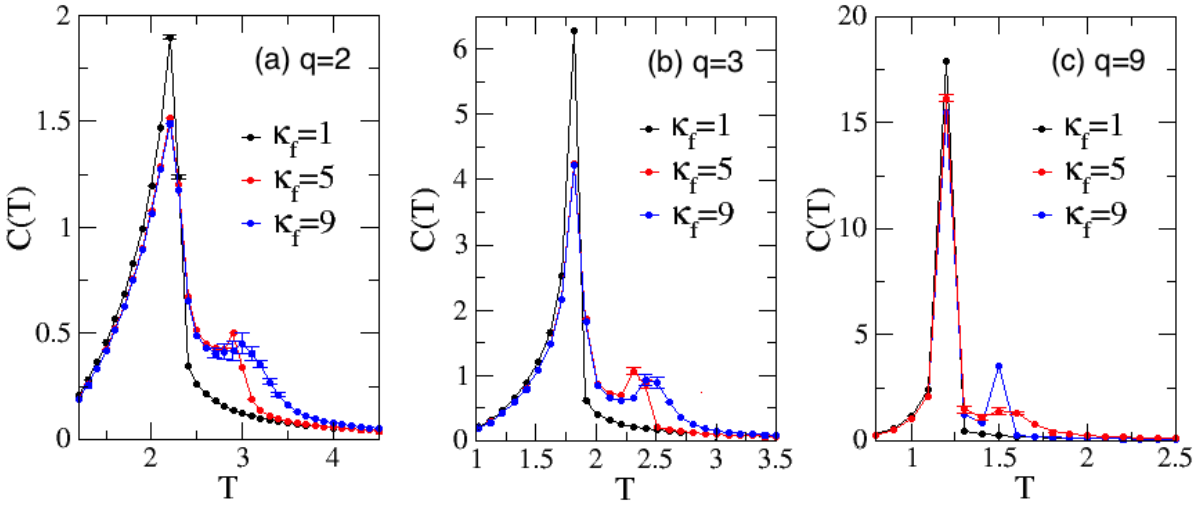

Figure 4.26: Specific heat of the two-block systems with size of $L = W = 80$, $H = 20$, and $v = 10$. The data is averaged over 5000 MCSs after 20000 (for q=2/3) or 40000 (for q=9) steps of relaxation, which is followed by an average over 16 runs.

We understand the disparity of the directional surface magnetizations as a result of finite size effects. To learn how the finite size effects influence the anisotropic behavior on the contacting surfaces, we run simulations of heating processes of $q = 2, 3$ and 9 systems with different aspect ratios L/W. In all the two-block systems we kept $W = H = 20$, while changing L from 20 to 160. Typical data are shown in Fig.4.28.

From Fig.4.28(a) and Fig.4.28(b) we find that there is a big difference between the values of the corresponding $\overline{\langle m_y(T)\rangle}$ and $\overline{\langle m_x(T)\rangle}$ in systems with $L = 20$ ($L/W = 1$), indicating the existence of the *strong anisotropy states*. When L increases to 40 ($L/W = 2$) and 80 ($L/W = 4$), the difference becomes smaller, indicating the existence of the *weak anisotropy states*. If we further increase L to 160, we find that the curves of $\overline{\langle m_y(T)\rangle}$ and $\overline{\langle m_x(T)\rangle}$ overlap nicely when the system temperature is in the vicinity of the phase transition temperature. The data for $q = 3$ show similar surface phenomena as observed in the $q = 2$ system, see Fig.4.28(b).

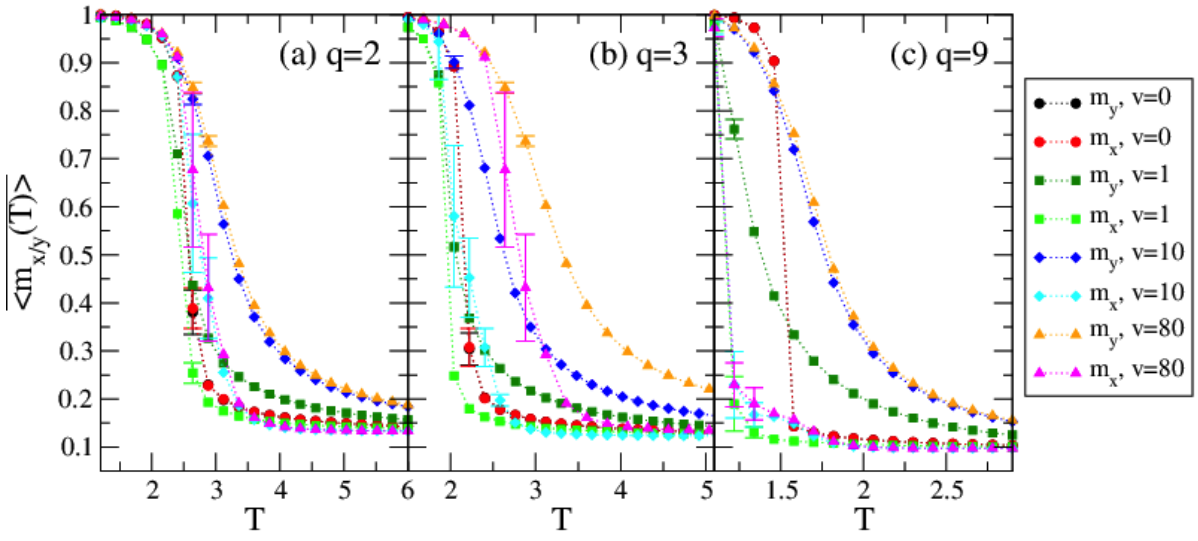

Figure 4.27: Directional surface magnetizations ($\overline{\langle m_x(T)\rangle}$ and $\overline{\langle m_y(T)\rangle}$) of systems ($W = L = 2H = 40$) with $q = 2$, $q = 3$, $q = 9$, $\kappa_f = 9$ and $v = 0, 1, 10, 80$. The data result from an average of 16 independent runs. At each temperature, 20000 (for $q = 2$ or 3)/40000 (for $q = 9$) MCS are discarded before taking the average over the next 5000 steps. Errors smaller than 0.01 are not shown.

In Fig.4.28(c), we show the directional surface magnetization curves for the heating processes in systems with $q = 9$. When $L = 20, 40$ and 80 ($L/W = 1, 2$ and 4), the data for $\overline{\langle m_x(T)\rangle}$ seem to indicate that the surface magnetization in x direction goes through a discontinuous phase transition at T=1.22, whereas the data for $\overline{\langle m_y(T)\rangle}$ indicate that the directional surface magnetization in y direction undergoes continuous phase transition. It is also obvious from the data of $\overline{\langle m_y(T)\rangle}$ that systems with larger aspect ratio yield smaller directional surface magnetizations in y direction. When L reaches 160, we find from the $\overline{\langle m_x(T)\rangle}$ curve that its transition temperature is greatly increased. In addition, we find that the transition of the magnetization in y direction becomes discontinuous. As a result, the hysteresis curves of the surface magnetizations in x and y directions overlap. In our simulations, the phase transitions of the two directional magnetizations become discontinuous and they share the same phase transition temperature (at T =1.52). This

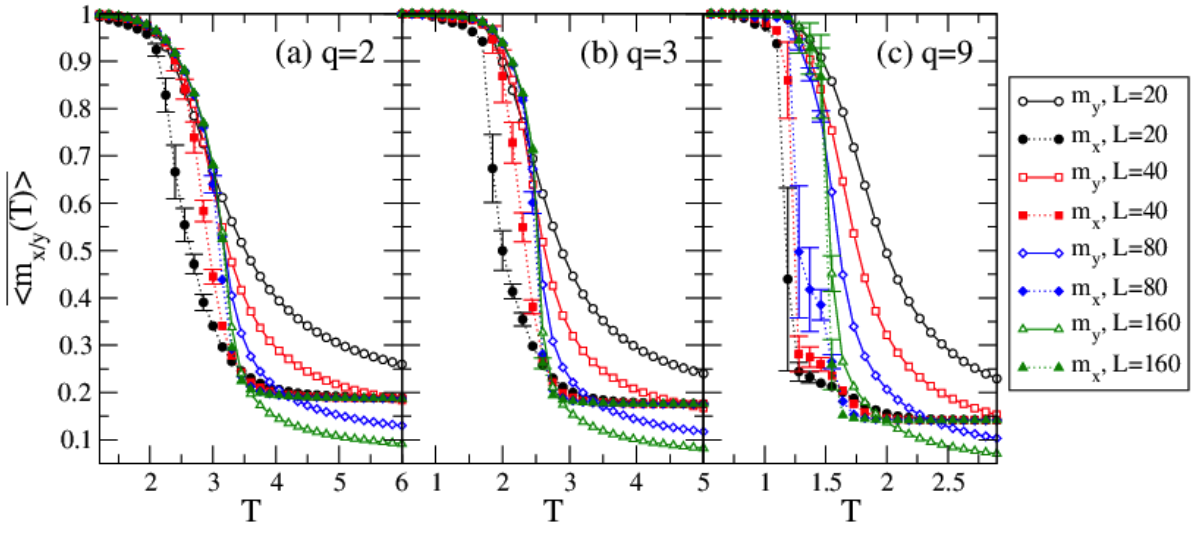

Figure 4.28: Directional surface magnetization (on the interface layer $z = 1$) of systems with $q = 2, 3, 9$, $\kappa_f = 9$, and $v = 10$. In these systems, $W = H = 20$, and L ranges from 20 to 160. Each curve shows the $\overline{\langle m_x(T)\rangle}$ or $\overline{\langle m_y(T)\rangle}$ during a heating process, and each data point is an average of 30 independent runs. (a) and (b) show the data for the $q = 2$ and $q = 3$ systems, where 40000 MCS are discarded before taking an average over another 40000 MCS. (c) shows the data for the $q = 9$ system, where 45000 MCS are discarded before taking an average over another 45000 MCS. Errors smaller than 0.01 are not shown.

phase transition temperature is the same as found in the counterpart system with v=0 (see the black and red dotted curves in Fig.4.27(c)).

In Fig.4.29, the average directional surface magnetization in the heating processes are plotted for the two-plane systems (with system size of $L = W = 20$). In this figure, we find that all the $q = 2, 3$ and 9 systems have their $\overline{\langle m_x(T)\rangle}$ curves undergo discontinuous phase transitions. Also, we find that the $\overline{\langle m_y(T)\rangle}$ curves (of the $v = 10$ systems) show continuous phase transitions like what is observed in the two-block systems, see Fig.4.27 and Fig.4.28. All these three systems show very different values for the x and y directional

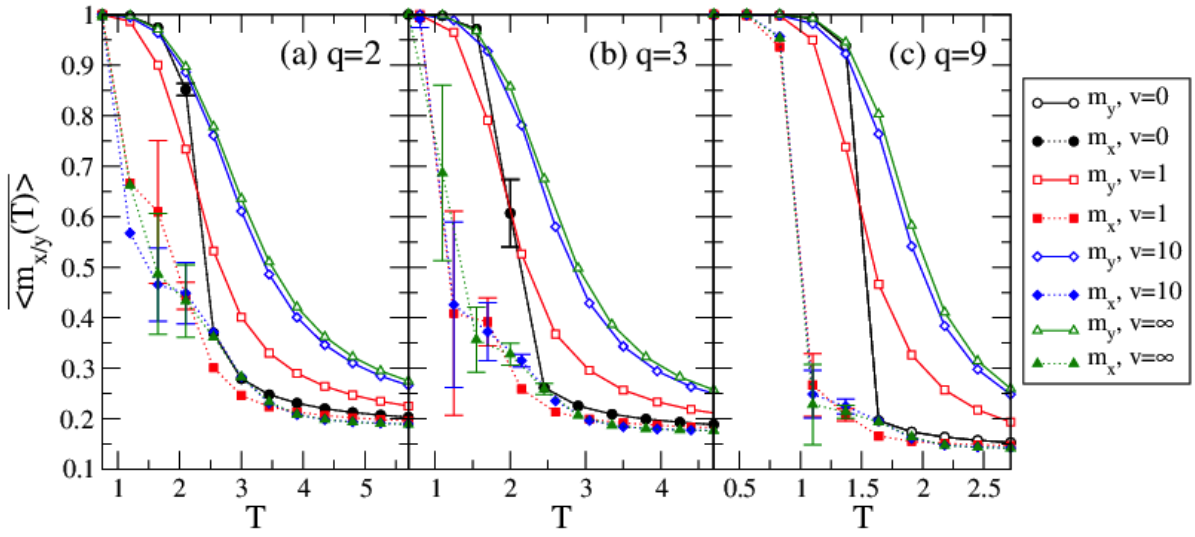

Figure 4.29: Directional surface magnetizations ($\overline{\langle m_x(T)\rangle}$ and $\overline{\langle m_y(T)\rangle}$) of the two-plane systems ($W = L = 20$) for $q = 2$, $q = 3$, $q = 9$, $\kappa_f = 9$ and $v = 0, 1, 10$ and ∞. Each curve is obtained in a heating process. At each temperature, 20000 (for $q = 2$ or 3)/30000 (for $q = 9$) Monte Carlo steps are discarded before taking the average over the next 20000 (for $q = 2$ or 3)/30000 (for $q = 9$) steps. Finally, data from 16 runs are averaged for obtaining these curves. Errors smaller than 0.01 are not shown.

surface magnetizations. In conclusion, the two-plane system with magnetic friction also relax into *strong anisotropy states* like the two-block systems, but with stronger anisotropy when given the same size of interfacial couplings.

Fig.4.30 and Fig.4.31 show snapshots of the two-block and two-plane systems with different aspect ratios $a = L/W$. All systems shown in these snapshots have the same width $W = 20$, the same driving velocity $v = 10$, the same coupling constant $\kappa_f = 9$, but different lengths L that range from 20 to 160, making the aspect ratio $a = 1, 2, 4$ and 8. It is not hard to see from both Fig.4.30 and Fig.4.31 that the smaller the aspect ratio is, the larger is the magnetization in the driving velocity (y direction). For example, when a is as small as 1 or 2, the finite size in the driving velocity direction cuts off the fluctuations

of the spin states in this same direction, resulting in larger values for $\overline{\langle m_y(T)\rangle}$. However, when a equals 8, the large system size in the driving direction starts to allow domains of different spin states to appear simultaneously in the driving direction. This explains why the dark green curve pairs in each of the $q = 2, 3$ and 9 plots of Fig.4.28 overlap exactly.

In addition, from Fig.4.30 and Fig.4.31 we find that both the two-block and the two-plane models show a certain degree of anisotropic magnetizations in temperatures that are above their respective equilibrium critical temperatures. Between these two models, the two-plane systems show relatively stronger anisotropy.

In general, we find very complicated anisotropic phase transition behaviors in the large interfacial coupling constant regime. We also find that this anisotropy is caused by the finite size of the system in the moving direction, and that it can be eliminated by changing the aspect ratio (L/W) of the 3D Potts system. In addition, we discovered that in the strong interfacial coupling regime the two-plane systems have an even stronger anisotropy in their contacting surfaces.

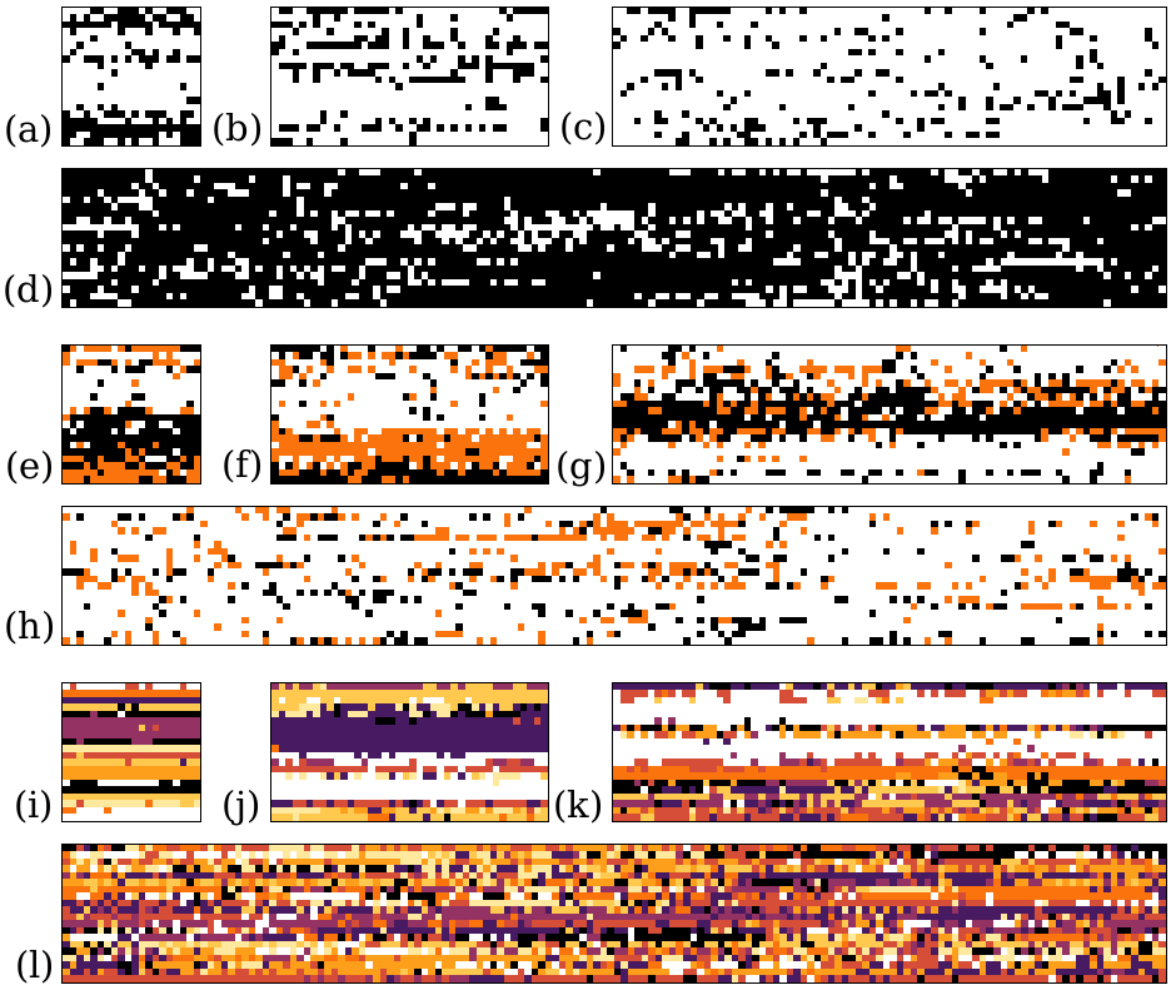

Figure 4.30: Snapshots of one of the connecting surfaces of the two-block systems with $W = 2H = 20$, $v = 10$, and $\kappa_f = 9$. For systems with $q = 2$ (T=3) [(a)-(d)] and 3 (T=2.45) [(e)-(h)] snapshots are taken after 80000 Monte Carlo steps, whereas for systems with $q = 9$ (T=1.55) [(i)-(l)] snapshots are taken after 90000 Monte Carlo steps. In (a), (e) and (d), $L = 20$; in (b), (f) and (j), $L = 40$; in (c), (g) and (k), $L = 80$ and in (d), (h) and (l), $L = 160$.

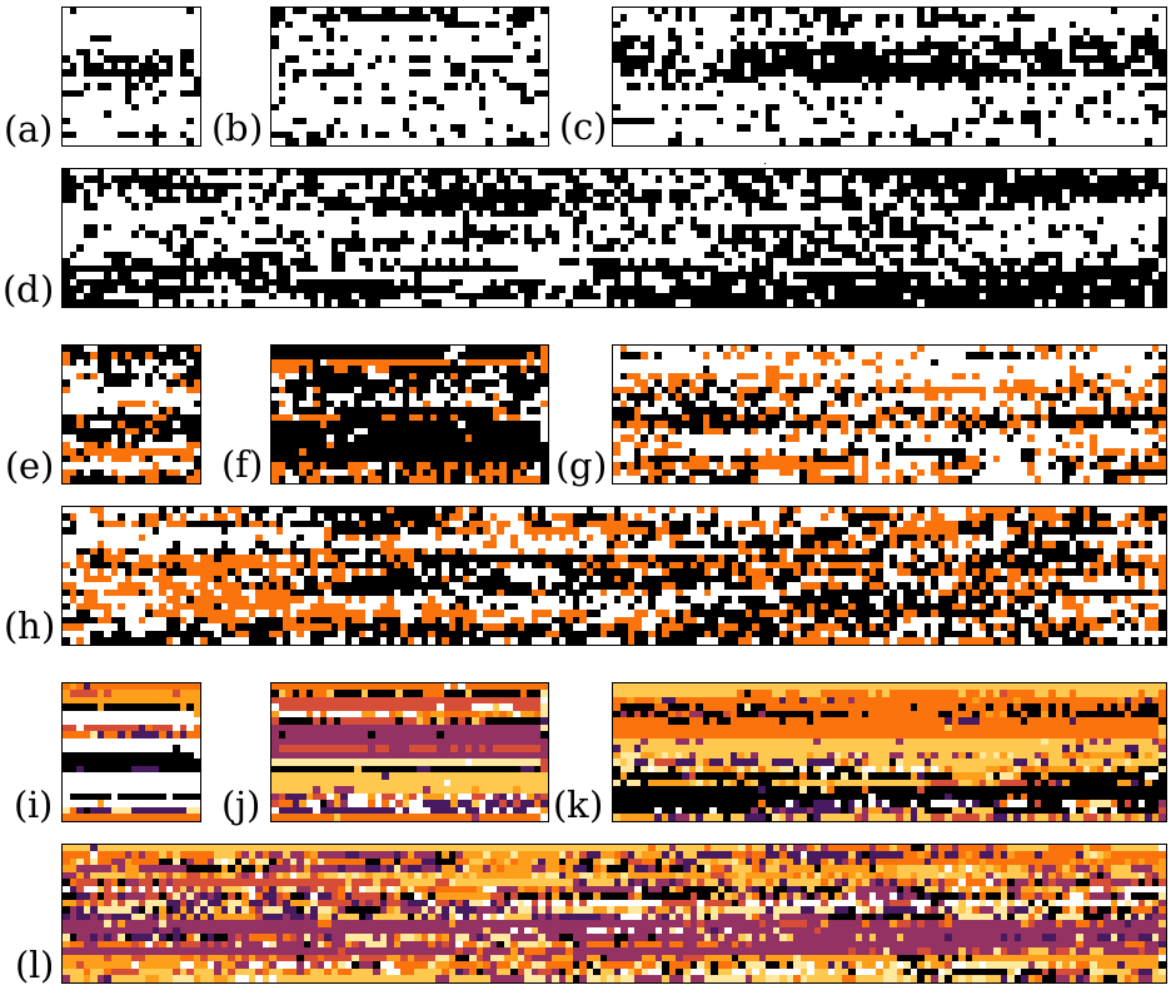

Figure 4.31: Snapshots of one of the connecting surfaces of the two-plane systems with $W = 20$, $v = 10$, and $\kappa_f = 9$. For systems with $q = 2$ (T=3) [(a)-(d)] and 3 (T=2.45) [(e)-(h)] snapshots are taken after 40000 Monte Carlo steps, whereas for systems with $q = 9$ (T=1.55) [(i)-(l)] snapshots are taken after 60000 Monte Carlo steps. In (a), (e) and (d), $L = 20$; in (b), (f) and (j), $L = 40$; in (c), (g) and (k), $L = 80$ and in (d), (h) and (l), $L = 160$.

4.2.4 Conclusion

We conclude by categorizing the two-block (and two-plane) Potts systems into three regimes: (1) the weak interfacial coupling regime ($\kappa_f \leq 1$), where surface phase transition temperatures hardly change in the finite systems with $q = 2, 3$ and 9, whereas the effective exponent β_{eff} is slightly decreased; (2) the medium interfacial coupling regime ($1 < \kappa_f < 6$), where surface phase transition temperature is increased in the finite systems with $q = 2, 3$ and 9; and (3) the strong interfacial coupling regime ($\kappa_f \geq 6$), where *strong anisotropy states* are observed in all the $L = W < \infty$ systems. Further analysis shows that both the observed *weak* and *strong anisotropy states* are results of finite-size effect and that these anisotropy states transit into *homogenous states* if the aspect ratio L/W is large (L is the system size in the driving direction and W is the system size perpendicular to the driving direction).

4.3 Magnetic Friction between a Wedge and a Block

At the beginning of this chapter, the critical phenomena of the free surfaces at discontinuous bulk transitions were discussed, followed by a careful analysis of the surface behavior of Potts systems with magnetic friction. In the latter case, strong spin anisotropy is discovered in the contacting surfaces of both the two-block and two-plane systems. In this section, instead of studying magnetic friction induced by the full contact of two surfaces, I will investigate three-dimensional Potts systems where magnetic friction takes place between a wedge and a block.

4.3.1 Model

One of the simplest three-dimensional Potts models that involves local surface contact is the *wedge-block Potts model*. This model consists of two three-dimensional Potts lattices: a wedge-shaped lattice (wedge) on the top (which can be thought to model a magnetic scanning tip), and a cubic lattice (block) at the bottom.

The schematic picture of these three-dimensional Potts systems is shown in Fig.4.32. The width of the tip of the wedge is T, the thickness of the tip is A, and the height of the wedge is h. The two lateral surfaces of the wedge make an angle of 45 degrees with the horizontal surface. In addition, the lower block has a length of L, a width of W and a height of H. In our simulations we set $W = T$. Also, periodic boundary conditions are applied in the x direction of the wedge, and in the x and y direction of the block. For all the other surfaces we have open boundary conditions.

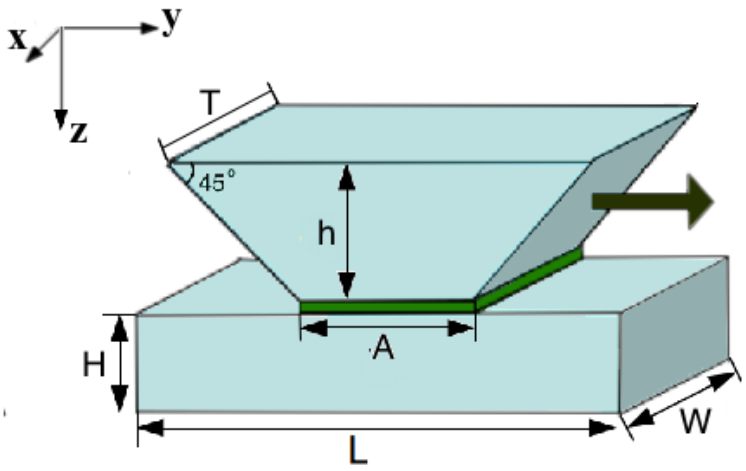

Figure 4.32: A schematic picture of the three-dimensional wedge-block Potts model. The system is made up of a three-dimensional wedge-shaped lattice at the top and a three-dimensional block at the bottom, with the bottom of the upper lattice sliding on the top of the lower lattice. The direction of the relative motion is the y direction.

To realize the relative movement between the two lattices, we first couple the upper wedge and lower block together, with a coupling strength κ_f. Then, we move the upper block in y direction at regular time intervals.

Specifically, we fix the size of the lower block such that $L = W = 2H = 40$ and the size of the wedge such that $T = 2h = 40$. In addition, as shown in Fig.4.32, we study wedge-block systems with different contacting areas $T \times A$ by changing the thickness of the wedge tip (A). We expect to observe a change of the magnetic behaviors of the contacting regions when changing the size of the wedge tip.

4.3.2 The Surface Properties

To study the surface behavior of the wedge-block Potts system, we investigate the surface magnetization, the magnetization correlation function, as well as the directional surface magnetizations of the contacting surfaces. The expressions for the surface magnetization and the directional surface magnetizations are similar to the ones given in Eq.(4.33), Eq.(4.34) and Eq.(4.35). The expression for the surface magnetization correlation function takes the following form:

$$k_B T \chi(z,T) = \frac{1}{N(z)}(< N_m(z,T)^2 > - < N_m(z,T) >^2), \tag{4.38}$$

where $z = z_s$ and $z = z'_s$, label the contacting surfaces. Here $N(z)$ is the total number of sites in the z^{th} layer, and $N_m(z,T)$ is the number of sites that take the dominant state in the z^{th} layer at temperature T.

The Surface Magnetization and the Magnetization Correlation Function of the Wedge-block Systems.

In the following, we show our data for the surface magnetization and the magnetization correlation function of the wedge-block systems. The data for the $q = 2$ systems are shown in Fig.4.33 - Fig.4.36, and the data for the $q = 9$ systems are shown in Fig.4.37. In these figures, each data is obtained as an average of 16 runs, and in each run an average is made over 5,000 MCSs after a relaxation of 20,000 MCSs. The size of the tip of the wedge is varied such that $A = 1, 6$ and 11. Plots are made for systems with $v = 0/80$ and $\kappa_f = 1/9$.

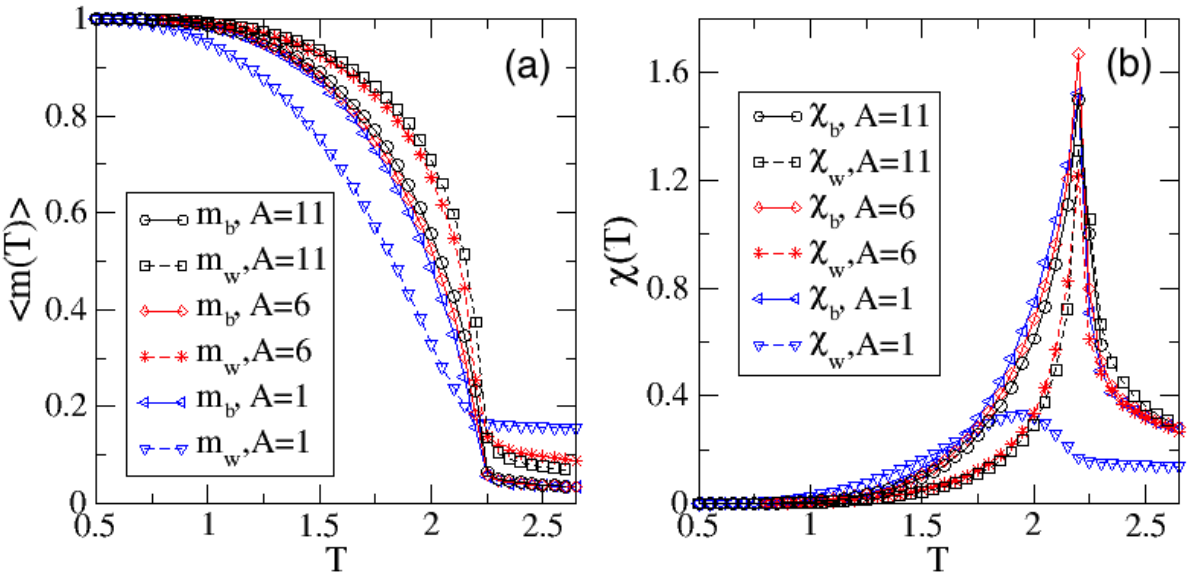

Figure 4.33: Panel (a) shows the average magnetization on the contacting surfaces (w=wedge, b=block), whereas panel (b) shows the values of the magnetization correlation function on the contacting surfaces. The system parameters are: $q = 2, L = W = 80, h = H = 20, v = 0, \kappa_f = 1, t_{relax} = 20000$ and $t_{total} = 25000$.

In Fig.4.33(a)(b), we show our data for the surface magnetization and magnetization correlation function of the $q = 2, \kappa_f = 1$ systems with no relative movement. (Here

m_b/X_b represents the surface magnetization/magnetization correlation function of the top surface of the block, and m_w/X_w represents the surface magnetization/magnetization correlation function of the bottom surface of the wedge.) From Fig.4.33(a), we find that when $v = 0, \kappa_f = 1$, the properties of the tip of the wedge can be very different from those of the top surface of the lower block. Compare the blue curves for the $A = 1$ systems, we see that the dashed blue curve for m_w has smaller curvature than the solid blue curve for m_b. For the $A = 6$ (11) systems (see the red (black) curves), the dashed red (black) curve for m_w has larger curvature than the solid red (black) curve for m_b.

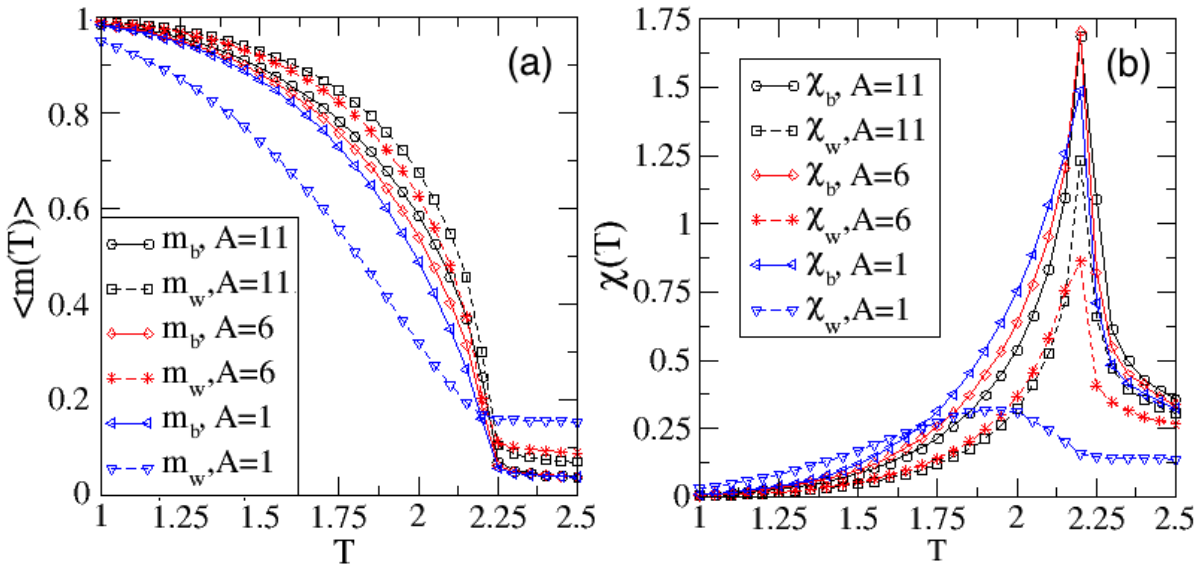

Figure 4.34: Panel (a) shows the average magnetization on the contacting surfaces, whereas panel (b) shows the values of the magnetization correlation function on the contacting surfaces. The system parameters are: $q = 2, L = W = 80, h = H = 20, v = 80, \kappa_f = 1, t_{relax} = 20000$ and $t_{total} = 25000$.

If the velocity of relative movement between the two Potts lattices is $v = 80$, minor changes can be found in the magnetization and magnetization correlation function curves. For example in Fig.4.34(a), the m_b and m_w values become closer to each other in the $A = 6$ and $A = 11$ systems.

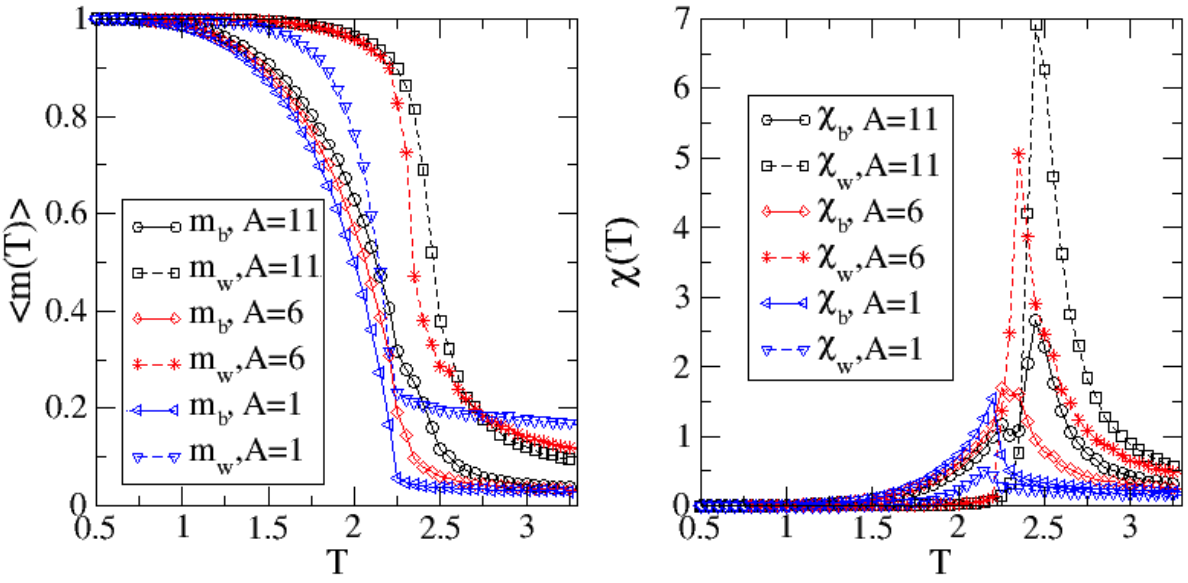

Figure 4.35: Panel (a) shows the average magnetization on the contacting surfaces, whereas panel (b) shows the values of the magnetization correlation function on the contacting surfaces. The system parameters are: $q = 2, L = W = 80, h = H = 20, v = 0, \kappa_f = 9, t_{relax} = 20000$ and $t_{total} = 25000$.

Fig.4.35(a)(b) show the data for the non-moving $q = 2, \kappa_f = 9$ systems. From Fig.4.35(a) we find that, if $v = 0$, the bottom surface of the wedge always has larger magnetization than the upper surface of the block. If one looks at the black solid curve and red solid curve in Fig.4.35(a) carefully, one can notice that the first drop of m_b is followed by a second drop at a larger temperature. We understand this as a result of strong interfacial couplings between the two contacting surfaces. This phenomenon is not so obvious in the $A = 1$ systems, where the size of the contacting area is small. In the $A = 1$ system, the χ_w peaks at 2.15 and the χ_b peaks at 2.20. In the $A = 6$ system, the χ_w peaks at 2.30, whereas χ_b shows two maxima, one peaks at 2.25, and the other one peaks at 2.30. In the $A = 11$ system, the χ_w peaks at 2.45 and the χ_b peaks at both 2.25 and 2.45.

In Fig.4.36(a)(b), where the data for the $q = 2, \kappa_f = 9, v = 10$ systems are shown, we

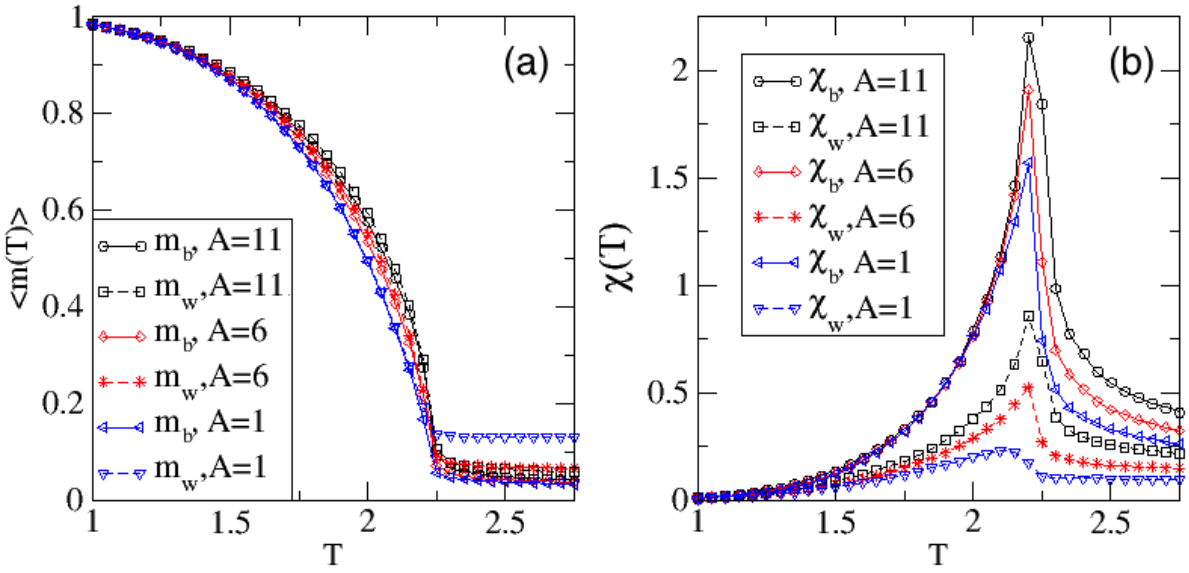

Figure 4.36: Panel (a) shows the average magnetization on the contacting surfaces, whereas panel (b) shows the values of the magnetization correlation function on the contacting surfaces. The system parameters are: $q = 2, L = W = 80, h = H = 20, v = 80, \kappa_f = 9, t_{relax} = 20000$ and $t_{total} = 25000$.

find that the surface behavior of the wedge tip and the block top are remarkably similar to each other. In Fig.4.36(a), the m_b and m_w curves for all the $A = 1, 6$ and 11 systems almost overlap. (The surface magnetizations of the $A = 11$ systems are slightly bigger than the ones of the $A = 6$ systems, which are slightly bigger than the ones of the $A = 1$ systems.) At the same time, Fig.4.36(b) indicates that the positions of the magnetization correlation function maxima are all very close to each other. For example, when $A = 11$, both χ_w and χ_b peaks at 2.20; when $A = 6$, both χ_w and χ_b also peaks at 2.20; when $A = 1$, χ_w peaks at 2.10 and χ_b peaks at 2.20.

The surface magnetization and surface magnetization correlation function data for the $q = 9$ systems show the same phenomena, see Fig.4.37. For example, in Fig.4.37(a), we find that for $v = 80$, $\kappa_f = 1$, the magnetizations of the wedge tip and block top show noticeable differences (compare the solid and dashed curves of each color). Yet, in

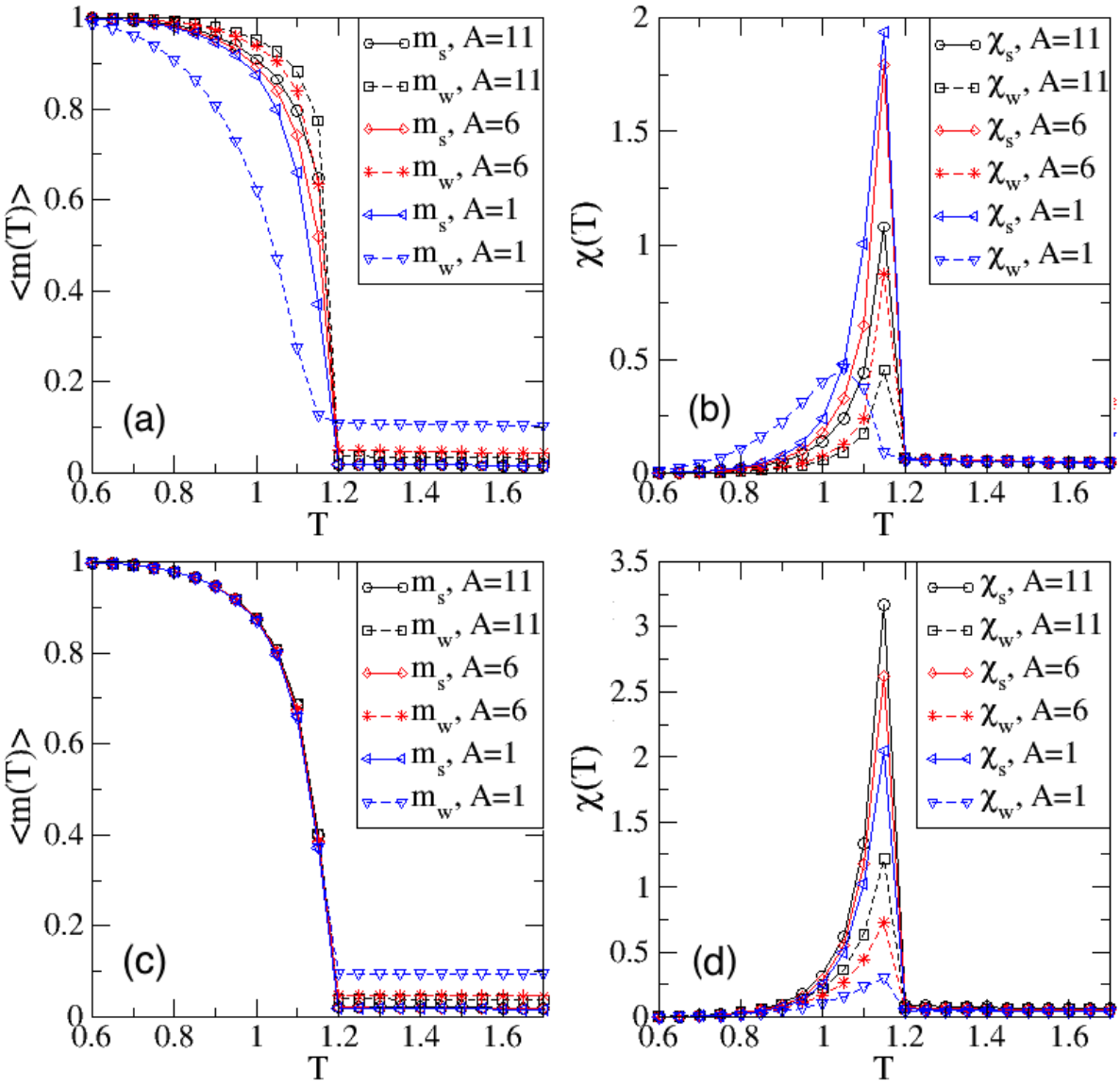

Figure 4.37: Panels (a) and (c) show the average magnetization on the contacting surfaces, whereas panels (b) and (d) show the magnetization correlation function on the contacting surfaces. The system parameters are: $q = 9, v = 80, L = W = 80, h = H = 20, t_{relax} = 20000$ and $t_{diff} = 5000$. In (a) and (b) $\kappa_f = 1$, whereas in (c) and (d) $\kappa_f = 9$.

Fig.4.37(d) we find that when $v = 80, \kappa_f = 9$, all the surface magnetization curves overlap with each other and all the surface magnetization correlation function curves peak at the same temperature $T = 1.15$.

To sum up, in the wedge systems with either small or large total number of states, we discovered that the finite size transition of the two contacting surfaces become very similar to each other in presence of strong interfacial couplings (this is especially true when the area of local contact is large).

4.3.3 The Local Surface Behaviors

In the wedge-block systems, the lower Potts block is only partially in contact with the upper tip, and we expect the magnetic behavior of the contacting surfaces to differ from place to place. To study the local surface behaviors, we introduce two new quantities, the *line magnetization* and the *line magnetization correlation function*. The mathematical expressions for these two parameters are as follows:

$$m(y, z, T) = (\frac{qN_m(y, z, T)}{W} - 1)/(q - 1) \tag{4.39}$$

$$k_B T\chi(y, z, T) = \frac{1}{N(y, z)}(\langle N_m(y, z, T)^2\rangle - \langle N_m(y, z, T)\rangle^2) \tag{4.40}$$

$N_m(y, z, T)$ in the above questions represents the number of the sites that are taking the dominant state in the line located at (y, z) at temperature T, and can be expressed as:

$$N_m(y, z, T) = \max(N_0(y, z, T), N_1(y, z, T), ..., N_{q-1}(y, z, T)). \tag{4.41}$$

It is not hard to see from the Eq.(4.39) and Eq.(4.40) that the line magnetization is the magnetization of a line of sites in x direction with fixed y, z and T, whereas the line

magnetization correlation function quantifies the magnetic fluctuation of sites in a line in x direction with the same values of y, z and T.

In our research, both the average line magnetization and the average line magnetization correlation function are numerically calculated through extensive Monte Carlo simulations. In the following, data for the wedge-block systems with weak and strong interfacial couplings ($\kappa_f = 1$ and 9) are shown and discussed.

The Line Magnetization

In this part, we discuss the average line magnetization for $q = 9$ systems with different coupling constants and different relative velocities. Since our purpose is to study the local magnetic properties of the contacting surfaces, we calculate the line magnetization at the bottom of the wedge as well as the line magnetization at the top surface of the lower block.

Fig.4.38 shows the average line magnetization data of the contacting layers as well as the fifth layers from the contacting layers of a $A = 6$ system with $\kappa_f = 1$ and $v = 0$ (Fig.4.38(a)(b)) and $v = 80$ (Fig.4.38(c)(d)). In Fig.4.38(a), data of the first and fifth layer from the bottom of the wedge lattice are displayed. The black curves show that the average line magnetizations of both the contacting layer and the inner layer are inhomogeneously distributed at temperature $T = 1.1$. In Fig.4.38(b) where the data for the lower block are displayed, we find that the line magnetizations on the surface, where the contact is taking place, show the same pattern as seen in Fig.4.38(a) (compare the black curves with circles). In the other places of the block surface where there are no interfacial couplings, we find the line magnetizations take much smaller values (around 0.66). In Fig.4.38(c)(d), we can see an obvious change of the line magnetizations due to the relative movement. When $v = 80$, the line magnetizations of the bottom layer of

the wedge take slightly smaller values (see the black curve with circles in Fig.4.38(c)), whereas the top layer of the block displays a uniform line magnetization.

Fig.4.39 gives information on the average magnetizations when the coupling between the two lattices is strong ($\kappa_f = 9$). In Fig.4.39(a)(b), where $v = 0$, we see that the lines of coupled sites take the value $\langle m(y, z, 1.1)\rangle = 1$ (see the black lines with circles). Interestingly, we also find the value $\langle m(y, z, 1.2)\rangle = 1$, in a system where $T = 1.2 > T_c(q = 9) \approx 1.15$ (see the red lines with circles where $y = 21, 22, 23, 24$). This means that the ordering temperature on the contacting area can be increased locally by increasing the coupling strength (from $\kappa_f = 1$ to $\kappa_f = 9$). When the upper wedge moves with $v = 80$, we find that the line magnetizations on the contracting area are brought back to values around 0.1 at the temperature $T = 1.2$ (see the red lines with circle in Fig.4.39(c)(d)). We also find that the line magnetizations on both contacting surfaces become uniform and take the same value, whereas the line magnetizations in the fifth layers have the same values as for $v = 0$. These phenomena tell us that the magnetic friction with large velocity and strong interfacial couplings significantly alters the magnetic behavior on the contacting surface. However, its influence on the magnetic behavior of the inner layers is negligible.

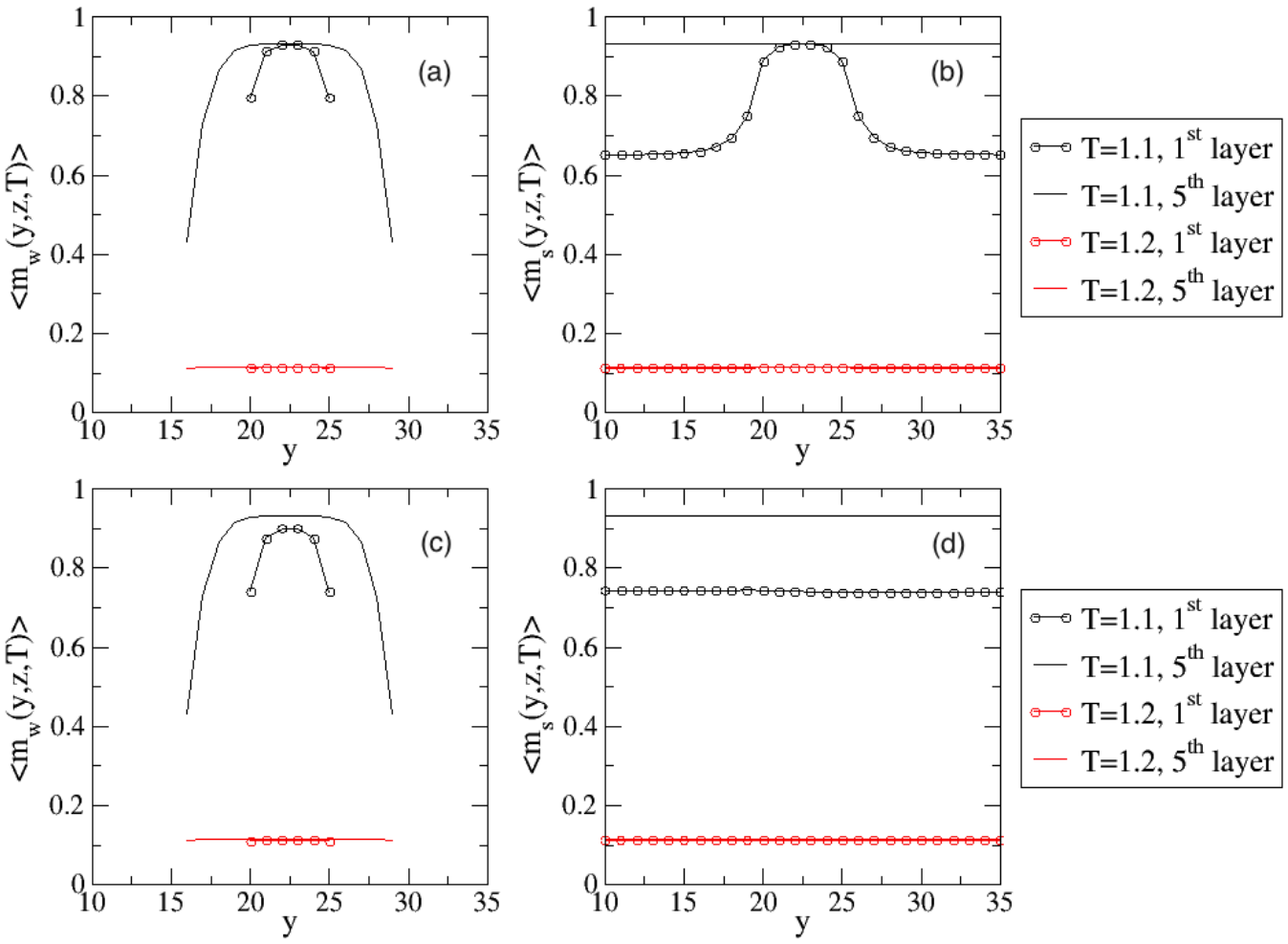

Figure 4.38: Panels (a) and (b) show the average line magnetizations of the wedge-block system with $v = 0$, whereas panels (c) and (d) show the average line magnetizations of the system with $v = 80$. Data for temperatures $T = 1.1$ and $T = 1.2$ are displayed. Panels (a) and (c) show the average line magnetizations of the first and the fifth layer from the bottom of the wedge lattice, whereas panels (b) and (d) show the average line magnetizations of the first and the fifth later from the top of the lower block lattice. Other system parameters are $q = 9$, $\kappa_f = 1$, $A = 6$, $L = W = 40$, $h = H = 20$, $t_{relax} = 20000$, $t_{run} = 25000$. Averages are obtained from 16 independent runs.

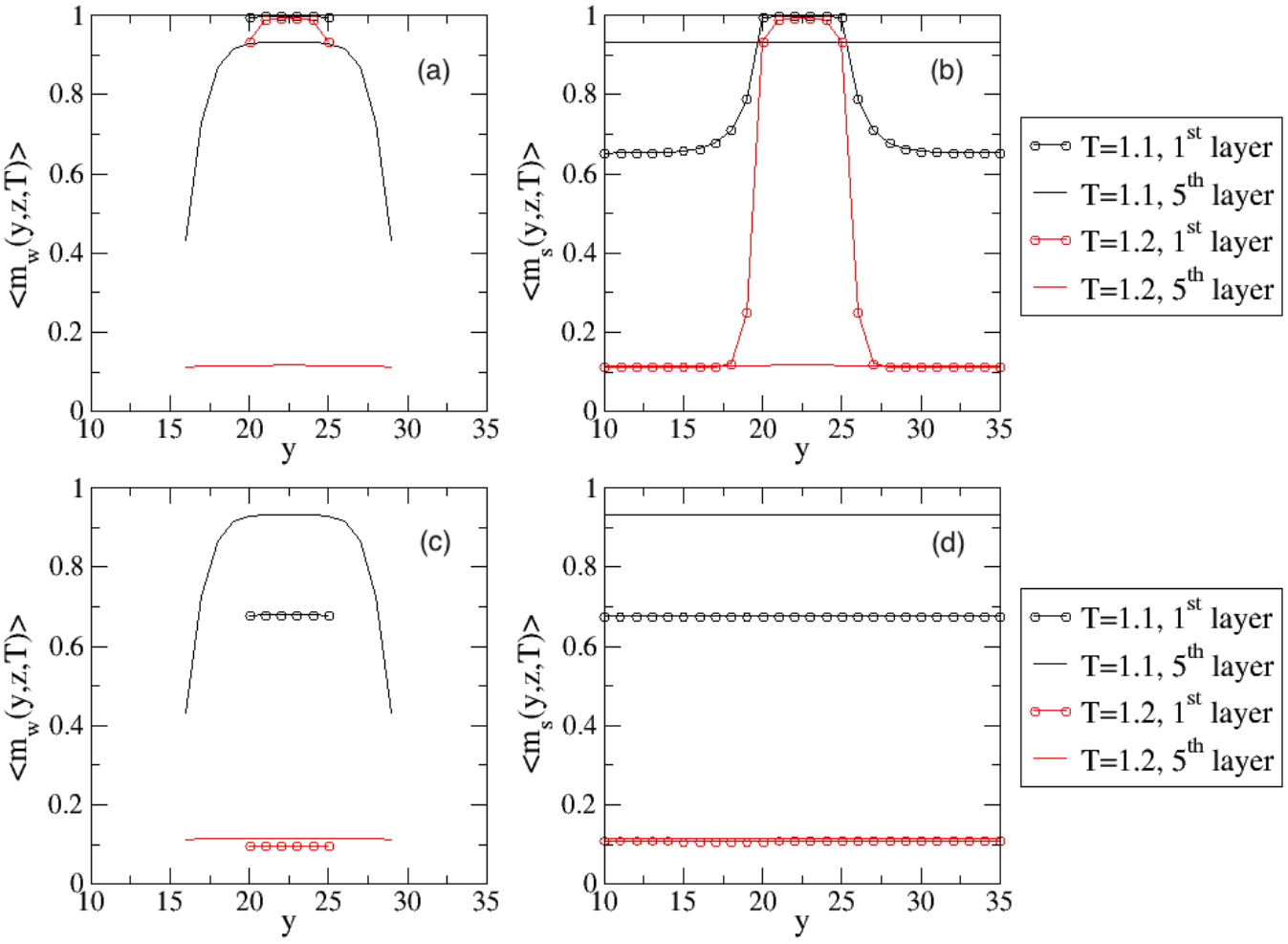

Figure 4.39: Panels (a) and (b) show the average line magnetizations of wedge-block systems with $v = 0$, whereas panels (c) and (d) show the average line magnetizations of systems with $v = 80$. Panels (a) and (c) show the average line magnetizations of the first and the fifth layer from the bottom of the wedge lattice, whereas panels (b) and (d) show the average line magnetizations of the first and the fifth later from the top of the lower block lattice. Other system parameters are $q = 9$, $\kappa_f = 9$, $A = 6$, $L = W = 40$, $h = H = 20$, $t_{relax} = 20000$, $t_{run} = 25000$. Averages are obtained from 16 independent runs.

The Line Magnetization Correlation Function

To study the local magnetic fluctuation of the wedge-block systems, we focus on $q = 9$ Potts systems with different wedge sizes: $A = 1$ and $A = 6$. By looking at the line magnetization correlation function of these systems with $\kappa_f = 9$ and $v = 80$, we can see how the size of the contacting area influences the local magnetic behavior of the surfaces.

Fig.4.40 shows the line magnetization correlation function data for the $\kappa_f = 1$ systems. Comparing the $k_BT\chi$ (20,1,1.1) in Fig.4.40(a) and the $k_BT\chi$ (22,1,1.1) in Fig.4.40(c), we find that the line magnetization correlation function value of the wedge tip is much larger when the tip size is small. To study the line magnetization correlation function values of the sites on the contacting surface, we look at Fig.4.40(b)(d) for detailed information. In Fig.4.40(b), where there is only one column/line of sites of the wedge sliding on the lower block, the line magnetization correlation function values of the sites on the contacting layer of the block show homogeneous distribution. However, in Fig.4.40(d), we find the line magnetization correlation function values $k_BT\chi$ (20,1,1.1), $k_BT\chi$ (21,1,1.1), $k_BT\chi$ (22,1,1.1), $k_BT\chi$ (23,1,1.1), $k_BT\chi$ (24,1,1.1), $k_BT\chi$ (25,1,1.1) show a small but steady increase. Since the $k_BT\chi$ values are numerically calculated with a coordinate fixed on the wedge, the change of the value of the magnetization correlation function in v direction indicates a modification of magnetic fluctuations due to magnetic friction.

Fig.4.41 shows plots of line magnetization correlation function for the $\kappa_f = 9$ systems with $v = 80$. From the black curves with circles in both Fig.4.41(a) and Fig.4.41(c), we find the line magnetization correlation function values of the sites on the wedge tip now become the same, which are around 0.22. In addition, we find that at $T = 1.2$ the line magnetization correlation function values also become the same, which are around 0.03.

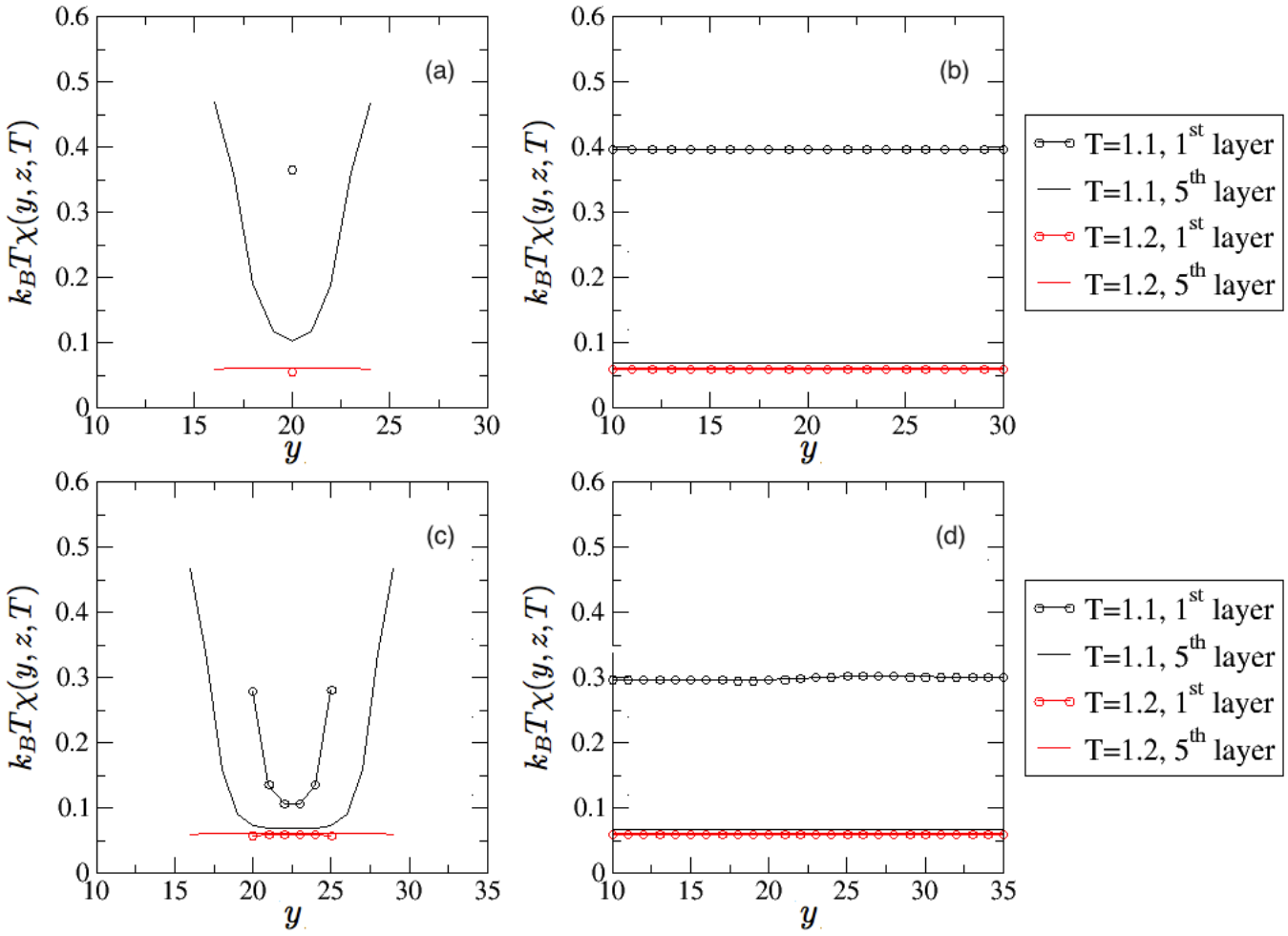

Figure 4.40: Panels (a) and (b) show the line magnetization correlation function data of wedge-block systems with $A = 1$, whereas panels (c) and (d) show the line magnetization correlation function data of the systems with $A = 6$. Panels (a) and (c) show the line magnetization correlation function data of the first and the fifth layer from the bottom of the wedge lattice, whereas panels (b) and (d) show the line magnetization correlation function data of the first and the fifth later from the top of the lower block lattice. Other system parameters include $q = 9$, $\kappa_f = 1$, $v = 80$, $L = W = 40$, $h = H = 20$, $t_{relax} = 20000$, $t_{run} = 25000$. Averages are made from 16 independent runs of Monte Carlo simulations.

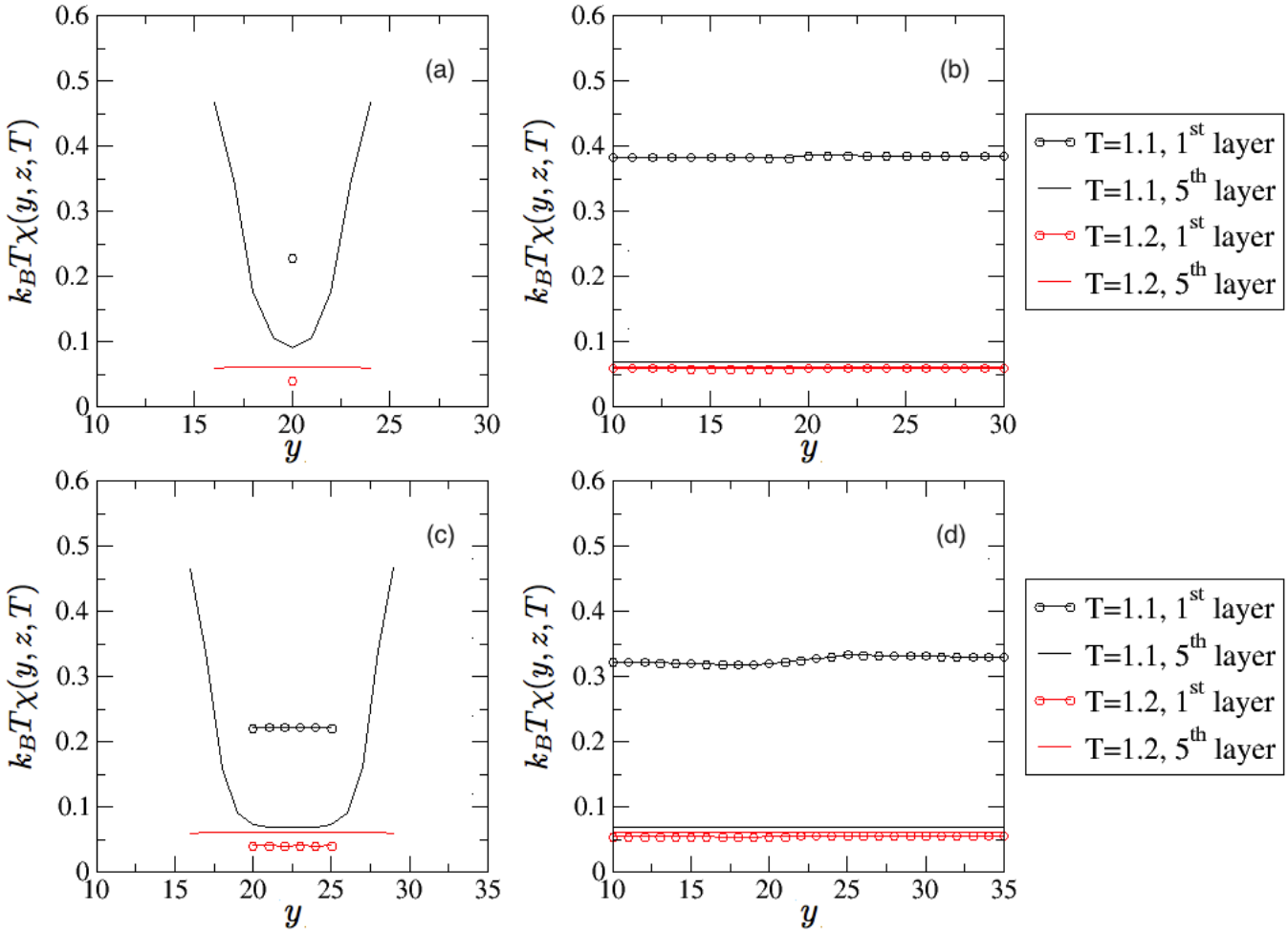

Figure 4.41: Panels (a) and (b) show the line magnetization correlation function data of wedge-block systems with $A = 1$, whereas panels (c) and (d) show the line magnetization correlation function data of the systems with $A = 6$. Panels (a) and (c) show the line magnetization correlation function data of the first and the fifth layer from the bottom of the wedge lattice, whereas panels (b) and (d) show the line magnetization correlation function data of the first and the fifth later from the top of the lower block lattice. Other system parameters include $q = 9$, $\kappa_f = 9$, $v = 80$, $L = W = 40$, $h = H = 20$, $t_{relax} = 20000$, $t_{run} = 25000$. Averages are made from 16 independent runs of Monte Carlo simulations.

Finally, we study the line magnetization correlation function of the sites on the contacting layer of the lower block. In Fig.4.41(b), where only one column (line) of sites of the wedge is sliding on the lower block, we observe a larger value of $k_BT\chi$ (20,1,1.1) compared to the value of $k_BT\chi$ (19,1,1.1), indicating that only one single column of contact of this $\kappa_f = 9$ and $v = 80$ system is enough to create an observable suppression of the fluctuation of the magnetization. This kind of suppression is made even more obvious in Fig.4.41(d), where the line magnetization correlation function value starts from 0.32 at $(y = 20, z = 1)$ and ends at 0.33 at $(y = 25, z = 1)$. This indicates that magnetic frictions with a larger contacting area (larger wedge size in the wedge-block system) can strengthen the suppression of the local magnetic fluctuations.

At temperature $T = 1.2$, all observed line magnetization correlation function values are small as the surfaces are fully disordered (see the red curves in Fig.4.40 and Fig.4.41).

4.4 Summary

In this chapter, the results of our research on magnetic friction are discussed. It is first shown that at the discontinuous bulk transition of a two-dimensional Potts lattice the surface transition is continuous and that the transition exponents actually depend on the total number of spin states of the Potts lattice. Secondly, the investigation of magnetic friction between three-dimensional Potts lattices is presented, where both full and partial surface contact are considered. In finite systems with periodic condition, we observed anisotropic surface magnetization when the interfacial coupling is strong. By varying the system size in the direction of movement, our simulation confirms that the anisotropic magnetization is a result of finite size effect. In the wedge systems with partial surface contact, we first discovered that the magnetic friction with large coupling constant on the contacting surfaces makes the finite size transition temperature of both surfaces similar

to each other. In addition, we found that strong interfacial couplings induce uniform magnetization on the wedge tip and suppresses locally the magnetic fluctuations on the lower contacting surface (in the locations where magnetic friction is taking place).

Chapter 5

Conclusions

In this dissertation, I introduced two models to study the non-equilibrium behavior of systems with energy input at interfaces or boundaries. The first model is a two-dimensional lattice gas system where energy is input into the system from the interface. The second model involves two three-dimensional Potts lattices moving against each other, along their contacting surfaces. Both models are studied through extensive Monte Carlo simulations and computational data analysis.

The simulation of the first model (two-dimensional lattice gas system) reveals novel non-equilibrium modulated steady states, as a result of the interplay of the spontaneous symmetry breaking in the cold sector and the convection cells formed along the interface. Through spectrum analysis, a finite-size phase diagram of the non-equilibrium states (the fully disordered state, the fully phase separated state, and the modulated state) as a function of system size and temperature (of the cold sector of the lattice) is numerically generated.

To study the second model, we first carefully investigated the surface behavior of the equilibrium two-dimensional Potts systems, where we found that the surface exponents

at the first-order bulk transition are dependent on the total number of states each site can take. We then studied Potts systems with different geometries, where magnetic friction happens in different manners. The first kind of system involves two identical Potts blocks/planes moving against each other, with full contact between the subsystems). The second kind involves one wedge-shaped lattice with its tip sliding on the surface of the lower block lattice with only partial contact between the sub-systems. For the first kind of geometry, we studied systems with different coupling strength κ_f, total number of states q, velocity of relative v movement, and system temperature T. We find that different degrees of anisotropy appear on the contacting surfaces. We also studied directional surface magnetizations for systems with different sizes, which leads to the conclusion that the observed anisotropy is due to finite size effects. For the second kind of geometry, we investigated systems with $q = 9$, varying κ_f, T and varying the tip size A of the wedge lattice. The first discovery from the Monte Carlo simulations is that magnetic friction with strong interfacial couplings ($\kappa_f = 9$) makes the finite size transition on both of the contacting surfaces very similar to each other. The second discovery is that the large κ_f causes uniform magnetization on the wedge tip. The third finding from the simulations indicates that magnetic friction effectively suppresses magnetic fluctuations on the surface of the lower block lattice.

Bibliography

[1] E. Ising, Contribution to the theory of ferromagnetism. *Z. Phys.* **31** 253 (1925).

[2] R. B. Potts, Some generalized order-disorder transformations. *Mathematical Proceedings of the Cambridge Philosophical Society* **01** 106 (1952).

[3] A. A. Markov, *Z. Theory of Algorithms.* Academy of Sciences of the USSR (1954).

[4] W. Feller, *An Introduction to Probability Theory and Its Applications.* Wiley, New York (1968).

[5] N.G. van Kampen, *Stochastic Processes in Physics and Chemistry.* North-Holland, Amsterdam (1981).

[6] M. Pleimling, *Class Notes of Non-equilibrium Statistical Physics.* Virginia Tech, Blacksburg (2011).

[7] L. Boltzmann, Einige allgemeine Sätze ber Wätrmegleichgewicht. Ŵiener Berichte **63** 679 (1871).

[8] J. W. Gibbs, *Elementary Principles in Statistical Mechanics.* Charles Scribner's Sons, New York (2011).

[9] J. McGreevy, *Class Notes of Thermodynamics and Statistical Mechanics.* University of California at San Diego (2012).

[10] K. Huang, *Statistical Physics.* CRC Press (2010).

[11] D. A. Lavis, G. M. Bell, *Statistical Mechanics of Lattice Systems: Closed Form and Exact Solutions.* Springer (1999).

[12] M. Henkel, M. Pleimling, R. Sanctuar, *Ageing and the Glass Transition.* Springer (2007).

[13] U. C. Täuber, *Critical Dynamics: A Field Theory Approach to Equilibrium and Non-Equilibrium Scaling Behavior.* Cambridge University Press (2014).

[14] D. P. Landau, K. Binder, *A Guide to Monte Carlo Simulations in Statistical Physics* Cambridge University Press, Cambridge (2000).

[15] D. Zubarev, V. G. Morozov, G. Röpke, Volume 2: Relaxation and hydrodynamic processes *Statistical Mechanics of Nonequilibrium Processes* Akademie Verlag, Germany (1996).

[16] H. Park and M. Pleimling, Surface criticality at a dynamic phase transition. *Phys. Rev. Lett.* **109** 175703 (2012).

[17] H. Park and M. Pleimling, Dynamic phase transition in the three-dimensional kinetic Ising model in an oscillating field. *Phys. Rev. E.* **87** 032145 (2013).

[18] G. L. Daquila, U. C. Täuber, Slow relaxation and aging kinetics for the driven lattice gas. *Phys. Rev. E.* **83** 051107 (2011).

[19] G. L. Daquila, U. C. Täuber, Nonequilibrium relaxation and critical aging for driven Ising lattice gases. *Phys. Rev. Lett.* **108** 110602 (2012).

[20] Y.-L. Chou and M. Pleimling, Parameter-free scaling relation for nonequilibrium growth processes. *Phys. Rev. E.* **79** 051605 (2009).

[21] Y.-L. Chou and M. Pleimling, Characterization of non-equilibrium growth through global two-time quantities. *J. Stat. Mech.* P08007 (2010).

[22] W. Janke, Monte Carlo simulations in statistical physics – from basic principles to advanced applications. *Order, Disorder and Criticality.* **3** 93 (2013).

[23] N. Metropolis, A. W. Rosenbluth, M. N. Rosenbluth, A. H. Teller, and E. Teller, Equation of state calculations by fast computing machines. *J. Chem. Phys.* **21**, 1087 (1953).

[24] R. J. Glauber, *Lectures in Theoretical Physics.* ed. W. E. Brittin and L. G. Dunham, New York (1959).

[25] K. Kawasaki, Diffusion constants near the critical point for time-dependent Ising models. I *Phys. Rev.* **145**, 224 (1966).

[26] K. Binder, *The Monte Carlo Method in Condensed Matter Physics.* Springer, New York (1995).

[27] M. Pleimling, B. Schmittmann, and R. K. P. Zia, Convection cells induced by spontaneous symmetry breaking. *EPL* **89**, 50001 (2010).

[28] L. Li, M. Pleimling, Formation of nonequilibrium modulated phases under local energy input. *EPL* **98**, 30004 (2012).

[29] H. Dosch, *Critical Phenomena at Surfaces and Interfaces.* Springer, New York (1992).

[30] M. Pleimling, Critical phenomena at perfect and non-perfect surfaces. *J. Phys. A: Math. Gen.* **37**, R79 (2004).

[31] K. Binder and D. P. Landau, Crossover scaling and critical behavior at the "Surface-Bulk" multicritical point. *Phys. Rev. Lett.* **52**, 318 (1984).

[32] R. Lipowsky, Critical surface phenomena at first-order bulk transitions. *Phys. Rev. Lett.* **49**, 1575 (1982).

[33] L. Li, M. Pleimling, Surface critical exponents at a discontinuous bulk transition. *Phys. Rev. B* **99**, 214426 (2013).

[34] R. Lipowsky, Surface induced disordering at first-order bulk transitions. *Z. Phys. B* **51**, 165 (1983).

[35] R. Lipowsky and W. Speth, Semi-infinite systems with first order bulk transitions. *Phys. Rev. B* **28**, 3983 (1983).

[36] F. Iglói and E. Carlon, Boundary and bulk phase transitions in the two-dimensional Q-state Potts model (Q>4). *Phys. Rev. B* **59**, 3783 (1999).

[37] D. Kadau, A. Hucht, and D. E. Wolf, Magnetic friction in Ising spin systems. *Phys. Rev. Lett.* **101**, 137205 (2008).

[38] A. Hucht, Nonequilibrium phase transition in an exactly solvable driven Ising model with friction. *Phys. Rev. E* **80**, 061138 (2009).

[39] M. P. Magiera, S. Angst, A. Hucht, and D. E. Wolf, Magnetic friction: from Stokes to Coulomb behavior. *Phys. Rev. B* **84**, 212301 (2011).

[40] F. Iglói, M. Pleimling, and L. Turban, Nonequilibrium phase transition in a driven Potts model with friction. *Phys. Rev. E* **83**, 041110 (2011).

[41] L. Li and M. Pleimling, in preparation.

[42] M. Pleimling and W. Selke, Critical phenomena at perfect and non-perfect surfaces. *Eur. Phys. J. B* **1** 385-391 (1998).

[43] A. Pelissetto and E. Vicari, Critical phenomena and renormalization-group theory. *Physics Reports* **368** 549-727 (2002).

[44] A. M. Ferrenberg and D. P. Landau, Critical behavior of the three-dimensional Ising model: A high-resolution Monte Carlo study. *Phys. Rev. B* **44**, 5081(1991).

[45] H. J. Herrmann, Monte Carlo simulation of the three-dimensional Potts model. *Z. Physik* **35** 171-175 (1979).

[46] F. Y. Wu, The Potts model. *Reviews of Modern Physics* **54** 235-268 (1982).